STRUCTURE AND CARRIER TRANSPORT IN AMORPHOUS SEMICONDUCTORS

A dissertation presented to

the faculty of

the College of Arts and Sciences of Ohio University

In partial fulfillment

of the requirements for the degree

Doctor of Philosophy

Tesfaye A. Abtew

June 2007

This dissertation entitled

STRUCTURE AND CARRIER TRANSPORT IN AMORPHOUS SEMICONDUCTORS

by

TESFAYE A. ABTEW

has been approved for

the Department of Physics and Astronomy

and the College of Arts and Sciences of Ohio University by

David A. Drabold

Distinguished Professor of Physics

Benjamin M. Ogles

Dean, College of Arts and Sciences

Abtew, Tesfaye, Ph.D., June 2007, Physics and Astronomy

STRUCTURE AND CARRIER TRANSPORT IN AMORPHOUS SEMICONDUCTORS

(144 pp.)

Director of Dissertation: David A. Drabold

First-principles methods are used to study the network dynamics of hydrogenated amorphous silicon, including the motion of hydrogen. In addition to studies of atomic dynamics in the electronic ground state, a simple procedure is adopted to track the H dynamics n light-excited states. Consistent with recent experiments and computer simulations, formation of dihydride structures are observed for dynamics in the light-excited states, and explicit examples of pathways to these states are presented. My results appear to be consistent with aspects of the Staebler-Wronski effect, such as the light-induced creation of well-separated dangling bonds.

The network topology and defects in the amorphous $Si_{1-x}Ge_x$:H alloys have been analyzed. Structural changes, particularly an increase in the number of defects and strained bond angles, have been found as the Ge content increases from x=0.1 to 0.5. The electronic density of states exhibits a decreasing band gap and additional midgap and band-tail defect states as the Ge concentration increases. The network structures, which are responsible for midgap and band-tail states, are presented. The band tails show an exponential “Urbach” behavior. The mobility gap as a function of Ge concentration is also estimated.

Simulation of dynamics of localized states in a presence of thermal disorder is studied by integrating the time dependent Kohn-Sham equation and density functional

Hamiltonian. A rapid diffusion of the localized state to the extended state in a very short time step is observed. This diffusion is explained to be due to quantum mechanical mixing when another states gets close in energy to the state that is being tracked.

Finally, a study of transport in amorphous semiconductors is presented. Kubo-Greenwood formula is used for computing the DC conductivity of elemental and hydrogenated amorphous silicon for different temperatures. The results from this method are in good agreement with the experiment. The effect of doping on the DC conductivity is also presented. As the E_f level gets close to either the conduction edge or valence edge the DC conductivity increases. Once E_f exceeds the “mobility edge” there exist a weak temperature dependence on the DC conductivity.

Approved: _____

David A. Drabold

Distinguished Professor of Physics

To my wife Tsige(Marr), daughter Venezia(Veni) and our families

Figure 0.1: My family

Acknowledgments

There is no word to express the joy and satisfaction of reaching to a goal one had anticipated. I am extremely happy and joyful to be able to reach and attain my goal of getting a PhD in Physics. However, no success is possible without the tremendous support, encouragement and continuous presence of number of people in my study as well as a blessing from GOD. My gratitude to all of you is beyond words can explain.

It is not only in shaping my academic career, but also your encouragement and constant support was priceless and it won't suffice to say thank you, nevertheless I will say THANK YOU to you, my advisor and mentor, Professor David Drabold. I was (and am) lucky to have you as my advisor. You have been an advisor to talk about physics, a friend to talk about any issues and a big brother to help and talk about family problems.

I would like to thank the department of physics and astronomy at Ohio University USA and department of physics at Addis Ababa University Ethiopia for giving me the opportunity to pursue my study and all the support. My thanks extend to the NSF and ARO for financial support. Special thanks to Ennice Sweigart, Kyle Mckenzie who were very helpful and Don Roth who tirelessly answered all my questions regarding computer problems and even share a donut. I would like to thank Prof. D. Ingram, Prof. H. Castillo, Prof. D. Tees, and Prof. L. Chen for serving in my defense committee.

I am grateful to have best friends, Dr. Abay Gadissa and his wife Mihiret Yohannes, Masiresha Arimide and his wife Abaynesh Legesse, Fekade Mekonnen and his wife Hana, Solomon Fekade and his wife Tigist, Dr. Fesseha Kassahun and Dr. Bantikassegn Workalemahu for support, encouragement and friendship. My gratitude extends to my friend and colleague F. Inam, to the many discussions we had about physics, religion, politics, and others. I would like to thank all the group members of Prof. Drabold for collaboration and wonderful discussions and special thanks are for former members Dr. D. Tafen, Dr. R. Atta-fynn, and Dr. P. Biswas.

Finally, my wife Tsige Legesse (Marr) and my daughter Venezia Tesfaye (Veni), you are the *light* and *strength* of my life. Thank you for supporting and enduring with me all these years. I LOVE YOU. To all of our extended families thank you for your love, support and prayers.

Table of Contents

List of Tables

List of Figures

Chapter 1

Introduction

One of the big issues that the world that we are living in faces is the energy problem. There is a vast demand for energy and a need for alternative energy sources. Among the alternatives to fossil fuels is to use solar energy and energy sources like wind and hydrogen energy. These energy sources not only provide energy; they are also environment friendly and clean with no repercussion to the planet we live on. One of the materials which has been used for the last decades in making solar cells is hydrogenated amorphous silicon (a-Si:H). The possibility of making a uniform monolithic thin film and cheap processing cost make a-Si:H a valuable candidate for applications. However, there is a drawback associated with extended exposure of solar cells made of a-Si:H to light: the process of light-induced degradation, the Staebler-Wronski Effect (SWE) first observed in 1977 [1]. There are several theoretical models and explanations proposed for the light induced degradation of a-Si:H. However a complete understanding of this problem is still unavailable.

In the last decades, extensive work in experiment and modeling has been conducted to get the microscopic origin of SWE. Diffusion and concentration of hydrogen, and presence of defects and impurities in the network have been considered to play a key role in SWE [2]. Light-induced structural changes are complex, and information about the changes is provided by an array of experiments [2, 3, 4]. Some

of the experimental features associated with SWE are the change in the conductivity with defect creation (carrier trap formation), light induced hydrogen diffusion [5, 6], preferential formation of a structure with proton distance of 2.3 Å in device grade material and a shorter distance in low quality material [7]. Further, it was shown that metastable dangling bonds (DB) were separated by at least 10 Å, studies of defect creation and annealing kinetics in a-Si/Ge:H suggest that there is not a large population of mobile H leading to recapture events of H onto DBs as part of the photo-degradation process [8].

This work has been strongly motivated by a nuclear magnetic resonance measurement for light soaked material made of a-Si:H and observed an enhanced population of proton proton distance of 2.3±0.2 Å unseen in the original material. The SWE effect is not limited to the a-Si:H materials. It has been reported that hydrogenated silicon germanium alloys (a-SiGe:H) which also show the light induced degradation [9].

A basic goal in this dissertation is to understand the light-induced degradation and to probe different structures to obtain explanation that can be related to the NMR and other experimental observations.

The other aspect of hydrogenated amorphous silicon that is investigated in this work is carrier transport. This is primarily because of the importance of a-Si:H as an electronic material. In the last decades researchers have been studying and developing different methods and models to understand the role of defects and disorder in

the electronic structure and electronic transport of amorphous and crystalline solids [10]. However, many fundamental questions, especially on transport and optical properties, are still not fully understood qualitatively or quantitatively. The carrier transport is strongly influenced by disorder, defects (such as non-fourfold atoms) which introduce localized states in the optical gap and these states are strongly affected by phonons [11]. Hopping and electron diffusion occur as phonons derive nearby states into resonance [12, 13]. Studying the dynamics of electrons is key in the understanding of the nature of transport in disorder materials. In this dissertation, the dynamics of localized states in the presence of thermal disorder are investigated by integrating the time dependent Kohn-Sham equation. The study of transport in amorphous materials is also presented. Kubo-Greenwood formula is used to compute the DC conductivity of amorphous semiconductors.

1.1 Models

Since a small set of structural models of a-Si and a-Si:H is employed in this work, in this section these models are summarized for reference throughout the rest of the dissertation. The first step in performing a predictive simulation is to have a physically plausible model, which represents the topology of the network to yield an accurate description for the static (minimum energy conformation) properties and dynamics of the atoms. In this work defect free 64 and 216 atom a-Si models are used as a starting configuration for generating hydrogenated a-Si models shown in

Fig. 1.1. These starting models were generated by Barkema and Mousseau [14] using an improved version of the Wooten, Winer, and Weaire (WWW) algorithm [15]. New

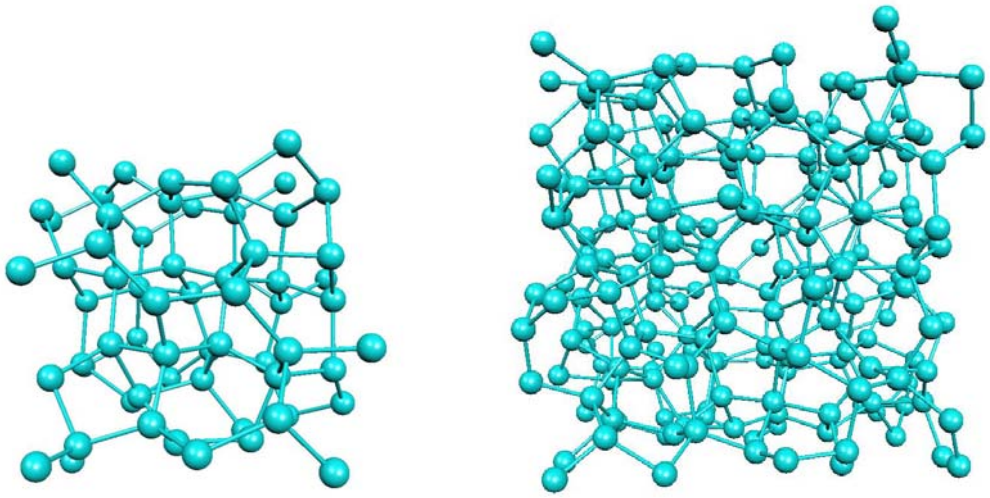

(a) (b)

Figure 1.1: The two structural models of amorphous silicon (a) a 64 atom a-Si model and (b) a 216 atom a-Si model. Periodic boundary conditions are used in all calculations in this dissertation.

supercell models have been developed from these initial models among which are: 70 atom a-Si:H models $aSi_{62}H_8$ [$aSi_{62}H_8$(a), $aSi_{62}H_8$(b), and $aSi_{62}H_8$(c)], a 72 atom a-Si:H model ($aSi_{61}H_{11}$), a 71 atom a-Si:H model ($aSi_{61}H_{10}$). A defect-free 64 atom a-Si model Fig. 1.1(a) is used as a starting configuration for generating these models. For $aSi_{62}H_8$(a), the working supercell is obtained by removing two Si atoms. The dangling bonds are terminated by adding 8 H atoms to create defect-free (that is, gap state free) structures with SiH_2 structural unit present in the network. This yields a 70 atom a-Si:H $aSi_{62}H_8$(a). The SiH_2 conformations obtained in the $aSi_{62}H_8$(a) and $aSi_{61}H_{11}$ are shown in Fig. 1.2(a) and Fig. 1.2(b).

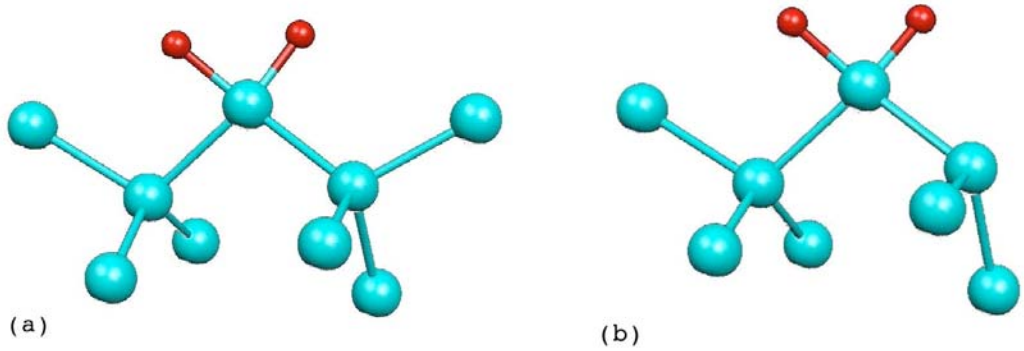

Figure 1.2: (a) SiH_2 conformation in $aSi_{62}H_8$ and (b) SiH_2 conformation in $aSi_{61}H_{11}$ with a dangling bond [16].

Other structural units which has two (Si-H) structural models (each with 3 different configurations) are generated as shown in Fig. 1.3. The first one is a model that contains an (H-Si-Si-H) structure which is referred as $aSi_{62}H_8$(b), where the two Si atoms are bonded to each other as shown in Fig. 1.3 (a) and the other one is a model that contains an (H-Si Si-H) structure which is referred as $aSi_{62}H_8$(c) where the two Si atoms are not bonded but are next nearest neighbors ($\sim$ 4.0 Å) as shown in Fig. 1.3 (b).

Model $aSi_{61}H_{11}$ is obtained in the same way except that one more Si atom is removed to form a 72 atom a-Si:H cell (61 Si atoms and 11 H atoms), which includes one dangling bond [17]. This supercell surgery is repeated at other sites to generate an ensemble of models to obtain some insight into the bonding statistics of SiH_2 conformations in the solid state. $aSi_{61}H_{10}$ is generated in the same way as $aSi_{61}H_{11}$ except this time there are two dangling bonds and no SiH_2 structure (61 Si atoms and 10 H atoms).

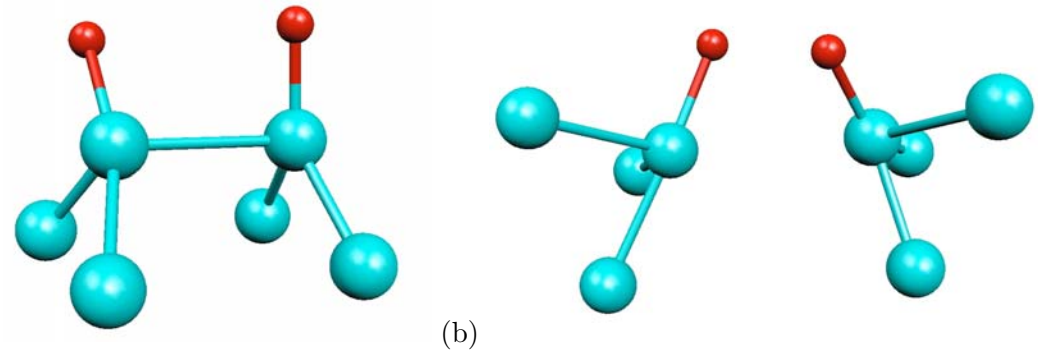

(a) (b)

Figure 1.3: The two structural units of hydrogenated amorphous silicon with 2(Si-H) structure (a) with the two Si atoms bonded: $aSi_{62}H_8$(b), and (b) with the two Si atoms as next nearest neighbors : $aSi_{62}H_8$(c).

In addition to the aforementioned models other models are used in this work including a 138 atom cell (18 of the atoms are H) a-Si:H model [18] ($aSi_{120}H_{18}$), a 223 atom a-Si:H model ($aSi_{214}H_9$; 214 Si and 9 H atoms) and a 223 atom a-$Si_{1-x}Ge_x$:H model. For $aSi_{214}H_9$, by starting from from a 216 atom a-Si model with two dangling bonds, two silicon atoms are removed which resulted in the formation of additional vacancies. All of the vacancies except one are then terminated by placing a H atom at about 1.5 Å from the corresponding Si atom. Finally these newly generated structures are well relaxed using conjugate gradient optimization technique and SIESTA (discussed in the next section). While such surgical procedures are clearly unphysical, it is worth pointing out that the resulting proton NMR second moments of the clusters created are similar to the broad component of the line shape observed in experiments [19]. The starting configuration for a-$Si_{1-x}Ge_x$:H model is a well relaxed $aSi_{214}H_9$ model, then some of the Si atoms are substituted by germanium according to the required concentration and relax the newly constructed configuration.

In Fig. 1.4, Fig. 1.5, and Fig. 1.6, the structure of these models are illustrated by computing the partial pair correlation of the initial models as well as the hydrogenated amorphous silicon models which are generated. In all cases the Si-Si partial correlation shows a first peak of 2.36 Å and a second peak of 3.79 Å. After the hydrogenation there is a very small shift on the first and second peaks where the first peak is about 2.38 Å and the second peak is about 3.88 Å.

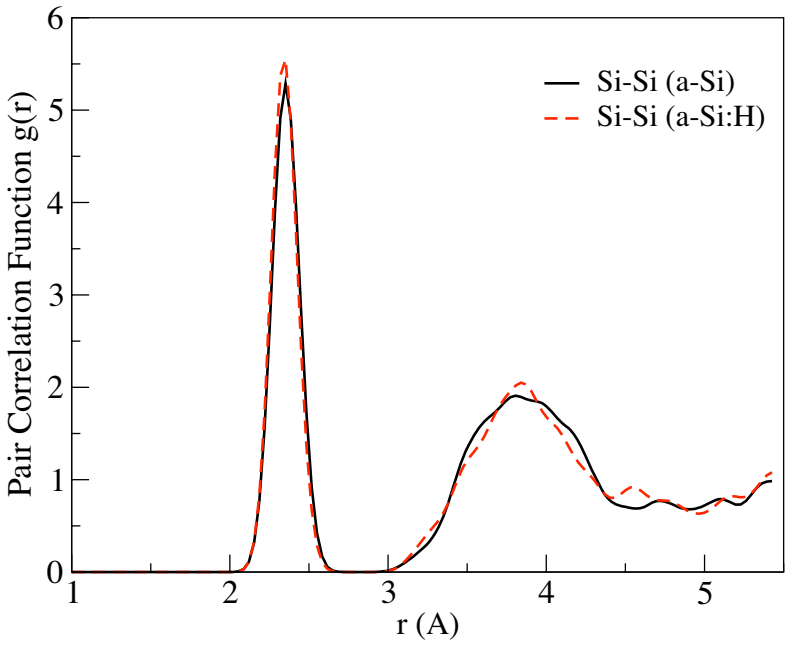

Figure 1.4: Partial pair correlation for Si-Si for aSi_{64} and for $aSi_{61}H_{10}$ models.

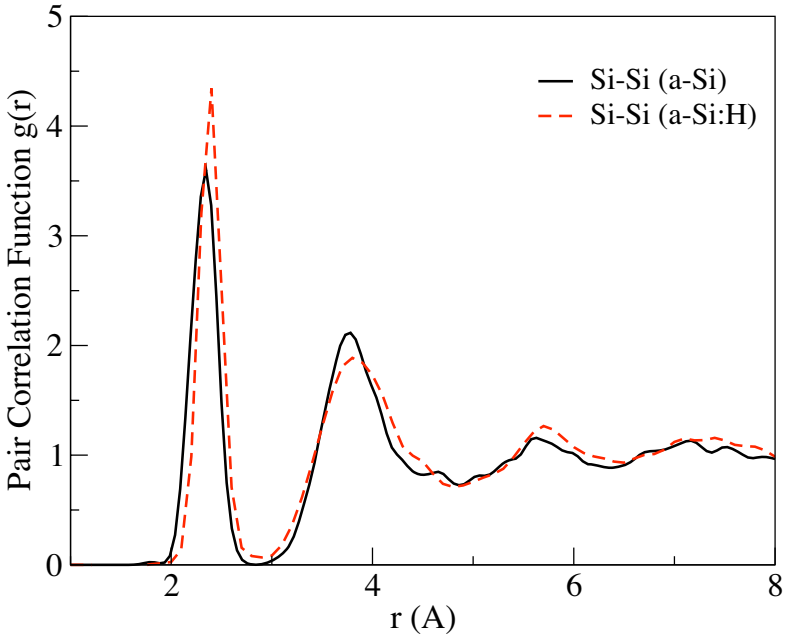

Figure 1.5: Partial pair correlation for Si-Si for aSi_{216} model and for $aSi_{214}H_9$ model.

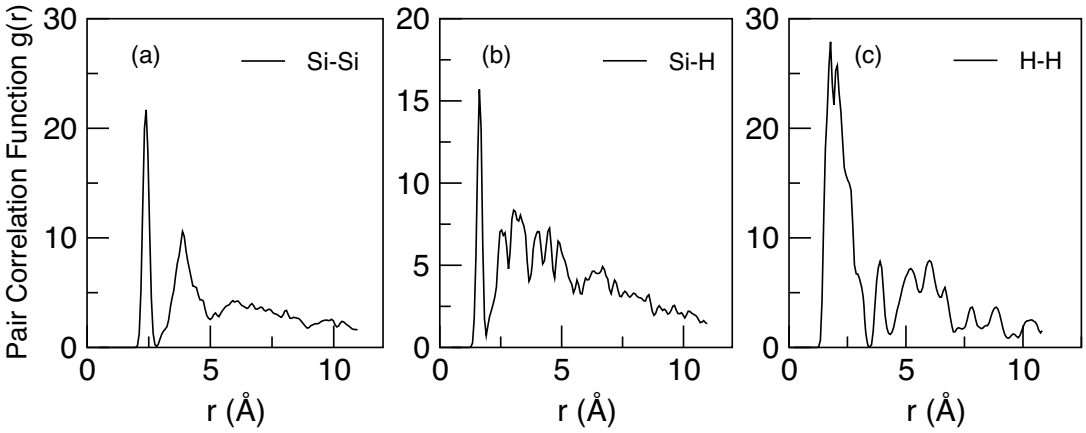

Figure 1.6: Partial pair correlation function for (a) Si-Si, (b) Si-H, and (c) H-H for the $aSi_{120}H_{18}$ model.

1.2 SIESTA

In this work the *ab initio* code SIESTA[1] which uses the localized orbitals is used. This code offers both flexibility and high accuracy, attributes required for studies of disorder phases of matter. Here a terse description of the method and the parameters and approximation used is presented. Detailed description of these methods are well presented in Ref. [20].

SIESTA [21] uses the standard Kohn-Sham self-consistent density functional method in the local density (LDA-LSD) or generalized gradient (GGA) approximations [22, 23, 24] with different parametrization options for the exchange correlation function. In this work, parametrization of Perdew and Zunger (PZ) [25] in the LDA and of Perdew, Burke and Ernzerhof (PBE) [26] in the GGA are used. Norm conserving Troullier-Martins [27] pseudopotentials factorized in the Kleinman-Bylander [28] form were used. For LDA both double ζ polarized basis sets (DZP), where two s and three p orbitals for the H valence electron and two s, six p and five d orbitals for Si valence electrons were used, and for comparison a cruder single ζ basis set (SZ), where one s orbital for the H valence electron and one s and three p orbitals for Si valence electrons were used. Only DZP basis sets is used for GGA calculations. For details on generation of the basis orbitals see reference [29] and references therein.

[1] SIESTA (Spanish Initiative for Electronic Simulations with Thousands of Atoms) is both a method and a computer program implementation, to perform electronic structure calculations and ab initio molecular dynamics simulations of molecules and solids. Comprehensive reviews are available in Ref [20].

1.3 Outline

The dissertation is organized as follows. Introduction, different models and the density functional code that are used in this work are discussed in Chapter 1. In Chapter 2, investigation of different dihydride structures and the comparison of the results from this work and the NMR experiment is presented. Then a ground state and simulated light excited state simulation which suggests the formation of dihydride structure is presented. Finally the consequence of hydrogen diffusion to the electronic and vibrational properties is discussed. In Chapter 3 a thorough investigation of hydrogen diffusion and its mechanisms and a key short time mechanism for the hydrogen diffusion are presented. The structural, dynamical, and electronic properties of amorphous $Si_{1-x}Ge_x$:H alloys, and the effect of germanium concentration on the electronic properties are presented in Chapter 4. In Chapter 5, time dependent Kohn-Sham equations is presented. The general method for estimating the DC conductivity using the Kubo-Greenwood formula and its application, the effect of doping and the Meyer Neldel rule are also presented in Chapter 5. Finally concluding remarks are presented in Chapter 6 which is followed by Appendix A.

In this dissertation, I report my research on several topics, most of which was published only with my advisor and in one case with a fellow graduate student F. Inam (chapter 3). Inam's role in that chapter was to assist in computing statistics of bond breaking which is minor in the whole chapter. The dissertation consist of several chapters, most of which have been published in closely related forms in journals. My

contributions in this dissertation and in the published and submitted articles are: all of the simulation work, all of the writing (with many editing and corrections from my advisor D. A. Drabold) and all of the calculations except one Ref. [H] where Inam contributed few results. All of my results are under a constant guidance from my advisor D. A. Drabold. Our list of publications follows:

I. **T A Abtew** and D A Drabold, *"Thermally driven hopping and electron transport in amorphous materials from density functional calculations"*, **J. Phys. Cond. Matt. (16)** S5289-S5296 (2004).

II. **T A Abtew**, D A Drabold and P C Taylor, *"Studies of silicon dihydride and its potential role in light-induced metastability in hydrogenated amorphous silicon"*, **Appl. Phys. Lett. (86)** 241916 (2005).

III. **T A Abtew** and D A Drabold, *"Simulation of light-induced changes in hydrogenated amorphous silicon"*, **J. Phys. Cond. Matt. (18)** L1 (2006).

IV. **T A Abtew** and D A Drabold, *"Hydrogen dynamics and light-induced structural changes in hydrogenated amorphous silicon"*, **Phys. Rev. B (74)** 085201 (2006).

V. D A Drabold and **T A Abtew**, *"Defects in Amorphous semiconductors: amorphous silicon, in Theory of Defects in Semiconductors"*, Edited by D. A. Drabold and S. K. Estreicher, Springer-Verlag (2006)."

VI. **T A Abtew** and D A Drabold, *"First principles molecular dynamics study of amorphous $Si_{1-x}Ge_x$:H alloys"*, **Phys. Rev. B (75)** 045201 (2007).

VII. **T A Abtew** and D A Drabold, *"Light induced structural changes in hydrogenated amorphous silicon"*, **J. of Optoelect. and Adv. Mater. (8)** 1979 (2006).

VIII. **T A Abtew**, F. Inam, and D A Drabold, Thermally stimulated H emission and diffusion in hydrogenated amorphous silicon, **submitted to PRL** (Nov. 2006).

Chapter 2

Light induced structural changes in hydrogenated amorphous silicon

The work presented in this chapter is published: T A Abtew, D A Drabold and P C Taylor, Appl. Phys. Lett. **(86)** *241916 (2005); T A Abtew and D A Drabold, J. Phys. Cond. Matt.* **(18)** *L1 (2006); T A Abtew and D A Drabold, J. of Optoelect. and Adv. Mater.* **(8)** *1979 (2006); T A Abtew and D A Drabold, Phys. Rev. B* **(74)** *085201 (2006).*

There have been various proposals for the microscopic origins of the Staebler-Wronski effect (SWE). One class of models involves breaking of "weak bonds" which were often unspecified [30]. Another class of models propose the creation of new defects as a result of movement of the original defect [31]. Zafar *et al.*[32] considered a metastability model based on transfer of H between clustered and isolated phases seen by NMR. Bonding in each of these phases was presumed to be monohydride. In their subsequent work Zafar *et al.*[33] showed that the 2-phase picture satisfactorily accounted for new experiments on the thermal changes in the spin-density and also the changes caused by evolving hydrogen. Nevertheless, this model was unable to account for light-induced effects.

Some current theories combine the electronic and hydrogen energy states and hydrogen diffusion as in the hydrogen collision model of Branz [5] and the hydrogen

flip model of Biswas *et al.* [34] . Kopidakis *et al.*[35] proposed that clustered-phase sites can bind either one or two hydrogen pairs (dihydride-bonding). In this line of argument, recently, Zhang *et al.*[36] proposed a model that m vacancies of m missing Si atoms, which are fully terminated with Si-H bonds to eliminate dangling bonds (DB) and strained Si-Si bonds, provide the H-pair reservoir and metastability sites in Si. There are also newer findings [37] that reveal a lack of spatial correlation between the defects and hydrogen, the realization that the effectiveness of light induced defects as recombination centers depends on the light exposure conditions, and the observation that it is not only defects which are produced by extended light exposure but also larger structural changes in the material involving the Si network.

An experimental clue of importance that has strongly motivated our work was recently reported by Su *et al.* [7], who performed nuclear magnetic resonance (NMR) experiments on protons in a-Si:H and found that the NMR spectrum of light-soaked a-Si:H films show the preferential creation of a H-H distance of 2.3 ± 0.2 Å. Remarkably, this experiment directly connects light soaking to creation of a specific new structure (or family of structures) in the amorphous matrix. Given the remarkably well-defined nature of the observed proton separation, it is natural to expect that the structure(s) causing the feature must be a well defined conformation. There are two possible interpretations of the results of Su *et al.* [7]. The simplest interpretation is that some metastable, paired-hydrogen site is formed after the exposure to light. A second interpretation, which can not be ruled out by the experiments to date, is that some

changes in the various NMR relaxation rates after exposure to light allow existing paired-hydrogen sites, such as SiH_2, to become observable in the NMR spectra. Of particular importance to the latter interpretation, Stutzmann *et al.* [30] have argued that the breaking of weak Si-Si bonds will also promote the diffusion of dangling bonds away from the original site. If the presence of such a dangling bond near a stable, paired-hydrogen site, for which the most logical candidate is SiH_2, allows this site to be seen in the H NMR, then the results of Su *et al.* are also logically explained. Although there are technical reasons why this explanation is not as probable as the formation of metastable, paired-hydrogen sites, it cannot be ruled out.

In this chapter we present a systematic study and analysis of light-induced effects in hydrogenated amorphous silicon. First we present a study on the feasibility of silicon dihydride structures for the observation of the NMR experiment of Su *et al.*. We then present a study of H atomic dynamics in the electronic ground states and light excited states. The diffusion mechanism of hydrogen and the resulting formation of new structure in the amorphous network is also discussed.

2.1 Silicon dihydride structures in a-Si:H

The experimental results of Su *et al.* [7] pose important questions. Is the observation of two protons separated by a distance of 2.3 Å feasible in terms of the energetics and structure of the amorphous network? And if feasible, what creates the

structure in the first place? In this section we answer the first question by investigating different structural units and compare them with experiment [16].

One of the possible candidates for the experimental observation of two protons separated by a 2.3 Å is a dihydride structure. This dihydride structure may be in the form of two H atoms connected to a single Si atom to form a H-Si-H structure where the Si atom is bonded with two additional Si atom and then four coordinated; or two nearby H atoms each connected to a Si atom as Si-H H-Si where each of the Si atoms are bonded with three more Si atoms.

In order to study these different structures, we have generated different models which include these structures embedded in the network. We used $aSi_{62}H_8$(a) and $aSi_{61}H_{11}$ discussed in Chapter 1 for studying the silicon dihydride structure of the form SiH_2. We have considered four configurations for each model in our calculation. Each configuration in the respective models was constructed by selecting different (typically tetrahedral) sites of the SiH_2 conformations in the cell. We performed our calculations of SiH_2 structure and dynamics on each of the four configurations of $aSi_{62}H_8$(a) and also on each of the four configurations of the $aSi_{61}H_{11}$ model.

For the first group of four configurations ($aSi_{62}H_8$(a)), our results are summarized in Table 2.1. In all these configurations, for different initial proton distances, we see a consistent approach to near the measured proton-proton separation of (2.3±0.2 Å) as the basis set improves from SZ to more complete DZP. Though the shift is smaller, there is also an improvement in agreement with the experiments in

going from LDA to GGA functionals. There is a strong message in these results that high-quality calculations are needed to properly describe the structure.

Table 2.1: The H-H distance before and after relaxation for $aSi_{62}H_8$(a) using LDA and GGA exchange correlation functional for four different configurations. The GGA (DZP) calculation is expected to be the most accurate [16].

Config-urations	H-H distance before relax-ation (Å)	H-H distance after relaxation (Å)		
		LDA (SZ)	LDA (DZP)	GGA (DZP)
1	1.58	2.51	2.40	2.38
2	2.27	2.38	2.36	2.35
3	3.02	2.69	2.46	2.42
4	3.30	2.59	2.47	2.42
Average		2.54	2.42	2.39

The same calculation has also been done for the $aSi_{61}H_{11}$, and, the results are given in Table 2.2. As before, a DZP basis set and GGA appears to be necessary. Consistent with the first configuration, $aSi_{61}H_{11}$ also gives proton separations well within the tolerance of the experiments of Su *et al.*. In these results we show that SiH_2 configurations in the solid state are consistent with the experimental observations. We also find that the details of basis set and density functional are important for accurately representing these structures.

Using accurate methods (a double-zeta polarized basis and a GGA) and supercells properly representing the disorder of a-Si:H, it has been shown that SiH_2 yields the proton-proton distance [16] inferred from the experimental work of Su *et*

Table 2.2: The H-H distance before and after relaxation for $aSi_{61}H_{11}$ using LDA and GGA exchange correlation functional for four different configurations. These models contain one dangling bond. The GGA (DZP) calculation is expected to be the most accurate [16].

Configurations	H-H distance before relaxation (Å)	H-H distance after relaxation (Å)		
		LDA (SZ)	LDA (DZP)	GGA (DZP)
1	1.61	2.39	2.35	2.34
2	2.20	2.59	2.51	2.46
3	2.35	2.34	2.33	2.32
4	3.29	2.56	2.47	2.44
Average		2.47	2.42	2.39

al. [7] Extending this to other silicon dihydride units is necessary for completeness and comparison to experiments [7] and other modeling [5].

We therefore generated two additional models, $aSi_{62}H_8$(b) and $aSi_{62}H_8$(c) , which contain the same number of atoms but different dihydride structural units as discussed in Chapter 1. Each configuration in the models is constructed by selecting different (tetrahedral) sites of the 2(Si-H) conformations in the cell. We then repeated this supercell surgery at other sites to generate an ensemble of models (3 configurations). Our objective here is to investigate whether these structures also exhibit a metastable structure with an H-H distance of 2.3 Å or not as we obtained for the SiH_2 structure that is discussed in the previous section.

To investigate the two silicon dihydride structural units, we relaxed $aSi_{62}H_8$(b) and $aSi_{62}H_8$(c) with pre-existing (H-Si-Si-H) and (H-Si Si-H) respectively. After relaxation we obtained an average H-H distance of 2.21 Å for paired hydrogen in

(H-Si-Si-H) units of the $aSi_{62}H_8$(b) model with a total energy of -6735.86 eV and 1.88 Å for paired hydrogen in (H-Si Si-H) units of the $aSi_{62}H_8$(c) model with a total energy of -6734.88 eV. This shows that the (H-Si-Si-H) structure has lower total energy by ∼980 meV as compared with the (H-Si Si-H) unit for these particular conformations. This number must be taken with a grain of salt since repeating the calculation at different sites would yield somewhat varied results. Nevertheless, in both cases the proton distance is somehow shorter than the 2.3 Å experimental result and with our previously reported theoretical result of 2.39 Å in SiH_2 structural unit. However, in the case of (H-Si-Si-H) with relatively larger initial H-H separation (∼ 3.0 Å), we have obtained larger final H-H distances (3.5 Å - 4.5 Å). The result for the calculation of the paired hydrogen distance in the three different configurations of $aSi_{62}H_8$(b) and $aSi_{62}H_8$(c) using both LDA and GGA are summarized in Table 2.3 and Table 2.4 respectively.

Table 2.3: H-H distance before and after relaxtion for "$aSi_{62}H_8$(b)" using LDA and GGA exchange correlation functional for three different configurations. The GGA (DZP) calculation is expected to be the most accurate.

	H-H distance		
Configurations	before relax (Å)	after relax (LDA) (Å)	after relax (GGA) (Å)
1	1.08	2.187	2.192
2	1.40	2.196	2.212
3	2.00	2.195	2.211
Average		2.193	2.205

Thus we conclude that the dihydride structure SiH_2, and H-Si-Si-H are the best candidates for the experimental measured proton-proton distance of 2.3±0.2 Å. In the case of SiH_2 we obtained a distance of 2.39 Å and in the case of H-Si-Si-H we obtained a distance of 2.21 Å. However, for H-Si-Si-H, we need to mention that there are cases where the proton-proton distance in the H-Si-Si-H becomes larger (3.5-4.5 Å) as compared with experiment.

Table 2.4: The H-H distance before and after relaxtion for "$aSi_{62}H_8$(c)" using LDA and GGA exchange correlation functional for three different configurations. The GGA (DZP) calculation is expected to be the most accurate.

	H-H distance		
Configurations	before relax (Å)	after relax (LDA) (Å)	after relax (GGA) (Å)
1	2.935	1.871	1.876
2	3.450	1.873	1.889
3	4.305	1.891	1.893
Average		1.878	1.886

Most of the aforementioned models of the SWE invoke paired-hydrogen sites. These models associate the SWE with the conversion of isolated H into paired-hydrogen sites, for which SiH_2 must be considered a prime candidate. The experiments of Su *et al.* [7] provide *direct* evidence that light soaking creates structures with a proton-proton separation of about 2.3 Å.

Given that the various models proposed [30, 31, 32, 33, 34, 35] all appear to be at least consistent with our calculations for SiH_2, the link between our calculations

and the NMR experiments is a very important step. On the other hand, what we have not done is provide any explanation of the light-induced formation of the SiH_2, which is certainly a key missing piece to the puzzle that we will address in the next section. This is not an easy process to simulate, since the (diffusive) time-scales for simulation are presumably vastly longer than what is directly accessible from our simulation.

Using accurate methods and supercells properly representing the disorder of a-Si:H, we determined dihydride structures that are credible candidates for the proton-proton distance inferred from the work of Su *et al.*. We have seen that accurate methods (including a double-zeta polarized basis and a GGA) are needed to properly describe the bonding in this system.

2.2 Hydrogen dynamics and its consequences to light exposed a-Si:H

In the previous section, the dihydride structural units are assumed to exist in the network *a priori*. In the next section we investigate if these dihydride structural units form upon light soaking starting from a network with no dihydride structure in the beginning of the simulation. We have performed extensive MD simulations of network dynamics of a-Si:H both in an electronic ground state ("light-off") and a simulated light-excited state ("light-on") using different models. We present a detailed calculation of hydrogen diffusion, its mechanisms and consequences on the

structural electronic and vibrational properties in both electronic ground state and light excited state [38, 39].

2.2.1 Hydrogen motion: Electronic ground state

To analyze the diffusion mechanism in the ground state we performed a MD simulation for five different temperatures, and tracked the trajectories and bonding information of all the H and Si atoms in the network. In all the cases, the MD simulations show diffusion of hydrogen in the cell and as a consequence, the network exhibits a complex bond-breaking and forming processes. The pattern of diffusion differs for individual H atoms depending upon the geometrical constraints around the diffusing H atom. A more detailed investigation of thermally stimulated hydrogen diffusion and its mechanisms will be given in detail in Chapter 3.

In order to illustrate the trajectories of H diffusion in the ground state, we have selected two diffusive H atoms, (H_{219} and H_{220}), and plotted their trajectories at T=300K in Fig. 2.1. The trajectories for both H_{219} and H_{220} atoms show diffusion in which the H atoms spend time being trapped in a small volume of the cell near a bond center which is followed by rapid emission to another trapping site. In order to examine how the bond rearrangement takes place in the network while the H atom is diffusing, we tracked each hydrogen atoms and computed its bonding statistics.

In Fig. 2.2 we show the Si-H bond length between one of the diffusing H atoms (namely H_{219}) and relevant Si atoms (Si_{90} and Si_{128}) with which it forms a

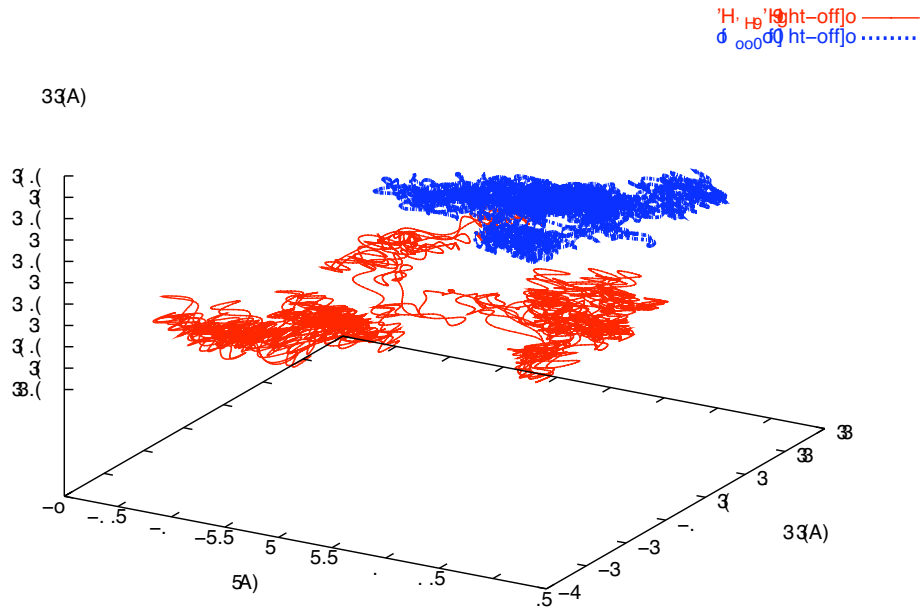

Figure 2.1: Trajectory for two different hydrogen atoms (H_{219} and H_{220}) in the ground state, which shows the diffusion and trapping of the atom for $aSi_{214}H_9$ model. The total time for the trajectory is 10ps [39].

bond while diffusing and Si_{208}. As we can see from Fig. 2.2, in the first 4ps H_{219} is bonded with Si_{90} with a bond length of 1.5 Å and trapped for a while until it breaks and hops to form another bond with Si_{128}. In the first ∼4 ps, the bond length between H_{219} and Si_{128} fluctuates between 3.8 Å and 2.5 Å. However, after ∼4 ps we observed a swift bond change in a very short period of time ∼0.1 ps when the H_{219} atom comes out of the trapping site and hops to form a bond with Si_{128} and becomes trapped there for ∼6 ps. This process of trapping and hopping appears to be typical for the highly diffusive H atoms.

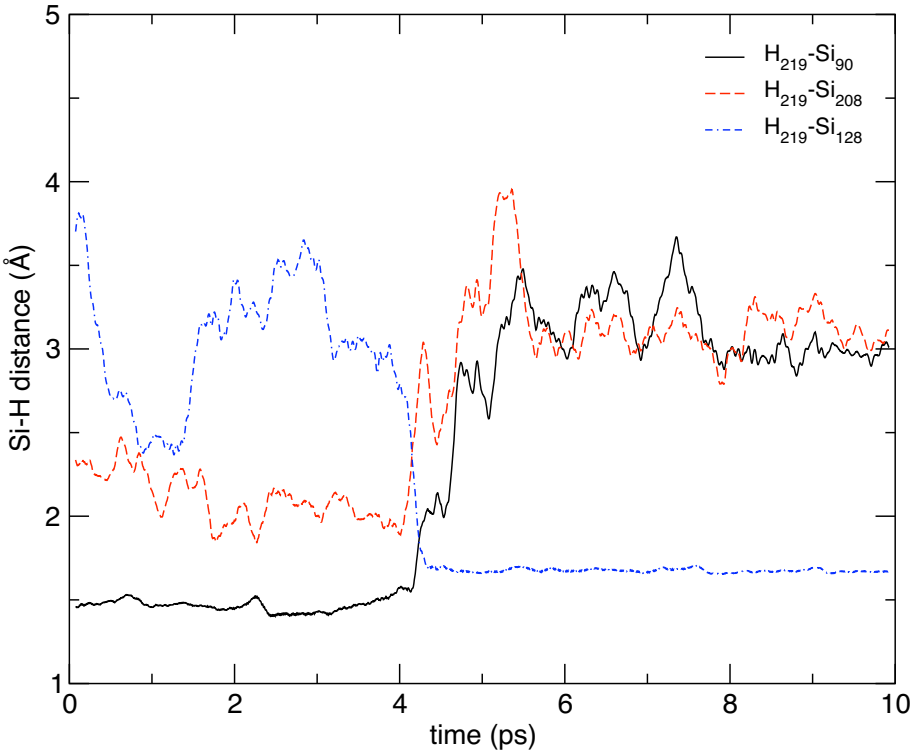

Figure 2.2: The Si-H bond length between the diffusing H (H_{219}) and three different Si atoms, (Si_{90}, Si_{208}, and Si_{128} as a function of time in the electronic ground state for $aSi_{214}H_9$. The total time for the trajectory is 10ps [39].

To study atomic diffusion we computed the time average mean squared displacement for both H and Si atoms for a given temperature using

$$\langle \sigma^2(\alpha, T) \rangle_{\text{time}} = \frac{1}{N_{MD}} \frac{1}{N_\alpha} \sum_{t=1}^{N_{MD}} \sum_{i=1}^{N_\alpha} |\vec{r}_i^{\,\alpha}(t) - \vec{r}_i^{\,\alpha}(0)|^2, \tag{2.1}$$

where the sum is over particular atomic species α (Si or H), N_α and $\vec{r}_i^{\,\alpha}(t)$ are total number and coordinates of the atomic species α at time t respectively, and N_{MD} is the total number of MD steps. The time average mean square displacement for $aSi_{61}H_{10}$ for five different temperatures was calculated using Eq. (2.1) for H atoms in the supercell in the electronic ground state ("light-off") and it is shown in Fig. 2.3.

We have observed a temperature dependence of H diffusion. This result will help us to compare the diffusion of H in the electronic ground state with the light excited state to be discussed in the next section.

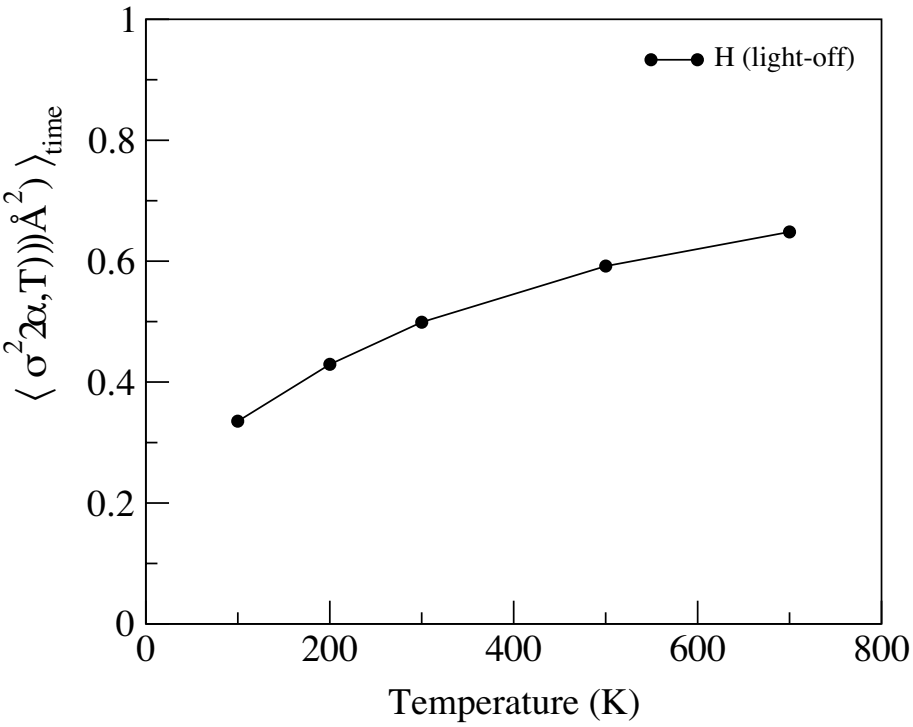

Figure 2.3: Time average mean square displacement for H as a function of temperature of MD simulation in electronic ground state for $aSi_{61}H_{10}$ [39].

2.2.2 Excited state dynamics and promotion of carriers

Defects in an amorphous network may lead to localized electron states in the optical gap or in the band tails. If such a system is exposed to band gap light, it becomes possible for the light to induce transitions from the occupied states to unoccupied states.

The stimulated light excited state ("light on") is achieved by starting from the well relaxed model, we add an electron to the system just above the Fermi level. The system is effectively in the excited state for ~ 400 fs until the electron recombines back to the top of the valence band. Since there is a strong electron-phonon coupling for a localized state, the additional electron causes local heating at a site where the state is localized. The local heating in turn introduces enhanced atomic diffusion in the vicinity of the localized site which eventually allow the atoms to diffuse out to the nearby sites.

2.2.3 Hydrogen motion: Light excited state

Similar to the case of electronic ground state, we analyzed the diffusion of H in the light excited state by performing a MD simulation. We tracked the trajectories and bonding statistics of Si and H atoms in the supercell. Our MD simulation in the light excited state show slightly enhanced hydrogen diffusion and consequently increased bond breaking and formation that leads to structural changes in the network.

For the purpose of analyzing the difference in the diffusion mechanism of H in the light excited state case as compared with the ground state, we performed similar calculations described in the previous sections for the light excited state case. To understand the trajectories of H in the light excited state, we have again selected two diffusive H atoms, (H_{219} and H_{220}) from the larger $aSi_{214}H_9$, and plotted their

trajectories in the light excited state in Fig. 2.4. The trajectories show the diffusion of H in the presence of different trapping centers, a region where the H atom spends more time before it hops and moves to another trapping site. However, in this case we observed enhanced diffusion and more trapping sites and hopping probably from local heating. These trapping and hopping processes continue until two hydrogens form a bond to a single Si atom to form a metastable SiH_2 conformation or until two hydrogens form a bond to (a) two different Si atoms which are bonded to each other, to form (H-Si-Si-H) structure or (b) two different Si atoms which are not bonded but close to each other to form (H-Si Si-H) structure. This is in agreement with a basic event of the H collision model [5] and other H-pairing models [35].

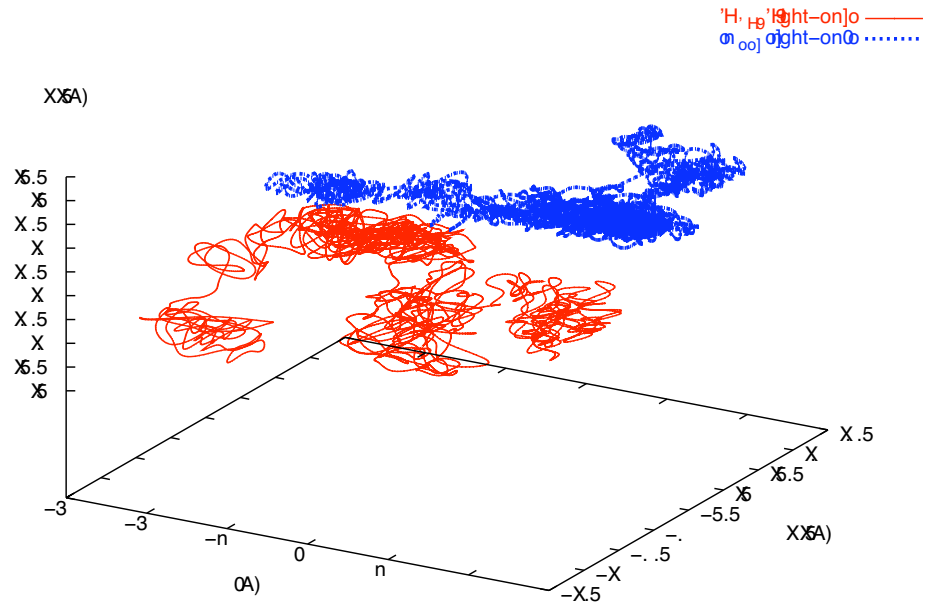

Figure 2.4: Trajectory for two different hydrogen atoms (H_{219} and H_{220}) which shows the diffusion and trapping of the atom for $aSi_{214}H_9$ in the light excited state. The total time for the trajectory is 10ps [39].

By tracking each H atom, we monitored its bonding and examine bond rearrangements. In Fig. 2.5 we show Si-H bond length as a function of time between one of the diffusing H atoms (H_{219}) and three other Si atoms (Si_{90}, Si_{128}, and Si_{208}) with which it forms a bond while diffusing in the network. As we can see from Fig. 2.5, the pattern of diffusion is quite different from the ground state: In the light excited state case we observed a) more number of trapping sites and less trapping time with frequent hopping, b) enhanced hydrogen diffusion, and c) increasing number of bond rearrangements and newly formed dihydride structural units. The atomic diffusion

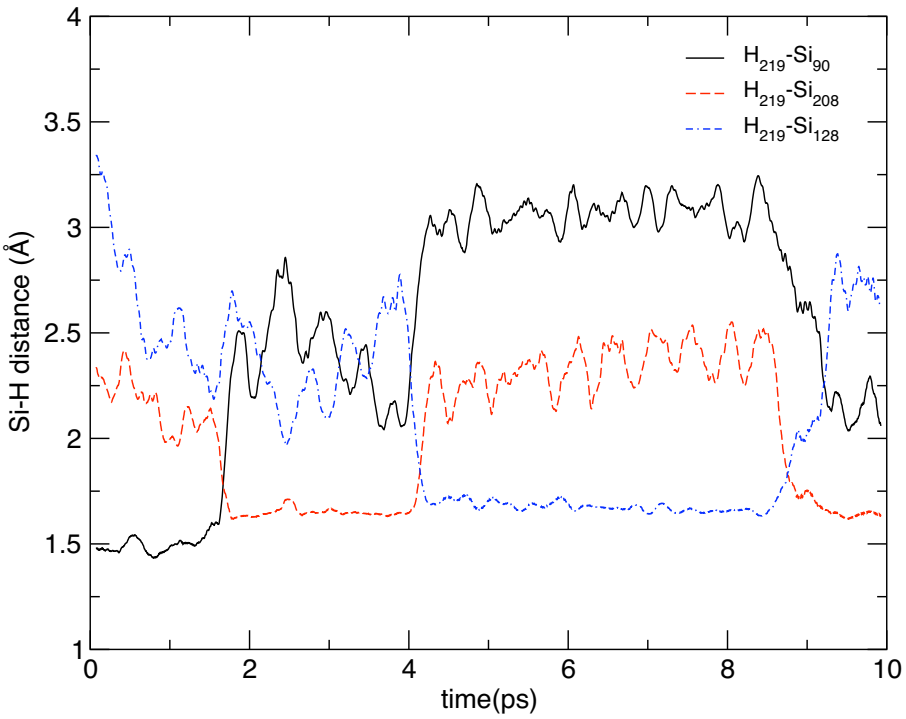

Figure 2.5: The Si-H bond length between the diffusing H (H_{219}) and three different Si atoms (Si_{90}, Si_{128}, and Si_{208}) with which H_{219} forms a bond (one at a time) while it is diffusing as a function of time for $aSi_{214}H_9$, in the light excited state. The total time for the trajectory is 10ps [39].

in the light excited state case has also been examined using the time average mean squared displacement for both H and Si atoms for different temperatures using Eq. 2.1 for both $aSi_{214}H_9$ and $aSi_{61}H_{10}$. The results from $aSi_{61}H_{10}$ are shown in Fig. 2.6.

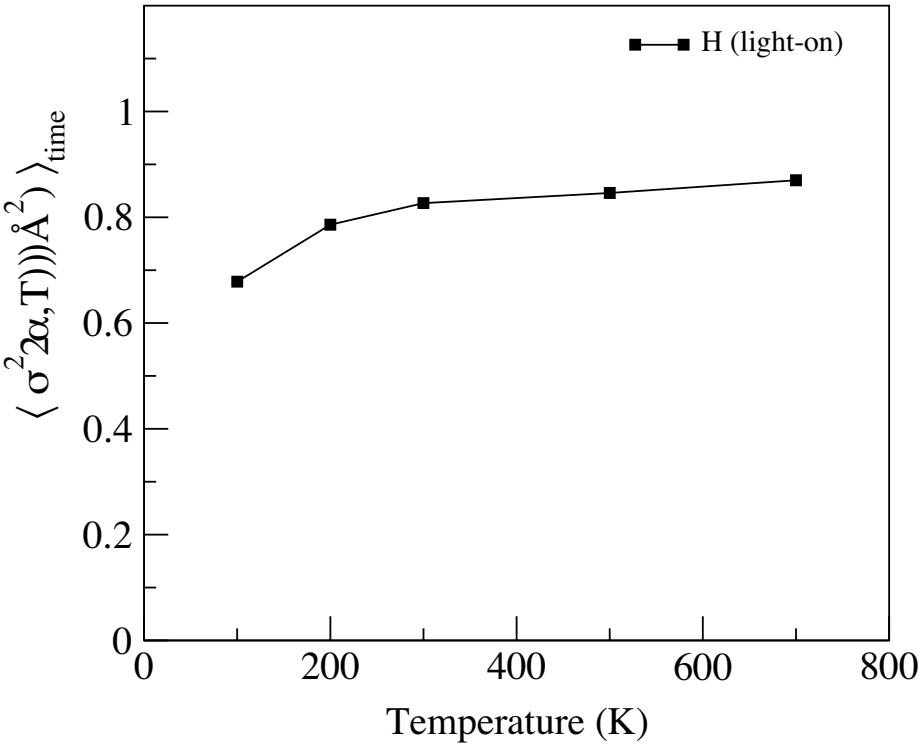

Figure 2.6: Time average mean square displacement for H as a function of temperature of MD simulation in the light excited for $aSi_{61}H_{10}$ [39].

For all the temperatures considered, our simulation results show enhanced diffusion of Hydrogen for the case when the light is "on" as compared with the case where the light is "off". The enhanced diffusive motion of H in the photo excited state relative to the electronic ground state arises from the strong electron-lattice interaction of the amorphous network, and an effect of "local heating" and subsequent thermal diffusion [40] initially in the spatial volume in which the state is localized. The

same calculations has also been performed on the larger model $aSi_{214}H_9$ at T=300K in which, the time average mean square displacement for H is 2.66 Å^2 for the light excited state and 1.10 Å^2 for the electronic ground state. These results again show and confirm a slightly enhanced hydrogen diffusion for the case of light excited state.

2.3 Consequences of hydrogen diffusion

2.3.1 Formation of dihydride structure

In the two scenarios that we considered, MD simulation in electronic ground state ("light off") and simulated light-excited state ("light on") we have observed an important difference. In the locally heated light-excited state, in addition to bond rearrangements and enhanced hydrogen diffusion, we have observed a preferential formation of new structure: SiH_2, with an average distance of 2.39 Å for the pair of hydrogens in the structure, (H-Si-Si-H) and (H-Si Si-H) with H-H separation which ranges from 1.8 Å to 4.5 Å. However, in the electronic ground state, we have obtained rearrangement of atoms including hydrogen diffusion, without formation of SiH_2 structure in the supercell. The mechanisms for the formation of these structures in the light-excited state follows breaking of H atom from Si-H bond close to the dangling bonds (DB) and diffusion to the nearest weakly bonded interstitial sites (or dangling bonds). This mobile H atom then collides (forms a metastable bond) with another Si+DB structure or breaks a Si-Si bond to form another Si-H bond. This is attributed to the fact that the dangling bond site is moving to accommodate the

change in force caused by the additional carrier and also because hydrogen is moving through weakly bonded interstitial sites with low activation barrier for diffusion until it is trapped by a defect [41].

In Fig. 2.7(a)-2.7(f), we have shown the snapshots [42] taken for intermediate steps in the dynamics of the whole cell, in the presence of charge carrier, where emphasis is given to the two hydrogens, which eventually be part of the SiH_2 conformation. For instance, considering the first configuration of $aSi_{61}H_{10}$, the two hydrogens that involved in the formation of the SiH_2 structure initially were about 5.50 Å apart and bonded to two different Si atoms (Si-H) which were separated by about 4.86 Å. When we performed MD simulations, the two hydrogen atoms dissociate from their original host Si and becomes mobile until they form the SiH_2 structure, in which the H-H distance is 2.37 Å which barely changes upon relaxation to 2.39 Å. We have observed similar pattern of H diffusion, bond rearrangements and formation of SiH_2 structure near the DB for the other two configurations considered in the simulation. We have summarized the results that show H-H distance (in SiH_2 structure) in Table 2.5.

We find that there are two different modes of bond formation for the mobile hydrogen. The first is when two mobile hydrogen atoms, H_m, collide with two Si atoms and form a metastable (H-Si-Si-H) or (H-Si Si-H) structure and the second one is when the mobile hydrogen moves until it encounters a preexisting Si-H+DB structure and makes a bond to form a SiH_2 structure. Consequently, our calculations show two basic ideas for the diffusion of H in the light-excited state: 1) the diffusion

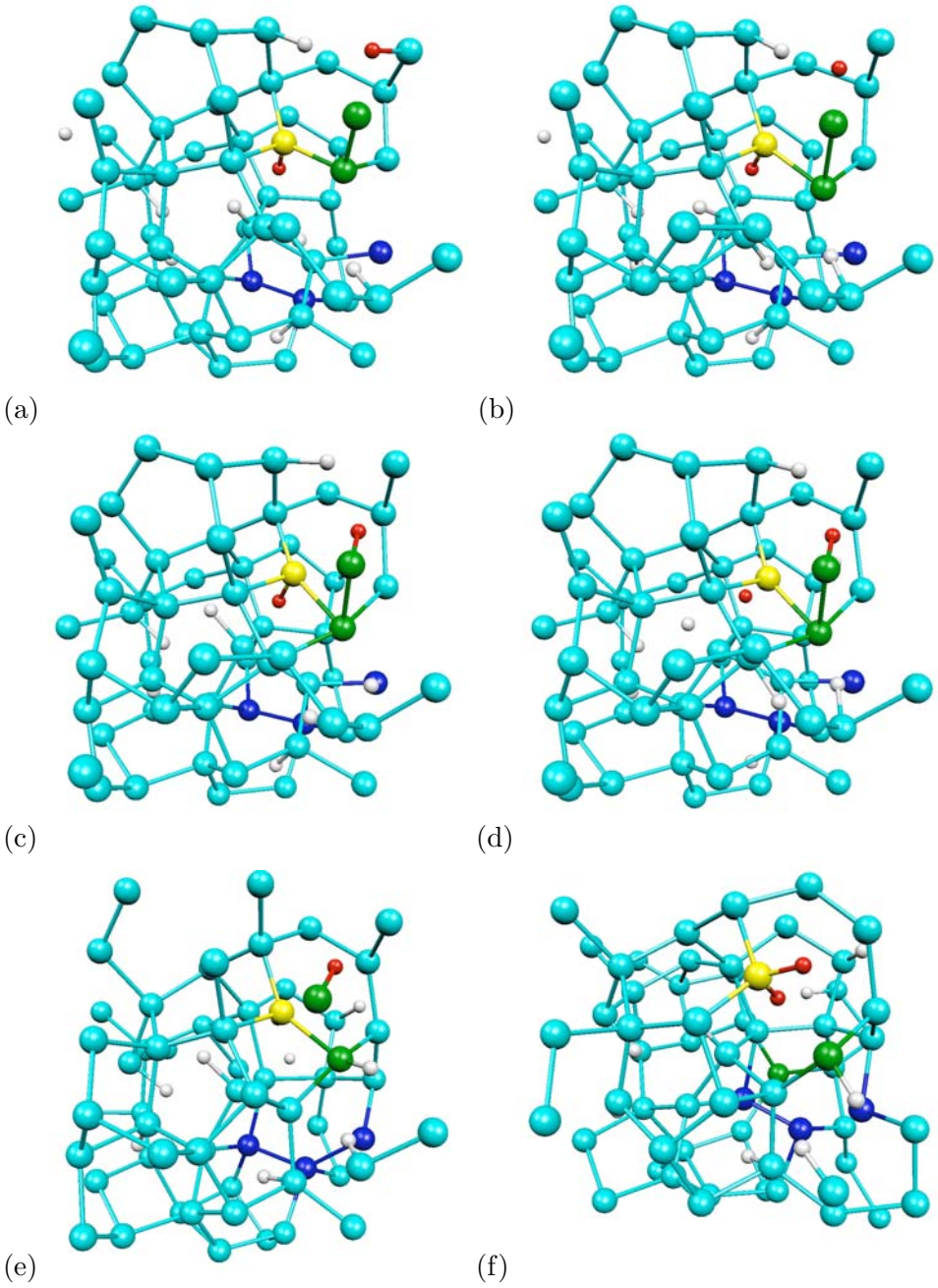

Figure 2.7: A pathway to SiH_2 formation. Thermal MD simulation for the first configuration of $aSi_{61}H_{10}$ in the presence of carriers in the formation of SiH_2 conformation. a) The initial configuration in which the two hydrogens (that eventually form SiH_2) are initially attached to two different Si atoms forming Si-H bond. b) One of the hydrogens dissociates from Si-H and form mobile hydrogen and leaves a dangling bond. c) the mobile hydrogen forms a bond with another Si(db) atom. d) the other H atom also leaves a dangling bond and becomes mobile e) rearrangements of bonds near the defect sites f) The formed SiH_2 structure after being relaxed to the minimum energy. (The two hydrogens that form the SiH_2 structure are shown in red while the Si atom in this structure is shown in yellow, and also we represent the initial defect sites with green and the final defect sites with blue.) [38].

Table 2.5: The H-H distance in the SiH_2 configurations of the system before and after MD simulations in the light excited case [39].

Config--urations	H-H distance before MD (Å)	after MD (Å)
1 ($aSi_{61}H_{10}$)	5.50	2.39
2 ($aSi_{61}H_{10}$)	3.79	2.36
3 ($aSi_{61}H_{10}$)	4.52	2.36
4 ($aSi_{214}H_9$)	3.29	2.45
Average		2.39

of hydrogen doesn't only break a Si-H bond but it also breaks a Si-Si bond and 2) the possibility that two mobile H atoms might form a bond to a single Si atom to form a metastable SiH_2 structure in addition to the formation of (H-Si-Si-H) and (H-Si Si-H) structures.

In $aSi_{61}H_{10}$, the two hydrogens involved in the formation of the SiH_2 structure initially were 5.50 Å apart and bonded to two different Si atoms (Si-H) which were separated by 4.86 Å. With thermal simulation in the light excited state, the two hydrogen atoms dissociate from their original Si atoms and become mobile until they form the SiH_2 structure, in which the H-H distance becomes 2.39 Å. We have observed similar pattern of H diffusion, bond rearrangements and formation of SiH_2 structure near the DB for the other two configurations considered in the simulation. The same phenomenon is observed in the case of $aSi_{214}H_9$. The two hydrogens involved in the formation of the SiH_2 structure initially were 3.29 Å apart and bonded to two differ-

ent Si atoms (Si-H), which were separated by 3.92 Å. With thermal simulation in the light excited state, the two hydrogen atoms dissociate from their original host and become mobile until they form the SiH_2 structure, in which the H-H distance becomes 2.45 Å. We have summarized the results that show before and after MD calculations of H-H distance (in SiH_2 structure) for $aSi_{214}H_9$ and three different configurations of $aSi_{61}H_{10}$ in the case of light excited state in Table 2.5.

We have calculated the time average probability distribution of proton distances for (H-Si-Si-H), (H-Si Si-H), and SiH_2 structures which is shown in Fig. 2.8. From the distribution we obtained that a SiH_2 structure has a higher proton distance of 2.3 Å, the (H-Si-Si-H) has an H-H distance of 2.1 Å, and the (H-Si Si-H) has a lower proton distance of 1.8 Å. This suggest that the recent experiment with the lower value of proton distance is due to a metastable structure of (H-Si-Si-H) and (H-Si Si-H). As we reported in our earlier results the SiH_2 structure has an H-H distance of 2.3 Å.

2.3.2 Change in the electronic properties

In order to understand the electron localization we used the inverse participation ratio, IPR,

$$IPR = \sum_{i=1}^{N} [q_i(E)]^2 \tag{2.2}$$

where $q_i(E)$ is the Mulliken charge [43] residing at an atomic site i for an eigenstate with eigenvalue E that satisfies $\sum_i^N [q_i(E)] = 1$ and N is the total number of atoms in the cell. For an ideally localized state, only one atomic site contributes all the charge

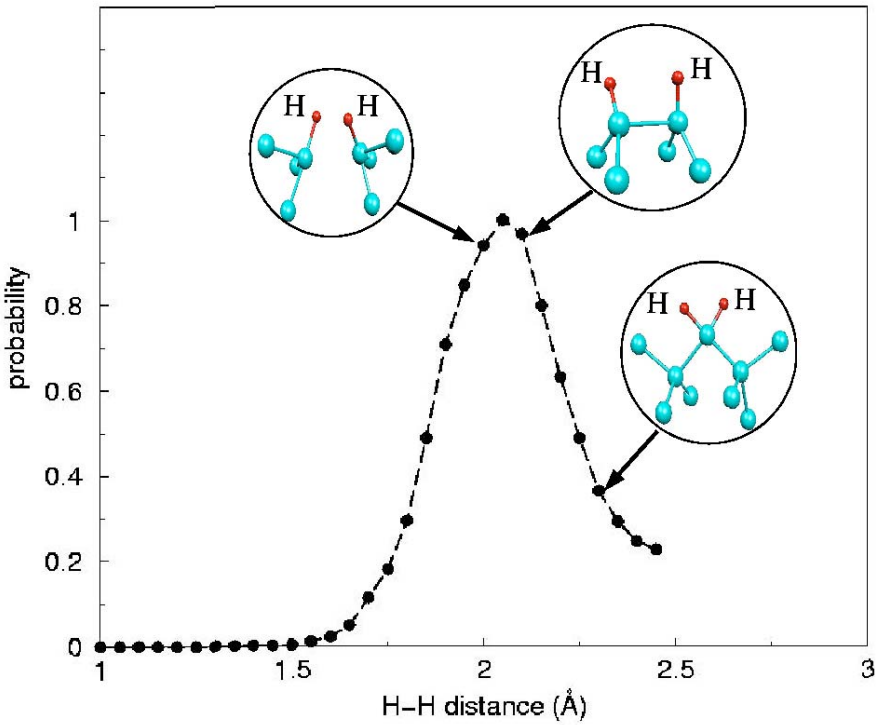

Figure 2.8: Probability distribution for proton separation. Inside we have shown the basic structures with their corresponding average proton distances.

and so IPR=1. For a uniformly extended state, the Mulliken charge contribution per site is uniform and equals $1/N$ and so IPR $= 1/N$. Thus, large IPR corresponds to localized states. With this measure, we observe a highly localized state near and below the Fermi level and a less localized state near and above the Fermi level. These states, highest occupied molecular orbitals (HOMO) and lowest unoccupied molecular orbitals (LUMO), are centered at the two dangling bonds in the initial configuration of the model. The energy splitting between the HOMO and LUMO states is 1.08 eV. Figure 2.9 (a) shows the Fermi level and IPR of these two states and other states as a function of energy eigenvalues in the relaxed electronic ground state.

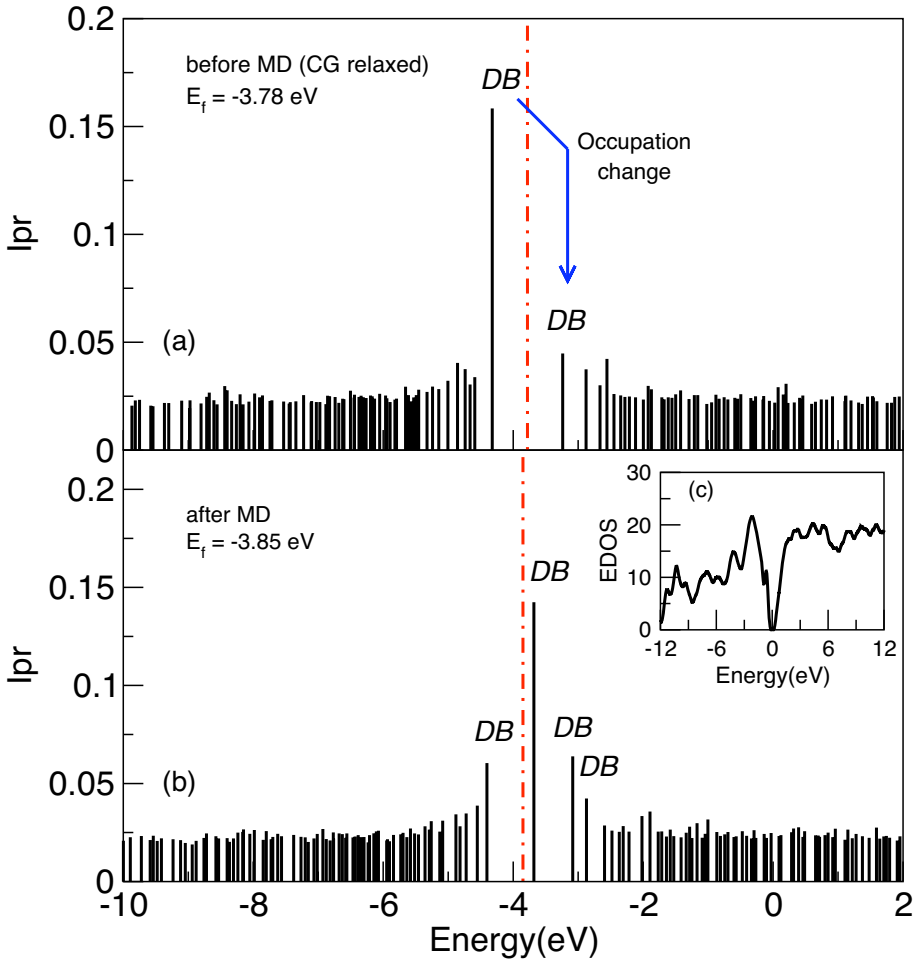

Figure 2.9: The inverse participation ratio of the eigenstates versus the energy eigenvalues, (a) in the relaxed electronic ground state and (b) in the relaxed simulated light-excited state (light excited MD followed by relaxation), with their respective Fermi energy in the first configuration of relaxed $aSi_{61}H_{10}$. The inset (c) shows the electron density of states with the Fermi level shifted to zero for the relaxed simulated light-excited state [39].

This picture changes for the simulated light excited state in which we observe enhanced diffusion of hydrogen and subsequent breaking and formation of bonds. Since electron-phonon coupling is large for localized states [11], the change of occupation causes the forces in the localization volume associated with the DB to change and the system moves to accommodate the changed force. Consequently, the hydro-

gen atoms close to the DB sites start to move in the vicinity of these defects either to terminate the old DB's or to break a weak Si-Si bond and by doing so, create new DB defects on nearby sites. As shown in Fig. 2.9 (b) we observe the formation a highly localized state and appearance of three less localized states, that correspond to the newly formed defect levels after simulated light-soaking. These processes induce transition of electrons from the top of the occupied states to the low-lying unoccupied states, which is reflected in the smaller value of the initial $\mathrm{IPR_{HOMO}}$ and an increase in the $\mathrm{IPR_{LUMO}}$.

$\mathrm{IPR_{HOMO}}$, where the state is initially localized, decreases from 0.158 to 0.060 after photo-excitation, while the $\mathrm{IPR_{LUMO}}$ increases from 0.045 to 0.142. The splitting energy between the HOMO and LUMO states has also declined to 0.723 eV. The newly formed defects with lower energy splitting between the HOMO and LUMO states suggest a presence of carrier induced bond rearrangements in the supercell. The comparisons for the energy and IPR of the system before MD (as relaxed) and after MD is given in Table 2.6.

In addition, analysis of the spatial distribution of the configurations shows that the H atoms close to the dangling bonds (< 4.0 Å) are most diffusive and the Si atoms which make most of the bond rearrangements including the Si atom in the $\mathrm{SiH_2}$ configurations are close (< 5.50 Å) to the dangling bonds. These show the additional charge carrier induces change in the forces around the dangling bonds and consequently rearranges the atoms around the dangling bond sites and eventually

Table 2.6: The energy and the inverse participation ratio IPR of localized states HOMO, LUMO, LUMO+1 and LUMO+2 before and after the MD for $aSi_{61}H_{10}$ [39].

	Eigenvalue		IPR	
	before MD (eV)	after MD (eV)	before MD	after MD
HOMO	-4.32	-4.40	0.158	0.060
LUMO	-3.24	-3.68	0.045	0.142
LUMO+1	-2.88	-3.08	0.037	0.064
LUMO+2	-2.66	-2.87	0.030	0.042

forming an SiH_2 structure. On average the newly formed defect sites are 3.80 Å and 4.70 Å far away from the two initial defect sites. The newly formed SiH_2 structure is (on average) 4.11 Å away from the initial defect sites. It is probable that limitations in both length and time scales influence these numbers, but it is clear that the defect creation is *not* very local because of the high diffusivity of the H.

The same calculation has been performed on $aSi_{214}H_9$. In Fig. 2.10 we have plotted both energy density of states and inverse participation ratio as a function of energy in the light excited state case before and after the MD simulation. As can be seen from the figure we obtained more localized states in the middle of the gap which are caused due to an increase in the number of defects upon light excitation. This supports that the diffusion of hydrogen not only forms preferential dihydride structures but also increase the number of defects in agreement with our findings for the smaller cell $aSi_{61}H_{10}$.

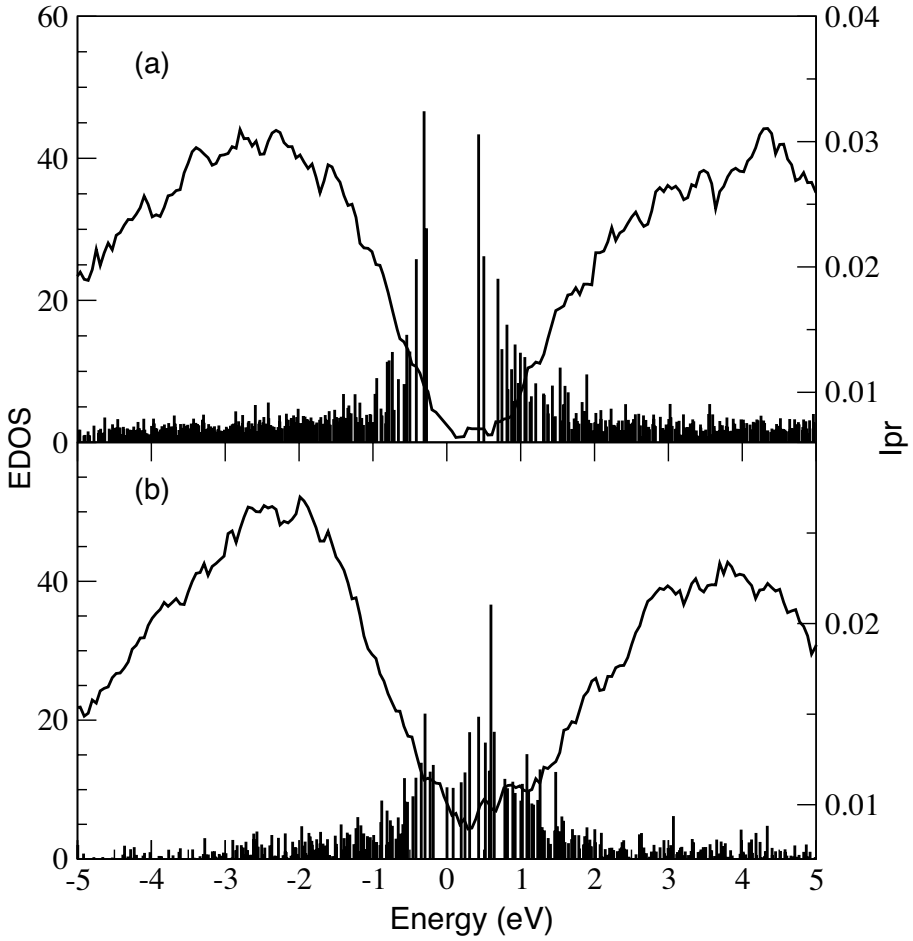

Figure 2.10: The energy density of states and the inverse participation ratio IPR of the eigenstates versus the energy eigenvalues for $aSi_{214}H_9$, (a) in the relaxed electronic ground state and (b) in the relaxed simulated light-excited state (light excited MD followed by relaxation), both the electron density of states and the inverse participation ration are plotted with the Fermi level shifted to zero [39].

2.3.3 Change in the vibrational properties

For an amorphous solid, the vibrational density of state is a sum of $3N$ (N is the number of atoms) delta functions corresponding to the allowed frequency modes. Starting with the relaxed $aSi_{61}H_{10}$ subsequent to MD in the light excited

state, we computed the vibrational energies (vibrational modes) from the dynamical matrix, which is determined by displacing each atom by 0.02 Å in three orthogonal directions and then performing *ab initio* force calculations for all the atoms for each displacement to obtain the force constant matrix, and with diagonalization, phonon frequencies and modes.

In our calculations, the VDOS shows H modes of vibrations in the range (600-900) cm^{-1} and also in the range (1800-2100) cm^{-1}. We have examined the vibrational modes to pick out those modes arising only from SiH_2. We reproduce the vibrational modes of SiH_2 and their corresponding experimental values [44, 45, 46] in Table 2.7. The first mode is the rocking mode at 629 cm^{-1} and 625 cm^{-1}; the second is the scissors mode at 810 cm^{-1} and 706 cm^{-1} and the last is the asymmetric stretching mode that occurs at 2025 cm^{-1} and 2047 cm^{-1} for the first and second configurations respectively. These results are in good agreement with the IR absorption spectra for the SiH_2 structure. The comparison of our results for the vibrational modes of SiH_2 with the experiment is summarized in Table 2.7. The results shown in Table 2.7 are sensitive to the basis sets used in the calculation, in agreement with other work emphasizing the delicacy of H dynamics [47].

In conclusion, we have presented a direct *ab-initio* calculation of network dynamics and diffusion both for the electronic ground state and light-excited state for a-Si:H. We computed the preferential diffusion pathways of hydrogen in the presence of photo-excited carriers. In the light-excited state, we observe enhanced hydrogen

Table 2.7: Frequency for some of the Si-H vibrational modes of the SiH_2 conformation for the first two configurations of the $aSi_{61}H_{10}$ obtained from our MD simulations and their corresponding experimental values [44, 45, 46] [39].

Configurations	Rocking cm^{-1}	Scissors cm^{-1}	Stretch cm^{-1}
1	629	810	2025
2	625	706	2047
Experiment	630	875	2090

diffusion and formation of new silicon dihydride configurations, (H-Si-Si-H), (H-Si Si-H), and SiH_2. This enhanced hydrogen diffusion which introduces a structural change in the network is attributed to the local heating. The two hydrogens in the SiH_2 unit show an average proton separation of 2.39 Å. The results are consistent (a) with the recent NMR experiments and our previous studies, and (b) with the hydrogen collision model of Branz and other paired hydrogen model in the basic diffusion mechanism and formation of dihydride structures. In contrast, simulations in the electronic ground state do not exhibit the tendency to SiH_2 formation. Undoubtedly, other H diffusion pathways exist, and the importance of larger simulation length and time scales as well as effects of promotions involving different states (which could include strain defects and floating bonds [48]) should be undertaken. For the first time, we show the detailed dynamic pathways that arise from light-induced occupation changes, and provide one explicit example of defect creation and paired H formation.

Chapter 3

Thermally stimulated hydrogen emission and diffusion in hydrogenated amorphous silicon

This work has been submitted for publication: T A Abtew, F. Inam, and D A Drabold, submitted (2007).

As one of the materials used in many applications, hydrogenated amorphous silicon has been extensively studied for the last decades. The presence of hydrogen and its diffusion has been connected to the generation of defects and also linked to light induced degradation in these materials [49, 50, 51, 52]. Although there have been number of studies, a complete picture on mechanism for hydrogen diffusion is still missing.

There are number of reports on the diffusion mechanism of H in a-Si:H. The breaking of H from a Si-H and diffusion through a weak interstitial Si-Si bond center, which is followed by hopping among transport sites before it gets trapped at a dangling bond site is the widely accepted model [2, 53, 54, 55, 56, 57]. The existence of an intermediate low-energy pathway which involves a metastable dihydride structure has also been reported [58]. However, by calculating a rate of hopping for different cases

of trapping sites, Fedders argued that thermal motion of hydrogen does not proceed from dangling bond to dangling bond via bond center sites and showed diffusing through the intermediate levels is insignificant [59]. Recently, floating bond assisted H diffusion is also reported. In this model Su *et al*[60] proposed that Si-H bonds do not spontaneously release H, rather with the mediation of a floating bond.

In crystalline Si, the importance of lattice dynamic activated diffusion has been reported [61, 62]. Buda *et al.* [63] has shown diffusion of H in the form of jumps from bond center (BC) site to another BC via intermediate hexagonal or tetrahedral sites.

In this chapter, we present an *ab initio* simulation which reveals the key role of thermal motion of Si atoms in driving H diffusion. We have undertaken accurate simulations including static lattice simulation (in which Si atoms were frozen) and extended thermal simulation. The static lattice shows negligible diffusion as compared with the dynamic lattice case. A key feature of our work is that we determine diffusion mechanisms directly from thermal MD simulation, *not* by imposing a conventional hopping picture among wells (traps) with varying depths. The principal result is that the dynamic lattice (particularly the motion of pairs or triples of Si atoms with a BC H present) is a primary means for ejecting atomic H into the network. This mechanism could not be easily inferred from phenomenological kinetic equation models of H transport [59], though it should readily emerge using a method devised to discover

rare (long time scale) events like the Activation-Relaxation Technique implemented with *ab initio* interactions [64].

To understand the diffusion of H at different temperatures we have used three different models: a 71 atom model $aSi_{61}H_{10}$, a 138 atom model $aSi_{120}H_{18}$, and a 223 atom model $aSi_{214}H_9$ described in Chapter 1. Most of the results presented here are from $aSi_{61}H_{10}$ at T=1000K. The simulations were performed using SIESTA [21]. We used a single ζ polarized basis set for Si valence electrons and double ζ polarized basis for H. We solved the self-consistent Kohn-Sham equations by direct diagonalization of the Hamiltonian. The Γ point was used to sample the Brillouin zone in all calculations. The total MD simulation time is 10ps for $aSi_{214}H_9$, 5ps for $aSi_{120}H_{18}$, and 1ps for $aSi_{61}H_{10}$.

3.1 Toy models

Before analyzing the results from the real models, we present a simple illustration of dependence of Si-H-Si bond angle and Si-Si distance on the energetics of the bond center configurations. Previous work suggests that BC sites are important traps. To elucidate this point we introduce two toy models: a) two silicon atoms with hydrogen near their bond center as shown in Fig. 3.1a and b) two silicon atoms with hydrogen molecule near their bond center as shown in Fig. 3.1b. Dangling bonds of the Si are terminated by H. We generated 170 different configurations by varying the Si-Si distance $R \in$ (2.26-5.40 Å), and Si-H-Si angle $\theta \in (90^\circ - 180^\circ)$. The H ($H_2$) is

maintained equidistant from both Si's. By fixing the two silicons and fixing the H (H_2) at suitable R and θ, we relaxed the configuration to minimize the energy using a double ζ polarized basis for both H and Si. In this way we extract a local picture of the potential surface for H (H_2) near the BC basin.

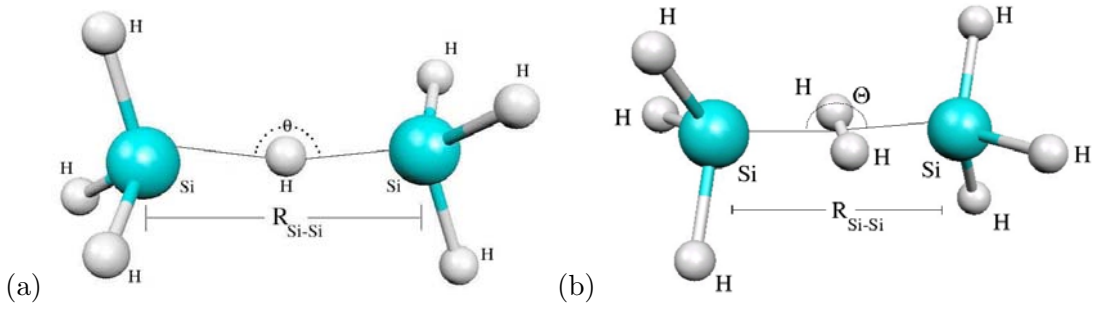

Figure 3.1: Toy models (a) with two Si atoms and seven H atoms where one of the H is kept near the bond center and (b) two Si atoms and eight H atoms where H_2 is kept near the bond center.

As expected, in the case of H at the bond center, a well defined minimum exists, with significant dependence upon both R and θ. In real a-Si:H parameters R and θ depend upon the local geometry (and its time-dependence arising from thermal motion of the atoms). Such motion may push the H into an unfavorable part of the $R-\theta$ configuration space, thus inducing emission. To quantify this, in Fig. 3.2a, we show the total energy surface of the system as a function of R and θ. The probability of hydrogen diffusion is highest on the red region and lowest on the green region. The energy spectrum shows a broader range of Si-H-Si angles ($\theta \in$120°-180°) with a range of Si-Si bond length $R \in$ 3.5-4.5 Å to have a stable bond center configuration. In the case of H_2 at the bond center, a large flat region with energy minima shown in

green (light grey) exist in the $R-\theta$ configuration space as shown in Fig. 3.2b. The presence of the large local energy minima in the $R-\theta$ configuration space allows the H_2 molecule to easily diffuse and explore the network with large degree of freedom unlike the H.

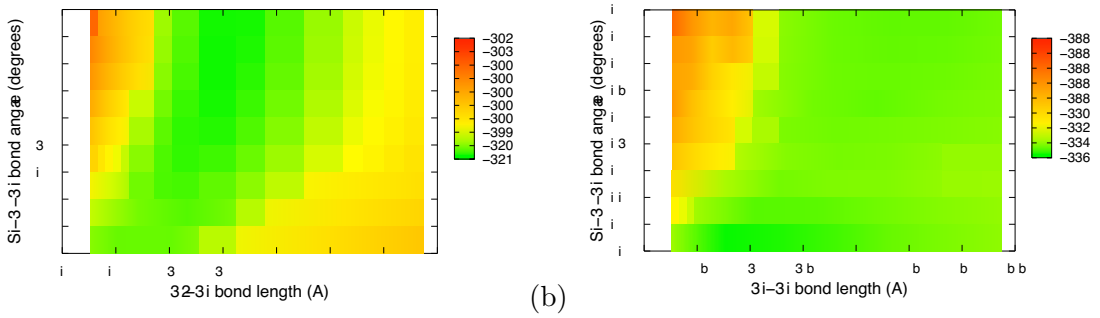

Figure 3.2: The projection of the total energy surface of (a) the Toy Model (Fig. 3.1a) and (a) the Toy Model (Fig. 3.1b). The potential well is deepest for green and shallow for red. Units of energy are eV.

3.2 Diffusion mechanism

To analyze the role of thermally induced Si motion in driving H diffusion, we considered results from $aSi_{61}H_{10}$ both at T=300K and T=1000K. The higher temperature simulation help us to see many more events of lattice vibration in a decent amount of time keeping the solid phase.The difference in the H diffusion for these two cases is clearly observed from the time average mean squared displacement ($\langle\sigma^2\rangle$) of H which yields an average mean square displacement of 0.14 Å^2 and 0.74 Å^2 for T=300K and T=1000K respectively. The same analysis for Si gives an average mean square displacement of 0.06 Å^2 and 0.56 Å^2 for T=300K and T=1000K respectively.

These results show that the thermal motion of Si atoms are crucial in enhancing the diffusion process of H. The MSD of Si and H for two different temperature 300K and 1000K is shown in Fig. 3.3.

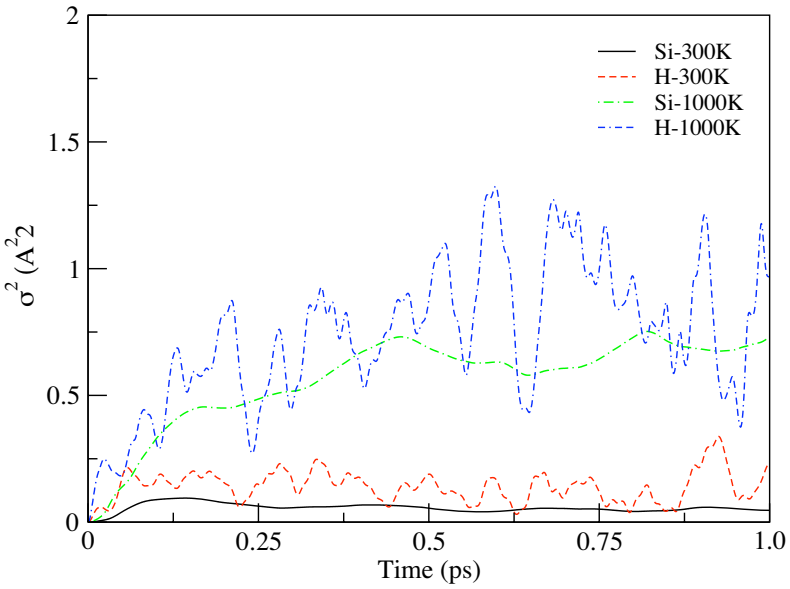

Figure 3.3: The average mean square displacement of Si and H in the $aSi_{61}H_{10}$ for two different temperatures.

The results from the dynamic lattice clearly show the effect of thermal motion of Si atoms on neighboring H. These Si atoms determine the fate of H either to diffuse out or to get trapped. There are basically three parameters defining the diffusion mechanisms: neighboring Si-Si distance (R_{Si-Si}), Si-H-Si bond angle and formation of H_2 molecule.

We determine one essential mechanisms for H diffusion in the dynamic lattice namely, "Fluctuating Bond Center Detachment" (FBCD) diffusion: if the H is initially covalently bonded to a Si atom, it stays bonded with it until another Si

comes in the vicinity and makes an instantaneous or fluctuating BC configuration. This event is followed by a switching of H from the covalent bond to the new Si to either form another Si-H bond or hop, depending upon the local environment. This process is important both as a means for the network to generate free H and to create dangling bonds. The mechanisms we report here are undoubtedly not the sole means of obtaining H diffusion, but are predominant in accurate and relatively extended MD simulations.

MD simulation reveals various traps: the bond center site (BC), a geometrical center site (GC), which is analogous to the T site in the crystalline Si, and a weakly bonded Si site. By BC, we refer to a H configuration with $\theta \in$ (120°-180°), and $R_{\text{Si-Si}}$ $\in$ (3.0-5.0 Å). The GC site is a region where four or more Si atoms in close proximity form a closed loop (ring) that attracts H to the center. In Fig. 3.4, we have plotted,

$$\rho(R,\theta) = \sum_i \sum_j \delta(R - R_i(t))\delta(\theta - \theta_j(t)), \tag{3.1}$$

a distribution function indicating time spent in different parts of the $R - \theta$ configuration space, where $R_i(t)$ is the distance between two Si atoms at a time, and $\theta_j(t)$ is a bond center angle (Si-H-Si) formed by two silicons and a central H at a given time, by considering only those H positions which fall near the BC of the two neighboring Si atoms sampled over all H. These results show preferred values of R, ranging from 3.0-4.0 Å and θ (Si-H-Si bond angle) in the range of 110°-170° where the H atoms spends more time. The hydrogen trapping time is highest on the red and lowest on

the green regions. Note that the result in Fig. 3.4 is qualitatively consistent with the energy surface from the toy model Fig. 3.2a.

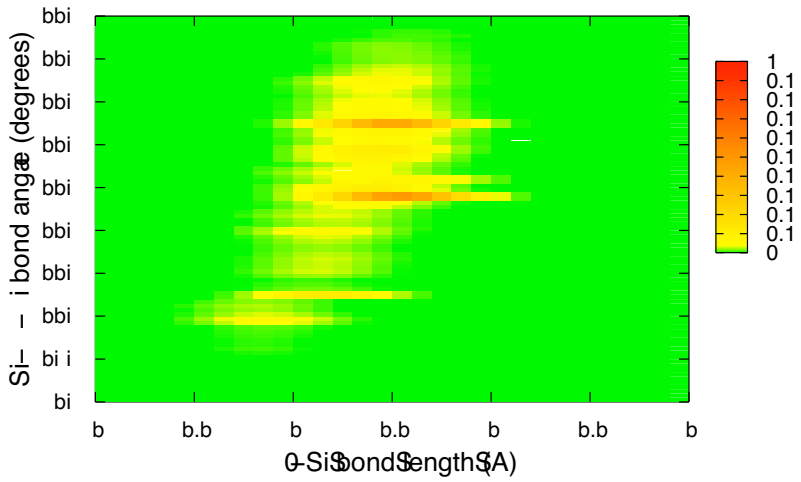

Figure 3.4: The normalized temporal distribution of $R_{Si\text{-}Si}$ as a function of Si-H-Si bond angle from $aSi_{61}H_{10}$ for a total of 1ps at T=1000K: red, most frequent visitation and green least frequent.

A hydrogen atom near a bond center will remain there with only local fluctuations so long as preferred R and θ are maintained. However, thermal fluctuation in the positions of neighboring silicon atoms induces instability in the Si-H-Si configurations. As a consequence, the thermal motion of Si squeezes out H to enable subsequent motion (transfer to passivate a dangling bond, hop to another trapping center, or possibly merge with another free H to form H_2). Substantial thermally-induced fluctuation of local Si bonding at modest temperatures has been observed in earlier work [66].

We have counted the number of bond breaking events and the pattern of diffusion. In the case of $aSi_{61}H_{10}$, for T=1000K, we have observed 3 bond breaking

events which are accompanied by rapid bond switching in 1ps simulation time. For $aSi_{214}H_9$ at 300K we have observed 5 major bond breaking events in the 10ps simulation time; all are FBCD assisted. After the bond breaking, all of the events lead to the hydrogen passivating a dangling bond.

The details of BC related hopping events depend upon the distance between the two Si atoms and the Si-H-Si angle formed by this configuration. The the probability of breaking Si-H bonds increases with the average MSD of Si and enhances the probability of FBCD. To illustrate this point, in Fig. 3.5, we have plotted the probability of finding H in BC site versus the average displacement of Si for different temperatures using three models, $aSi_{61}H_{10}$, $aSi_{214}H_9$, and $aSi_{120}H_{18}$ with a simulation time of 1ps, 10ps and 5ps respectively. The results show that the probability to form a bond center falls on a linear curve revealing a model-independent mechanism of H hopping which is controlled mainly by the motion of Si.

3.3 FBCD assisted diffusion

To discuss the FBCD mechanism in detail, we have selected three H from $aSi_{61}H_{10}$ model namely H_{67}, H_{68}, and H_{71} which diffuse through via FBCD. To analyze the role of the thermal motion of the neighboring Si atoms we tracked all nearby Si pairs correlated with the motion of H in all the three cases for 1ps at T=1000K.

In Figure 3.6(a), we show a situation in which H_{67} initially bonded to Si_{35} switched to Si_{46}. This event follows the close approach of Si_5 to the Si_{35}-H_{67} bond and

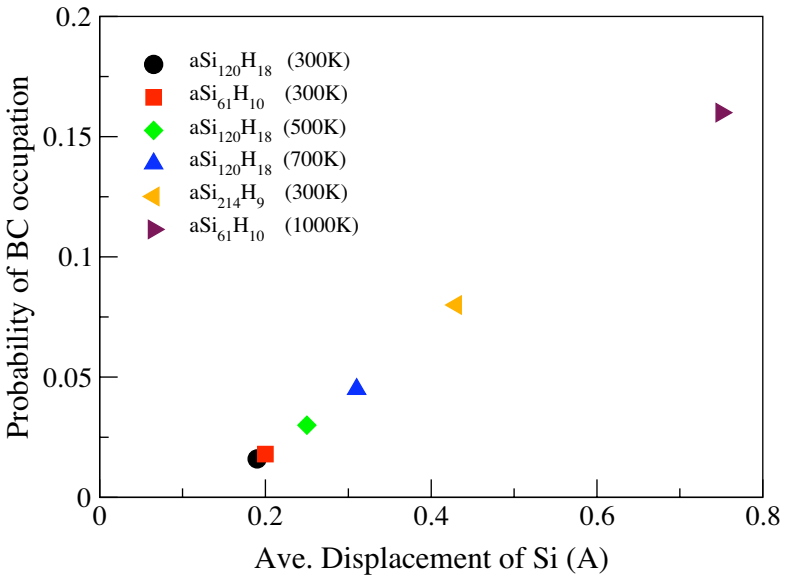

Figure 3.5: The probability of occupying a BC site.

forms a fluctuating bond center conformation. As the bond length Si_{35}-Si_5 changes from 4.0 Å to 2.9 Å as shown in Fig. 3.6(b), the bond angle Si_{35}-H_{67}-Si_5 changes from a bond center configuration 130° to 85° as shown in Fig. 3.6(c), compelling the H to diffuse and form a bond with another Si. This process happened twice (at 0.20ps and 0.63ps).

A second case for the FBCD assisted diffusion involves H_{68} similar to the previous example. As shown in Fig. 3.7(a), we observe a bond breaking process in H_{68}, a situation where H_{68} which was initially bonded to Si_{48} and later switched to Si_{36}. The switching occurs due to the close approach of Si_{39} to the Si_{48}-H_{68} bond and forms a fluctuating bond center conformation. As the bond length Si_{48}-Si_{39} changes from 4.2 Å to 3.0 Å as shown in Fig. 3.7(b), the bond angle Si_{48}-H_{68}-Si_{39} changes

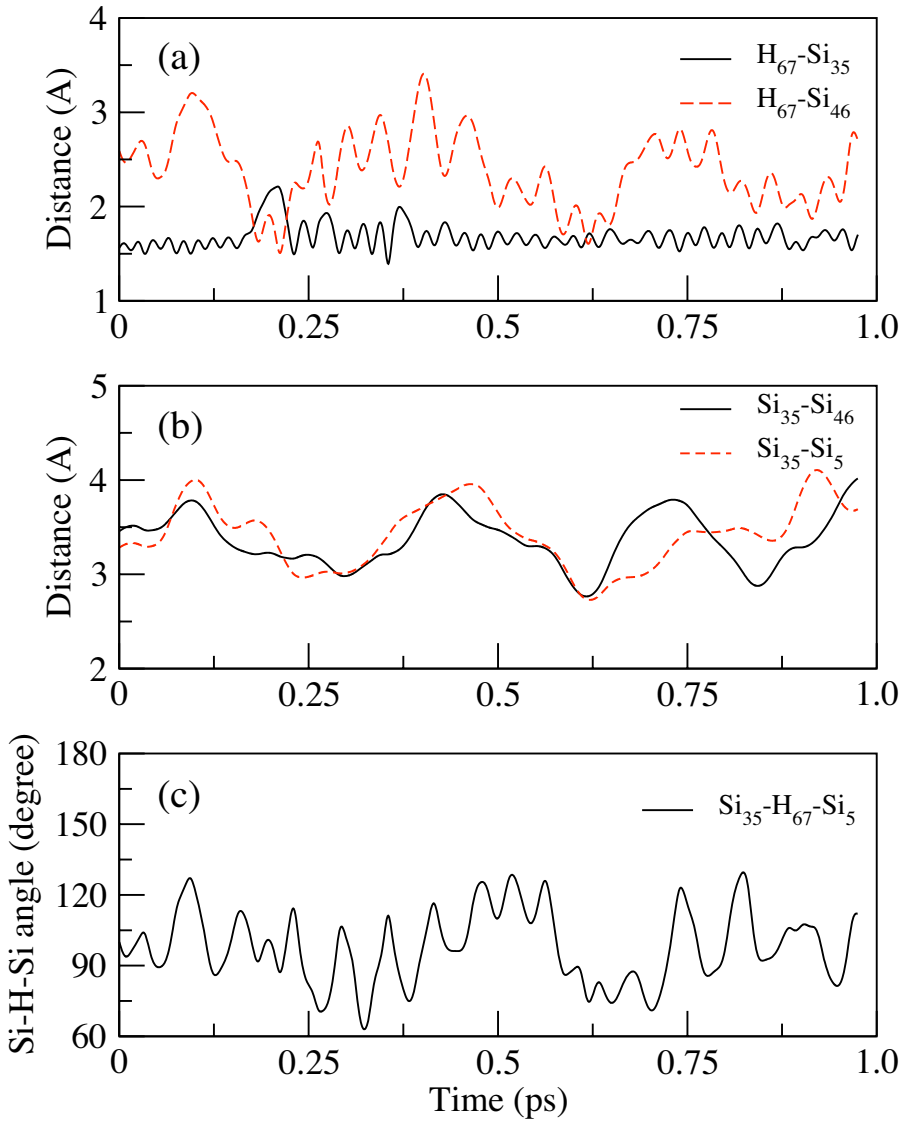

Figure 3.6: The distance between selected H-Si bonds, Si-Si bond and bond angle Si-H-Si which represent FBCD assisted diffusion mechanisms for the case of H_{67} in $aSi_{61}H_{10}$.

from a bond center configuration 150° to 89° as shown in Fig. 3.7(c). Once the BC environment is lifted the configuration is no more a local minima which forces the H to diffuse out.

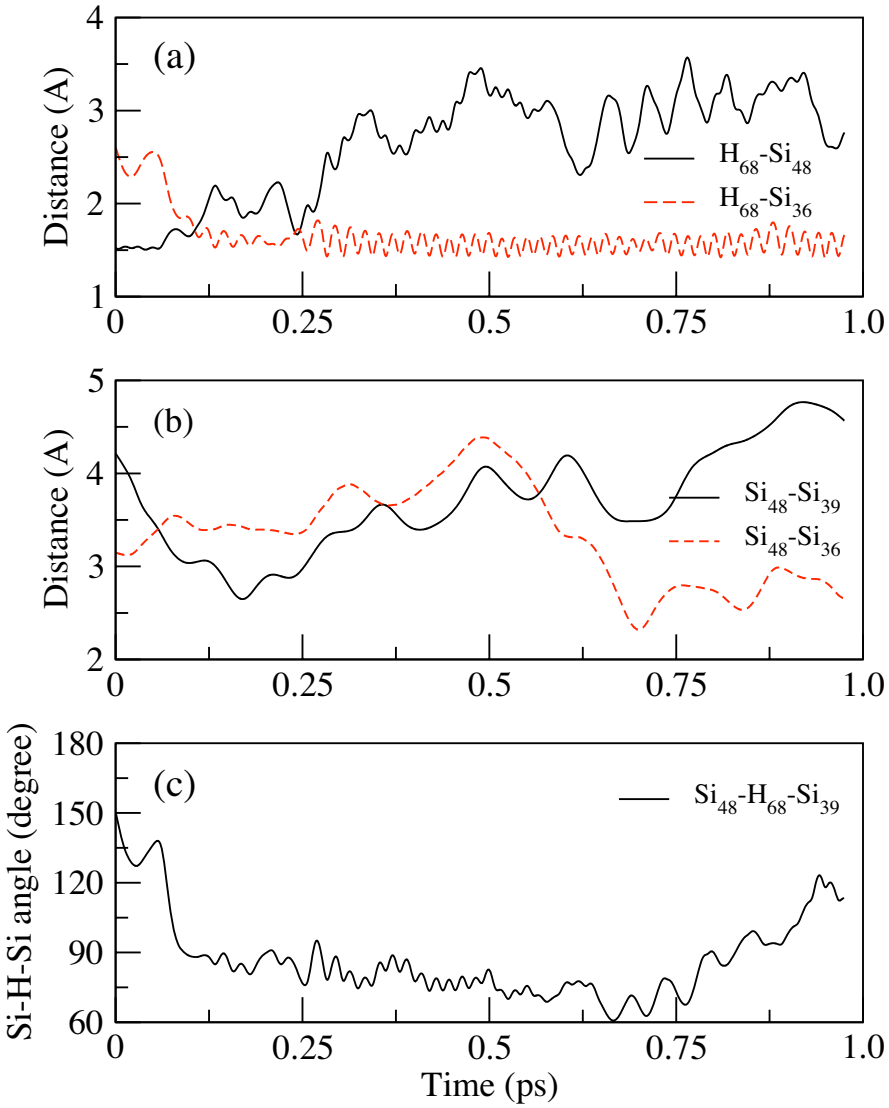

Figure 3.7: The distance between selected H-Si bonds, Si-Si bond and bond angle Si-H-Si which represent FBCD assisted diffusion mechanisms for the case of H_{68} in $aSi_{61}H_{10}$.

The third case involves H_{71}, where we have observed the FBCD mechanism to switch a bond from Si_{54} to Si_{49}. This event occured when Si_{54}-Si_{49} bond length changes from 3.5 Å to 2.5 Å which allow Si_{49} to break the bond center configuration formed by Si_{54}-H_{71}-Si_{54} by changing the bond angle from 120° to 80°. This process

is shown in Fig. 3.8(a)-(c). The FBCD assisted diffusion is the same in the other models.

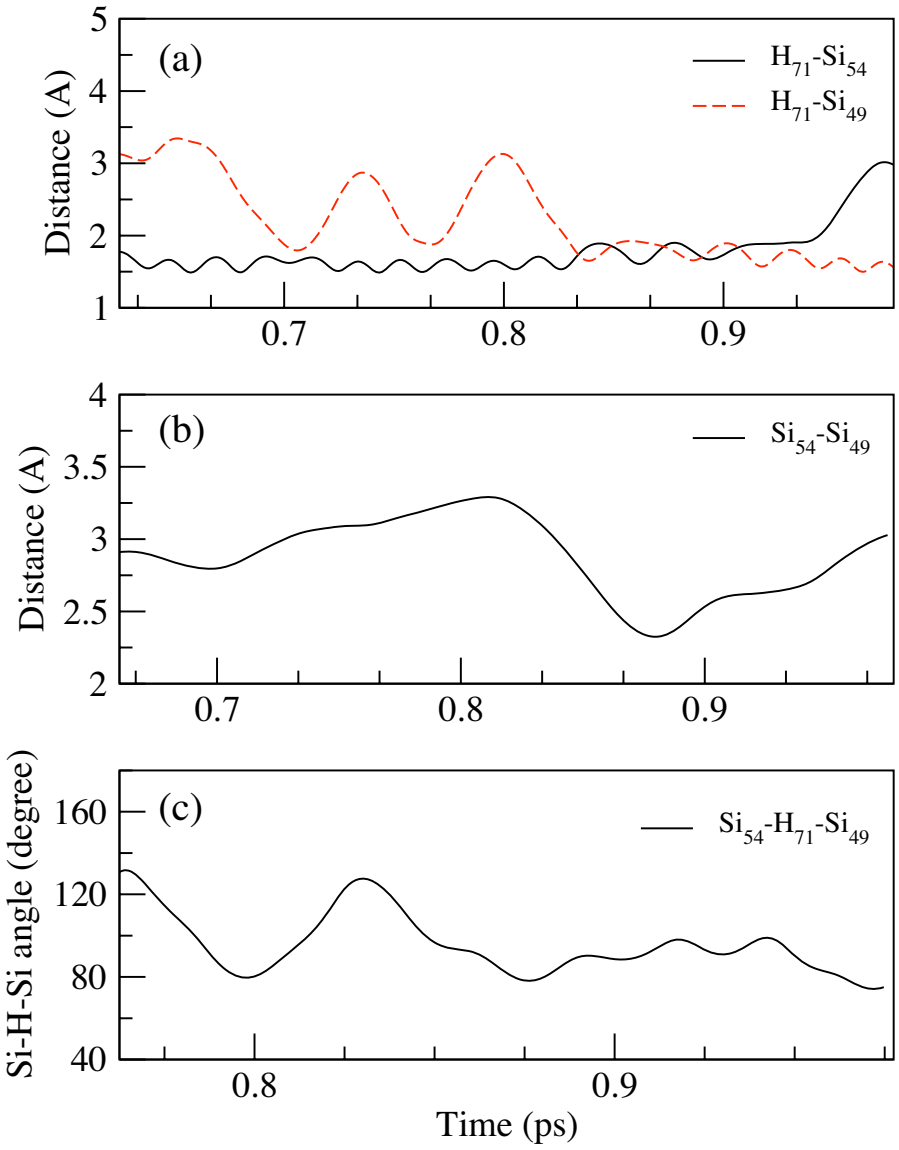

Figure 3.8: The distance between selected H-Si bonds, Si-Si bond and bond angle Si-H-Si which represent FBCD assisted diffusion mechanisms for the case of H_{71} in $aSi_{61}H_{10}$.

The FBCD mechanism is reminiscent of that of Su *et al.* [60], also depending upon the intercession of a Si not part of the initial conformation. However, the FBCD is a more general process that may or may not increase the Si coordination. We found many cases of H detachment in which no Si was overcoordinated. Ejection of H is a more subtle process than just changing coordination, and depends on the the local geometry (R, θ). Finally, all such FBCD conformations arise from fluctuations, and are thus short lived [66]. The mechanism of Su *et al* is a special case of FBCD.

In conclusion, we have demonstrated the nature of H diffusion in a-Si:H by direct simulation and with the aid of a model to develop a fairly simple picture of H motion. H emission is stimulated by Si motion, and the FBCD mechanism is shown to be important both for stripping off H chemically bonded to Si (thus creating "free" atomic H), and of course for creating Si dangling bonds. Our work is consistent with analogous studies in c-Si [63], and is a generalization of the work of Su and Pantiledes [60].

Chapter 4

Ab initio models of a-$Si_{1-x}Ge_x$:H alloys

The results presented in this chapter are published: T A Abtew and D A Drabold, Phys. Rev. B **(75)** *045201 (2007).*

Hydrogenated amorphous Si-Ge alloys are important materials for uncooled microbolometer applications, especially "thermal" night vision and IR sensing [69, 70]. The materials are of basic interest as they exhibit a mild form of alloy disorder (here "mild" refers to the chemical similarity of the two species) juxtaposed with topological disorder. Since the band gap of these alloys can be tuned by changing composition, they are being used and explored for photovoltaic applications [71, 72, 73]. The electrical, optical and vibrational properties have been studied from experiment [74, 9, 75, 76].

There are a number of experimental investigations on the bonding in amorphous $Si_{1-x}Ge_x$ alloys (both with and without hydrogen). Using extended x-ray absorption Nishino *et al* [77] found the Ge–Ge and Ge–Si bond lengths to be independent of composition (2.46 Å and 2.41 Å respectively). This is consistent with another X-ray absorption measurement by Incoccia *et al* [78] a few years before. On the other hand, for the non-hydrogenated alloys researchers showed a linearly increas-

ing bondlength as a function of concentration [79, 80, 81, 82] opposing the idea of "composition independent" bond length. However, there is limited understanding of whether the difference is connected to the presence of hydrogen in the alloy or not.

There are many simulations of a-Si and a-Si:H [83, 84, 85, 86, 87, 88]. Most of these studies provide networks in reasonable agreement with experiment, using a variety of different approaches. Our aim here is to offer small but reliable models of a-SiGe:H alloys, studying the effect of Ge concentration on bond length and on the structure of the amorphous network. Wherever possible, we compare the models to experiment, and to make new specific predictions of the structural origins of defect states appearing near the Fermi level. It seems likely that because of delicate energetics of alloy disorder, relaxation effects and (mild) charge transfer, a first principles approach is needed.

In this chapter we describe procedures for generating a-$Si_{1-x}Ge_x$:H alloy models, and discuss the approximations and parameters used in the *ab initio* code employed. We present a thorough analysis of structural properties by studying partial pair correlations, atomic coordination and bond angle distributions. The electronic properties of localized mid-gap and band-tail states are also analyzed. From the standpoint of band gap engineering, we describe the evolution of state density as a function of composition. The dynamical properties and vibrational density of states are also studied with a comparison to existing experiment.

The density functional calculations in the present work were performed within the generalized gradient approximation [26] (GGA) using the first principles code SIESTA [21]. Calculations in this paper employed single ζ basis with polarization orbitals (SZP) for Si and Ge and a double ζ polarized basis (DZP) for hydrogen [89]. The structures were relaxed using conjugate gradient (CG) coordinate optimization until the forces on each atom were less than 0.02 eV/Å. We solved the self-consistent Kohn-Sham equations by direct diagonalization of the Hamiltonian and a conventional mixing scheme. The $\Gamma(\vec{k} = 0)$ point was used to sample the Brillouin zone in all calculations.

After relaxation of $aSi_{214}H_9$ model as described in Chapter 1, we replaced some of the Si atoms by Ge atoms at random, and then again relaxed the newly formed alloy using conjugate gradient minimization to generate a-$Si_{1-x}Ge_x$:H alloys, with the Ge fraction x being 0.1, 0.2, 0.3, 0.4 and 0.5. We note that our models have the advantage that they are a minimum for an accurate energy functional. On the other hand, because of the *a priori* assumption of a tetrahedral a-Si network, and no possibility for modeling diffusive processes because of the rapid descent into a minimum, it is likely that our models will tend to underestimate disorder effects associated with alloying. Like other calculations of this sort the justification is partly *a posteriori*: namely agreement with a variety of experiments.

4.1 Structure

4.1.1 Bond length and pair correlation functions

For a given Ge atomic composition, x, we obtained the average bond lengths between Si–Si, Si–Ge, and Ge–Ge. In Fig. 4.1 we show these bond lengths as a function of Ge composition. The experimental data which are obtained for Ge composition $x \geq 0.3$ from Nishino *et al* are shown in Fig. 4.1. For these compositions, our result shows linear bond length distribution as a function of composition. By taking an average value of each type of bond for all the compositions, we obtained mean bond length value of 2.42 Å for Si–Ge and 2.46 Å for Ge–Ge bonds which are in good agreement with the experimental values of 2.46 Å and 2.41 Å [77, 81]. Our result give a mean bond length of 2.37 Å for Si–Si bond which is again in the experimental range of 2.35–2.37 Å [90].

The topology of models may be analyzed by partial pair correlation functions $g_{\alpha\beta}(r)$ of atomic species α and β. The partial pair correlation $g_{\alpha\beta}(r)$ can be written as

$$g_{\alpha\beta}(r) = \frac{1}{4\pi r^2 \rho N c_\alpha c_\beta} \sum_{i \neq j} \delta(r - r_{ij}) \tag{4.1}$$

where N is the total number of particles in the system; $\rho = \frac{N}{V}$ is the number density , $c_\alpha = \frac{N_\alpha}{N}$ and $c_\beta = \frac{N_\beta}{N}$. We have used a Gaussian approximation for the delta function with broadening $\sigma = 0.1$ Å.

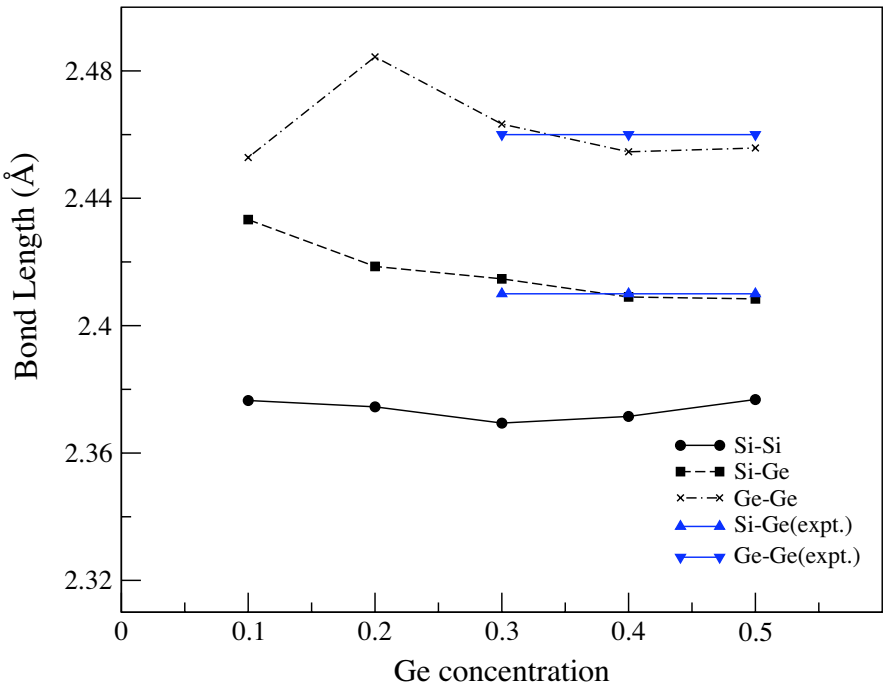

Figure 4.1: Si–Si, Si–Ge and Ge–Ge bond lengths as a function of Ge concentration. The straight lines with triangle up and triangle down symbols are experimental values of Si–Ge and Ge–Ge bond lengths respectively taken from Nishino *et al* [77].

We have analyzed the five alloy compositions, and a first nearest neighbor peak with subsequent deep minimum is always evident. These features imply strong short-range ordering in the models. In Fig. 4.2 we plot the partial pair correlation for Si–Si, Ge–Ge, and Si–Ge in the a-$Si_{1-x}Ge_x$:H alloy for x=0.1 and x=0.5. For Ge–Ge we obtained a first peak at r_o ∼2.46 Å which is the same for the two compositions considered. Similarly, the partial correlation for Si–Ge has a first peak at 2.42 Å and Si–Ge has first peak at 2.37 Å. We observed considerable similarity in first nearest neighbor peaks for the various Ge concentrations. These results support and repro-

duce values observed in experiment [77, 81, 90]. Our models retain an essentially tetrahedral structure for all Ge concentrations.

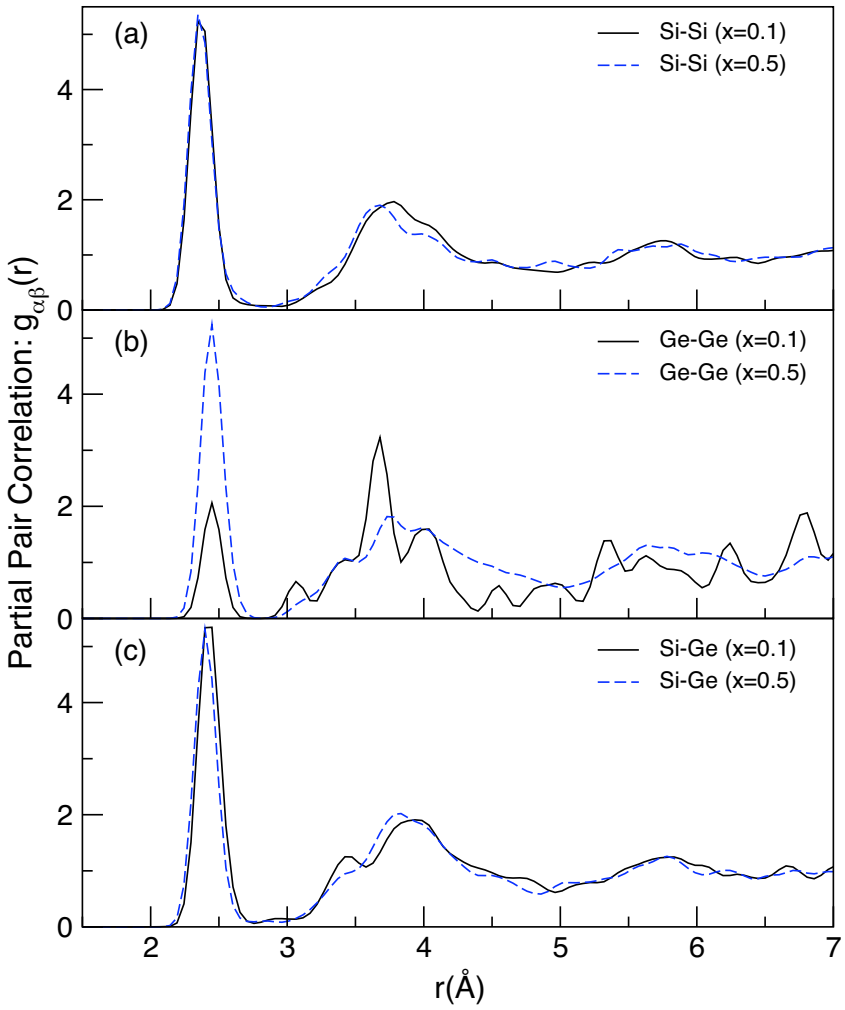

Figure 4.2: Partial pair distribution function $g_{\alpha\beta}$ of a-$Si_{1-x}Ge_x$:H alloys for two compositions (x=0.1 and x=0.5): (a) Si–Si, (b) Ge–Ge, and (c) Si–Ge.

4.1.2 Geometry of bonding

The tetrahedral a-Si (WWW) model ancestral to the alloy models we present here is fully coordinated (fourfold coordination for all the Si atoms). Thus, random

substitution of Ge without relaxation preserves the fourfold tetrahedral structure. The essential difference between the model with random substitution (without relaxing) and the fully relaxed case (the models we present in this paper) is that we see a decrease in the number of fourfold atoms (through creation of both threefold and fivefold atoms) as the Ge content increases. There is also an increase in weak (long) bonds. These changes influence all physical properties of the alloy systems. Like any *ab initio* simulation, the detailed numerics of our calculations must be taken with a grain of salt: the systems, while large by the standards of first principles studies, do not provide statistical error bars on coordination and defects. It is reasonable however to expect general trends to be reproduced as a function of x.

We obtained partial n_{Ge}, n_{Si}, n_{H}, and average coordination numbers, n, based on the nearest neighbor distance determined in the preceding section; first neighbor coordination numbers n_{SiSi}, n_{SiGe}, n_{SiH}, n_{GeGe}, n_{GeSi}, and n_{GeH} are obtained by integrating the pair correlation function $4\pi r^2 \rho g_{\alpha\beta}(\mathrm{r})$. The results are shown in Table 4.1. The total coordination numbers for Ge, Si and H are, $n_{\mathrm{Ge}} = n_{\mathrm{GeGe}} + n_{\mathrm{GeSi}} + n_{\mathrm{GeH}}$, $n_{\mathrm{Si}} = n_{\mathrm{SiSi}} + n_{\mathrm{SiGe}} + n_{\mathrm{SiH}}$, and $n_{\mathrm{H}} = n_{\mathrm{HSi}} + n_{\mathrm{HGe}}$ respectively. The observation of higher coordination number for composition x=0.5 is due to a net increase in over-coordinated (fivefold) bonds vs. under-coordinated (threefold) bonds. It is not obvious that total coordination of 4.09 at $x = 0.5$ is statistically significant; this will be checked in future work with extended annealing studies. The salience of these changes to the electronic structure of the alloy is discussed in section 4.2.

Table 4.1: The value of r_o in the first peak of the g(r) and the first neighbor coordination number $n_{\alpha\beta}$ in a-$Si_{1-x}Ge_x$:H alloys for five different Ge atomic compositions x=0.1–0.5. The integration ranges are from 0.0–2.8 Å for Si–Si, Ge–Ge, Si–Ge, Ge–Si, and 0.0–1.8 Å for Si–H, Ge–H, H–Si, and H–Ge.

Bond type	r_o(Å)	$n_{\alpha\beta}$ for first shell (x=0.1)	(x=0.2)	(x=0.3)	(x=0.4)	(x=0.5)
Si–Si	2.37	3.47	3.07	2.70	2.37	2.06
Si–Ge	2.42	0.50	0.86	1.22	1.54	1.97
Si–H	1.53	0.04	0.05	0.05	0.05	0.06
	n_{Si}	4.01	3.98	3.97	3.96	4.09
Ge–Ge	2.46	0.16	0.71	1.11	1.58	1.92
Ge–Si	2.42	3.80	3.22	2.80	2.34	2.04
Ge–H	1.60	0.04	0.02	0.03	0.02	0.03
	n_{Ge}	4.00	3.95	3.94	3.94	3.99
H–Si	1.53	0.89	0.89	0.78	0.78	0.67
H–Ge	1.60	0.11	0.11	0.22	0.22	0.33
	n_{H}	1.00	1.00	1.00	1.00	1.00

To investigate the effect of Ge composition on the structures, we analyzed and obtained all types of bonding and structures in the network for each Ge compositions considered. For x=0.1, about 96.81% of Si and 95.83% of Ge are fourfold, only 1.06% of Si and 4.17% of Ge are threefold coordinated, 2.13% of Si are fivefold. No fivefold coordination is obtained for Ge. Where fourfold Si is concerned, Si_4 (a Si atom bonded with four Si atoms) is a dominant structure which is followed by Si_3Ge (a Si atom bonded with three Si and one Ge atoms). We observed a similar pattern in the Ge fourfold coordination that Ge bonded to Si_4 structure is highly dominant which is followed by Ge bonded with Si_3Ge. The detailed results are shown in Table 4.2.

Table 4.2: Average percentage $m_\alpha(l)$ (bold characters) of atoms of species Si and Ge, l–fold coordinated at a distance of 2.68 Å for both Si and Ge, and 1.55 Å for H in a-$Si_{1-x}Ge_x$:H alloy for Ge atomic composition x=0.1. We also give the identity and the number of Ge and Si neighbors for each value of $m_\alpha(l)$.

Si				*l = 3*	**1.06**
				Si_3	0.53
				Si_2Ge	0.53
l = 4	**96.81**	*l = 5*	**2.13**		
Si_4	52.67	Si_5	1.06		
Si_3Ge	32.98	Si_4Ge	1.06		
Si_2Ge_2	6.91				
Si_3H	3.72				
Si_2GeH	0.53				
Ge		*l = 3*	**4.17**	*l = 4*	**95.83**
		Si_3	4.17	Si_4	79.17
				Si_3Ge	12.50
				Si_2GeH	4.17

In the case of x=0.5, we observed ∼10.47% fivefold bonds for Si. About 87.21% of Si and 99.04% of Ge are fourfold, only 2.33% of Si and 0.96% of Ge are threefold coordinated. The dominant structure in this case is a Si atom bonded with Si_2Ge_2, followed by Si_3Ge. A similar pattern is observed in the Ge fourfold atoms. The results are shown in Table 4.3. Comparing the bonding statistics of the relaxed network with the initial configuration (in which we randomly substituted Ge for Si), we see a significant decrease in the number of four-fold atoms. Also, we observe an increase in the number of weak bonds ($\sim$ 9.5%) for the case of x=0.5. The increase in weak bonds in this case is relative to the number of such bonds in the case of x=0.1.

Here, weak bond refers to a Si–Si or Si–Ge bond with bond length between 2.5 Å to 2.7 Å.

Table 4.3: Average percentage $m_\alpha(l)$ (bold characters) of atoms of species Si and Ge, l fold coordinated at a distance of 2.68 Å for both Si and Ge, and 1.55 Å for H in a-$Si_{1-x}Ge_x$:H alloy for Ge atomic composition x=0.5. We also give the identity and the number of Ge and Si neighbors for each value of $m_\alpha(l)$.

Si				*l = 3*	**2.32**
				Si_2Ge	1.16
				Si_3	1.16
l = 4	**87.21**	*l = 5*	**10.47**		
Si_2Ge_2	51.16	Si_4Ge_1	3.49		
Si_3Ge_1	19.77	Si_3Ge_2	5.81		
Ge_4	8.14	Si_4H	1.16		
Si_4	5.81				
Si_3H	1.16				
Si_2GeH	1.16				
Ge				*l = 3*	**0.96**
				Si_2Ge	0.96
l = 4	**99.04**				
Si_2Ge_2	40.38				
Si_3Ge	26.92				
$SiGe_3$	21.15				
Si_4	3.85				
Ge_4	3.85				
Ge_2SiH	1.92				
Ge_3H	0.96				

Angular distribution

We calculated the partial angular distributions for a-$Si_{1-x}Ge_x$:H with x=0.1, x=0.3, and x=0.5 Ge compositions and plotted them in Fig. 4.3(a)-(f). Though

we report only three Ge compositions, the trends are similar for the other two Ge compositions x=0.2 and x=0.4. The partial pair correlation functions for α–Si–γ are plotted in the upper panel and the partial pair correlation functions for α–Ge–γ are plotted in the lower panel. In each of the cases considered, we found total angular distribution peaks centered near the tetrahedral angle with θ in the range 103°-110°. The broader angular distributions for Ge–Si–Si and Ge–Ge–Si as the Ge concentration increases represent departures from the highly tetrahedral network we began with. We also report information on partial angular distributions for H. The mean of the distribution of H–Si–Si and H–Ge–Ge is close to the tetrahedral angle 109.47° while the other two partials, H–Ge–Si and H–Si–Ge, deviate from a tetrahedral angle and range from 100.0°–116.0°.

In general, our results show broader angular distributions (far from a tetrahedral angle of 109.47) in the case of H-Ge-Si and H-Si-Ge, where atoms of three different species form an angle. This is presumably connected to the asymmetries in bonding associated with the distinct species. This feature has also been observed in the case of structures, Ge-Si-Si and Ge-Ge-Si. As shown in Fig. 4.3 we observe a broader angular distribution for the two structures as the Ge composition increases. The probability density for $\cos(\theta)$ is normal (Gaussian), which is characteristic of all WWW models (and may indeed be more general). As reported elsewhere, normally distributed cosines of bond angles lead easily to exponential (Urbach) band tails in

the electron density of states near the valence and conduction edges [91]. We return to this point in the discussion of the electronic density of states.

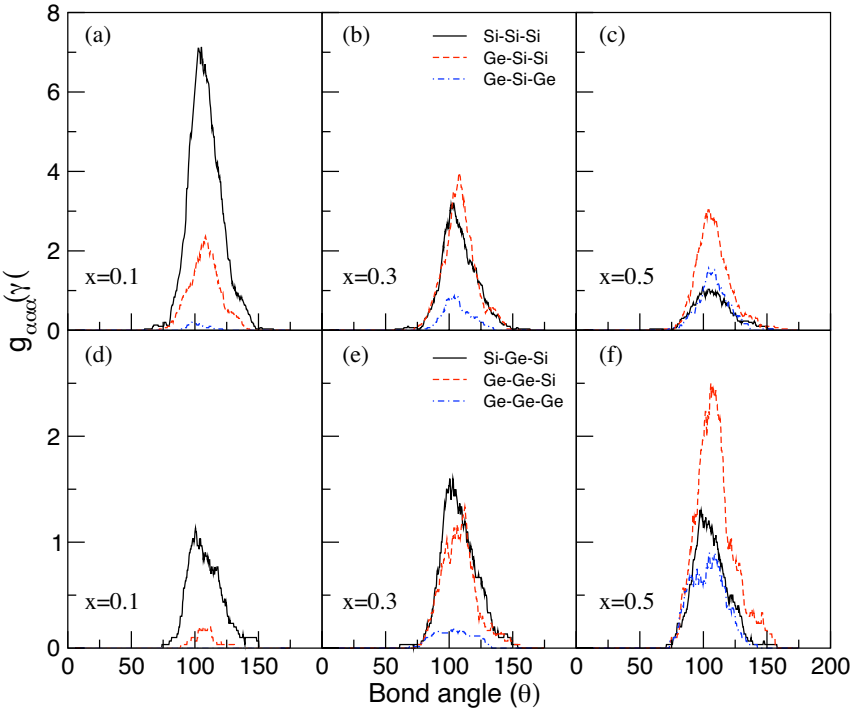

Figure 4.3: The partial bond-angle distribution function as a function of bond angle θ in a-$Si_{1-x}Ge_x$:H for x=0.1 (left panel), for x=0.3 (middle panel), and for x=0.5 (right panel). (a), (b) and (c) are partial angular distribution for three possible angles centering Si and (d), (e), and (f) are partial angles taking Ge as a center.

4.2 Electronic structure

4.2.1 Density of states

Electronic structure has been described by the electronic density of states (EDOS), which was obtained by summing suitably broadened Gaussians centered at each Kohn-Sham eigenvalue [92]. The results showed a band-gap (∼1.6 eV for

x=0.1), that becomes narrower as the Ge composition increases (∼0.8 eV for x=0.5). As usual, the reader should remember that the LDA gaps reported in this paper are significantly smaller than experiment. It is expected that trends with composition should be reproduced, however.

In this section, we present the results of one of the alloys (for a-$Si_{1-x}Ge_x$:H with x=0.4) among the five different Ge atomic compositions. The electron density of states (EDOS) shown in Fig. 4.4 shows a narrow gap. The band tails of the spectrum which we take in the region (-0.7–0.0 eV) fits exponential with $\sim e^{-E/E_o}$ with $E_o = 192$ meV as shown in the inset of Fig. 4.4. We analyze these defect states in the spectrum in detail in the next sections.

4.2.2 Localization: Inverse participation ratio

In order to understand the electron localization we used the inverse participation ratio, IPR,

$$\text{IPR} = \sum_{i=1}^{N} [q_i(E)]^2 \tag{4.2}$$

where $q_i(E)$ is the Mulliken charge residing at an atomic site i for an eigenstate with eigenvalue E that satisfies $\sum_i^N [q_i(E)] = 1$ and N is the total number of atoms in the cell. For an ideally localized state, only one atomic site contributes all the charge and so IPR=1. For a uniformly extended state, the Mulliken charge contribution per site is uniform and equals $1/N$ and so IPR=$1/N$. Thus, large IPR corresponds to localized states, small IPR to extended states.

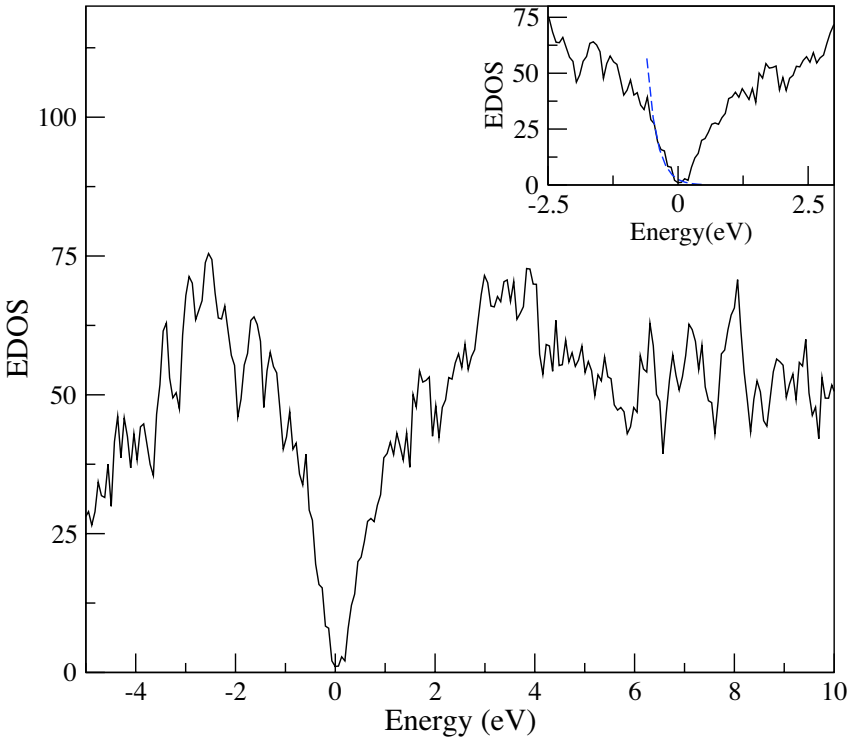

Figure 4.4: The electron density of states for a-$Si_{1-x}Ge_x$:H for x=0.4. The exponential fit in the inset for the valence band tail is $2.5\times e^{-E/E_o}$ with E_o = 192 meV for x=0.4. The Fermi level is shifted to E=0.

To investigate how the electronic properties evolve with composition in the gap, we have calculated the IPR of a-$Si_{1-x}Ge_x$:H alloy for two different Ge compositions, x=0.1 and x=0.4. We have determined the individual atomic contributions to the total IPR for localized eigenstate, to associate that state with particular structural irregularities. This provides a "spectral signature" for the various defect structure that emerge in our models. Since we are interested in states near the Fermi level, we limit our presentation here only to eigenvectors conjugate to eigenvalues which are mid-gap or near the band-tails of the spectrum. We plotted the inverse participation

ratio and the contributions of each of the atoms to the IPR for x=0.1 in Fig. 4.5 and Fig. 4.6 respectively. For the IPR, we only chose those atoms which contribute 10% or more for a particular state labeled (a–f). Those structures in the alloy which correspond to the selected mid-gap and band-tail states labeled (a–f) are shown in Fig. 4.7. As we can see from Fig. 4.5, there is one mid-gap state and about five band-tail states. We estimated the mobility band-gap in this case to be ∼1.6 eV.

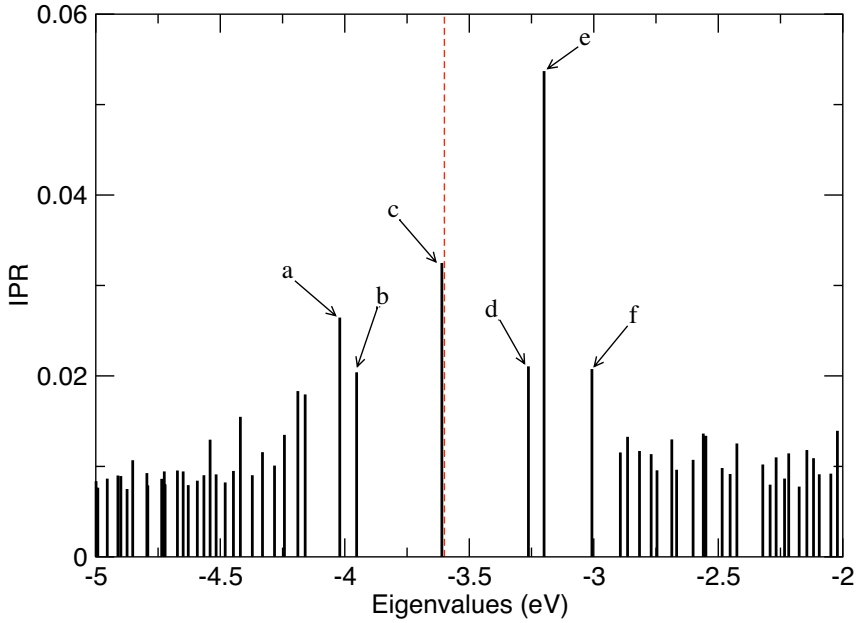

Figure 4.5: Inverse participation ratio (IPR) in the a-$Si_{1-x}Ge_x$:H alloy for x=0.1 versus energy. The dashed line is the Fermi level.

The structures which are responsible for the mid-gap state labeled c, arise from a threefold Si, a fivefold Ge, and defects. Note that the state is not entirely centered upon one obvious defect (there is resonant mixing) as predicted by the resonant cluster proliferation model [93]. We have also determined the structures

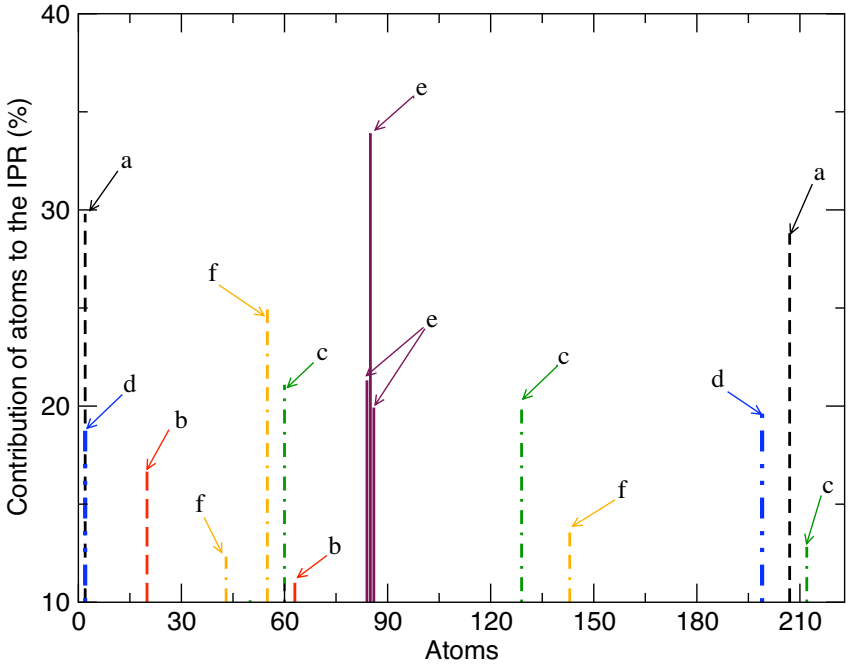

Figure 4.6: The contribution of atoms to the IPR (10% and above) of a given state in a-$Si_{1-x}Ge_x$:H alloy for x=0.1. The labels from a-f corresponds to different mid-gap and band-tail states of Fig. 4.5.

corresponding to the band-tail states ($a, d,$ and e). The large IPR derives primarily from a structure involving three fourfold Si but non-tetrahedral sites ($\delta\theta \approx 15°$). The other two mid-gap states come from a fivefold Si atom together with a strain defect (b), and a threefold Si bonded with a fivefold Si and a geometrical defect (f).

In the case of x=0.4, the inverse participation ratio as a function of eigenvalue is plotted in Fig. 4.8, while the contributions of each of the atoms to the IPR (only those atoms which contribute 5% and more) for a particular state labeled (a–f) and the different structures associated with these states are plotted in Fig. 4.9 and Fig. 4.10 respectively. As we can see from the IPR plots in the two cases, x=0.1 and

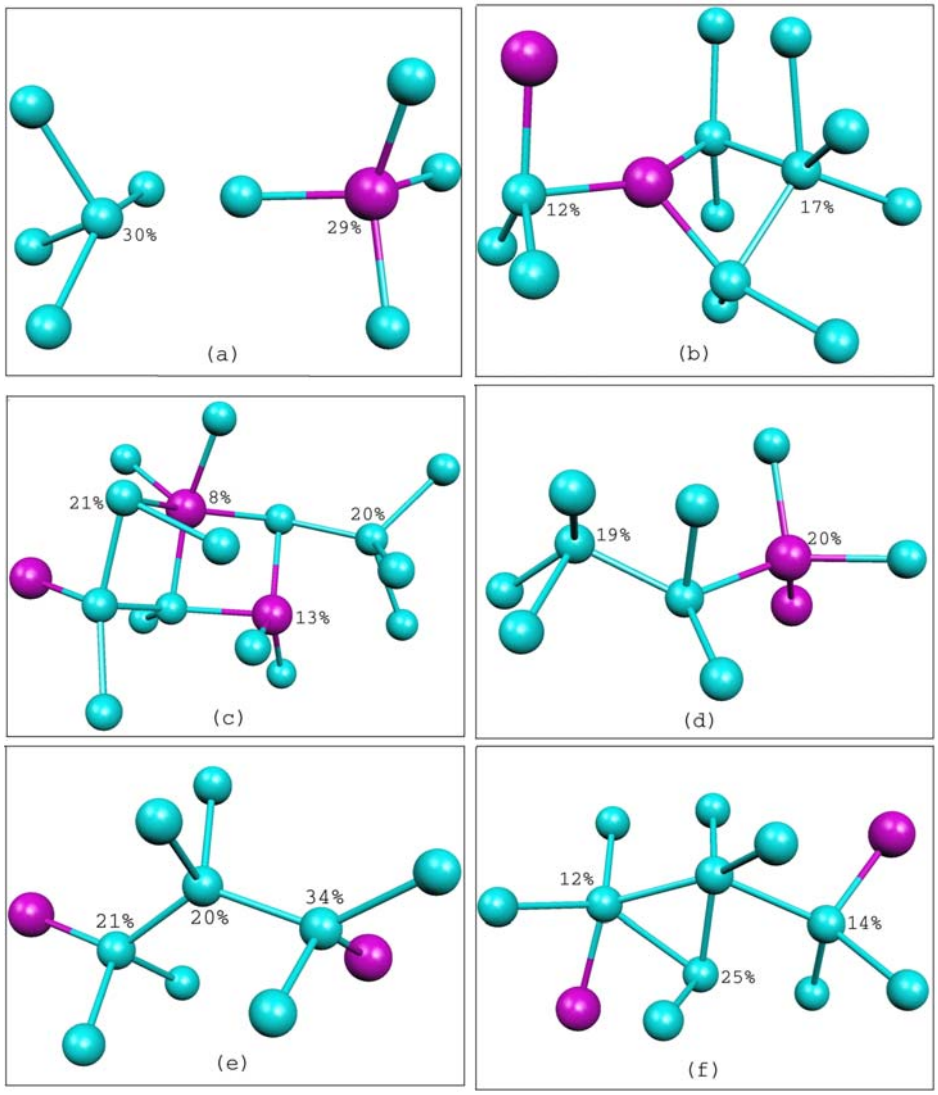

Figure 4.7: Representation of selected electronic eigenstates labeled in Fig. 4.5 from a–f in the a-$Si_{1-x}Ge_x$:H alloy for x=0.1. The color code is blue for Si and red for Ge. Numbers indicate selected site contributions to the eigenstate.

x=0.4, as the Ge content increases, we observed an increasing number of band-tail states close to the conduction band edge and hence a narrow bandgap spectrum.

By comparing the models for various x, we observe that strain defects become important in accounting for the band tail states for increasing Ge content. As shown

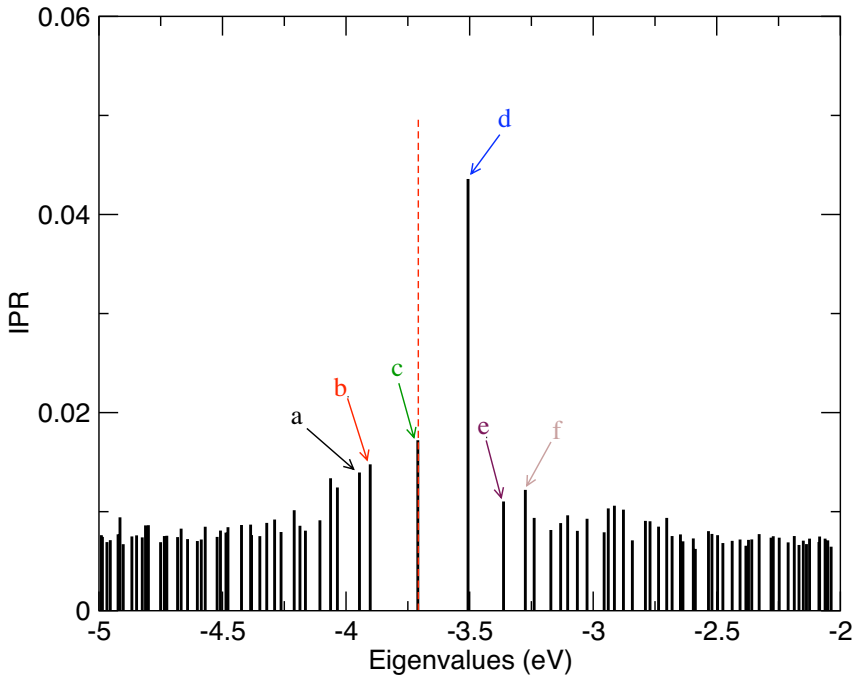

Figure 4.8: Inverse participation ratio (IPR) versus energy in a-$Si_{1-x}Ge_x$:H alloy for x=0.4. The dashed line is the Fermi level.

in Fig. 4.10, large contributions to the state labeled (a and b) come from geometrical defects, a fivefold Si, and a threefold Ge structure. States labeled d and f in this case are dominated by a geometrical defect which has three fourfold Si atoms connected to each other with strained bond with angular distribution off from a tetrahedral angle by $\pm 20^{\circ}$. The dominant contributions to the mid-gap state arise from a fivefold Si atom bonded with two strain defects.

To emphasize the effect of Ge concentration in the mobility band gap, we have estimated the mobility gap as a function of the Ge concentration x in Fig. 4.11 (f). The mobility gaps are extracted from Fig. 4.11 (a)-(e) which show the inverse participation ratio as a function of eigenvalues for different x. We observed a decrease

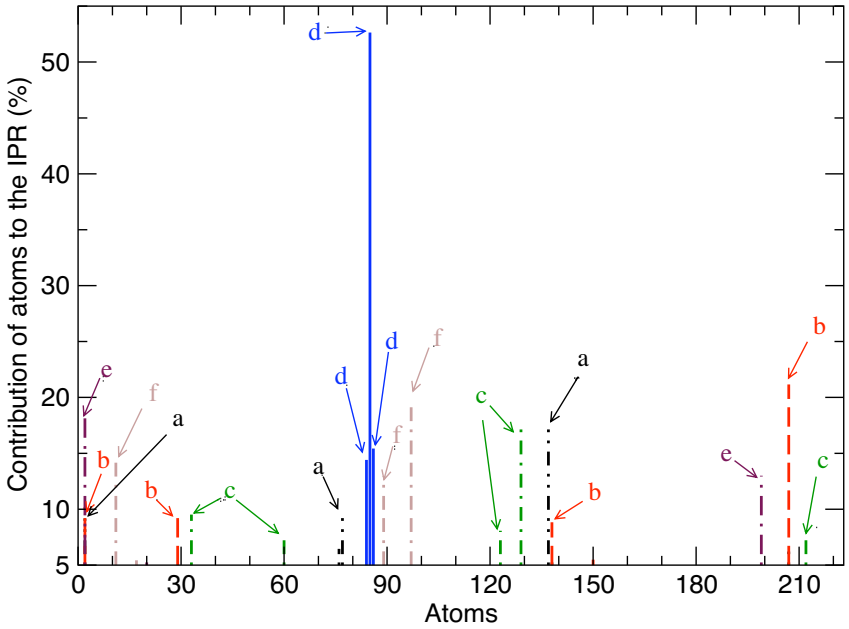

Figure 4.9: The contribution of atoms to the IPR (5% and above) of a given state in a-$Si_{1-x}Ge_x$:H alloy for x=0.4. The labels from a–f corresponds to different mid-gap and band-tail states of Fig. 4.8.

in the mobility gap as the Ge concentration increase from x=0.1 to x=0.5. The mobility gap is roughly estimated by examination of the plots of IPR versus energy. In each case, there is a fairly well-defined energy near the valence and conduction tails at which the IPR becomes roughly constant reflecting the onset of extended states. We include "error bars" to convey a rough estimate of uncertainty in our estimated gaps.

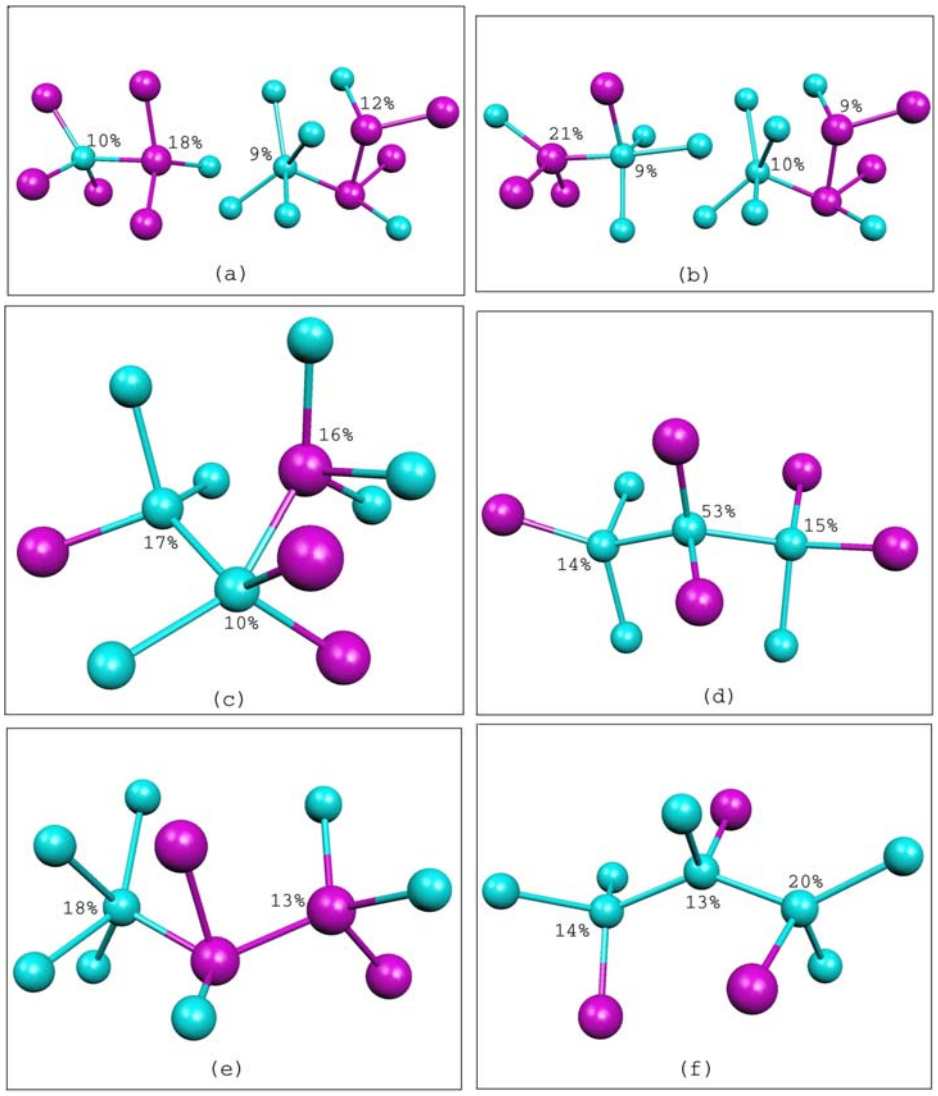

Figure 4.10: Representation of selected electronic eigenstates labeled in Fig. 4.8 from a–f in the a-$Si_{1-x}Ge_x$:H alloy for x=0.4. The color code is blue for Si and red for Ge. Numbers indicate selected site contributions to the eigenstate.

4.3 Dynamical properties

The lattice dynamics of a-$Si_{1-x}Ge_x$:H alloys are analyzed with the vibrational density of states (VDOS) and inverse participation ratio. The vibrational eigenvalues and eigenvectors are obtained by diagonalizing the dynamical matrix. The dynam-

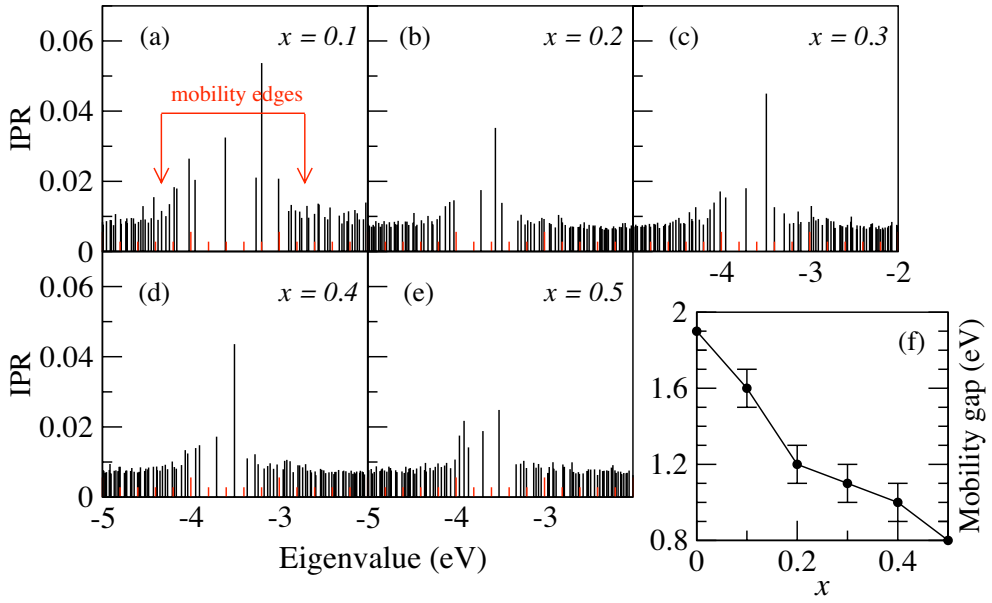

Figure 4.11: Inverse participation ratio (IPR) versus energy for different x: (a)-(e) and the estimated LDA mobility gap plotted versus the Ge concentration x: (f), in the a-$Si_{1-x}Ge_x$:H alloy. The red arrows indicate approximate mobility edges in the x=0.1 model.

ical matrix is determined by displacing each atom with 0.03 Å in three orthogonal directions and then performing first principles force calculations for all the atoms for such displacement. Each calculation yields a column of force constant matrix.

In Fig. 4.12, the phonon density of states for a-$Si_{1-x}Ge_x$:H for x=0.4 is plotted. From our simulation, the three optical mode peaks appear at 31.98 meV (Ge–Ge), 49.01 meV (Ge–Si), and 57.63 meV (Si–Si). The experimental results reported by Mackenzie *et al* [76] are 33.48 meV, 45.87 meV, and 58.27 meV for the three optical modes respectively.

The higher frequency modes in the range (213 meV-236 meV) are associated with hydrogen atoms with H–Si and H–Ge bonds which is in agreement with the

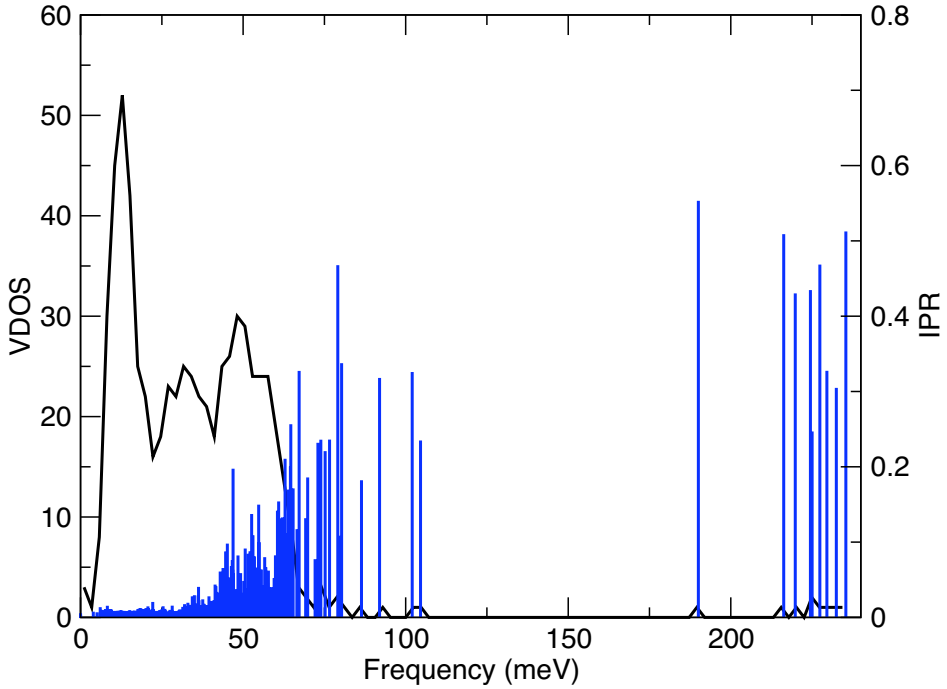

Figure 4.12: Vibrational density of states (black) and the inverse participation ratio (blue) for the a-$Si_{1-x}Ge_x$:H model for x=0.4.

experimental result (233.96 meV and 249.09 meV) reported by Wells *et al.* [94]. The principal hydrogen related features of the spectrum which exhibit higher IPR (highly localized states) are: stretch modes of Si–H at 252.81 meV, 249.58 meV, 245.49 meV, and 232.22 meV, and of Ge–H at 236.07 meV, 204.08 meV and a wagging vibration modes of Si–H and Ge–H dominate in the region of 74.39 meV-111.59 meV.

The important experiments of Aljishi and co-workers [74] provide basic information about the temperature dependence of the band tail states of these materials. In subsequent work, we will explore the band tail broadening from thermal motion [95] and analyze the validity of the model for Urbach tailing in Ref. [91]. The

temperature-dependence of the band tailing is likely to be of significant interest for applications.

In conclusion, we have presented an *ab initio* study of a-$Si_{1-x}Ge_x$:H alloys for five different Ge atomic compositions. Where the structural properties of a-$Si_{1-x}Ge_x$:H alloys are concerned, we show (a) a composition independent bond length, a modest, possibly statistically insignificant change in the total coordination, and total bond angle distribution, and (b) the emergence of geometrically strained structures and coordination defects as the Ge content increases. The electronic density of states shows an associated increase in band-tail state and gap states. This illustrates the process of "band gap engineering" with a clear illustration of how the gap closes (and with which states contributing) in the a-$Si_{1-x}Ge_x$:H alloy.

Chapter 5

Carrier transport

In the last decades researchers have been studying electronic transport in disordered systems. The possibility of doping these materials to modify their conductivity is of key technological interest. There are number of experimental studies which reported the conductivity of these materials in a wide range of temperatures which provide information about transport mechanisms. At low temperatures, much below room temperature, the idea of phonon induced hopping of electrons through localized states is considered to be the essential transport mechanism in disorder materials [96, 97].

In this chapter, we study the dynamics of localized states in the presence of thermal disorder by solving the time dependent Kohn-Sham equation with Crank-Nicholson approximation for the evolution operator and density functional Hamiltonian obtained from SIESTA [21]. We also present an investigation of electronic transport from first principles *ab initio* simulation. We have used the Kubo-Greenwood formula to compute the temperature dependent electronic conductivity of both *a-Si* and *a-Si:H* models at temperatures near room temperature. We also study the effect of doping ($n-$ type as well as $p-$type) on the conductivity. Finally we extract activation energy and pre-exponential factor of the conductivity to study the Meyer-Neldel rule [98] for the two models.

5.1 Integrating the time dependent Kohn-Sham equation

To characterize the spatial and spectral diffusion of the electronic state we track the time evolution of the electronic state by solving the time dependent Kohn-Sham equation. The spectral and spatial electronic diffusion can be obtained by tracking the time evolution of the state by solving the time dependent Kohn-Sham equation

$$i\hbar\frac{\partial}{\partial t}\psi(t) = H(t)\psi(t) \tag{5.1}$$

where H is the time dependent density functional Hamiltonian obtained from SIESTA and $\psi = \sum_i C_i\phi_i$ is the single electron wave function written in the basis of non orthogonal orbitals $\{\phi_i\}$. Löwdin transformation is used to change these basis to orthonormal basis $\{\varphi_i\}$ which is defined by $\varphi_i = \sum_j (S^{-1/2})_{ij}\phi_j$ where $S_{ij} = \int \phi_i^*\phi_j d^3r$ is the overlap matrix [99]. With these equations (5.1) becomes

$$i\hbar\frac{\partial}{\partial t}C' = H'C' \tag{5.2}$$

where $H' = S^{-1/2}HS^{-1/2}$ and $C' = S^{1/2}C$, whose solution can be obtained by using Crank-Nicholson scheme in the approximation of the evolution operator which gives a recursive relation (first order in τ) for C' between two consequative time steps t and $t+\tau$, where τ is a small time interval between two consecutive time steps.

$$C'(t+\tau) = \left(1 + i\tau H'(t)/2\hbar\right)^{-1}\left(1 - i\tau H(t)/2\hbar\right)C'(t) \tag{5.3}$$

The evolution operator approximated with Crank-Nicholson method is unitary and preserves orthonormality of the states for any τ.

The concept of participation ratio which is a quantity that tells how many sites a particular eigenstate is associated with, is commonly used to measure the localization of a state. For an ideally localized state the PR approaches unity and for extended states the PR could reach the number of atoms N. The inverse PR is defined as an inverse participation ratio IPR. Given the eigenvector $C_j(R_i)$ for state j which is defined at each site R_i, the IPR is defined as

$$(IPR)_j = (1/PR)_j = \frac{\sum_i \mid C_j(R_i) \mid^4}{(\sum_i \mid C_j(R_i) \mid^2)^2} \tag{5.4}$$

since we are able to get the time evolution of the eigenvector $C(t)$ from equation (5.3), the time evolution of spatial and spectral diffusion of the localized states can be calculated from equation (5.4).

5.2 Results

5.2.1 Spectral and spatial diffusion

The first step in the understanding of the spectral and spatial diffusion of the localized states requires a model with defects giving rise to these states. The

localization from the IPR for aSi_{64} and $aSi_{120}H_{18}$ we used at $t = 0$, is depicted in Fig. 5.1. The highly localized defect states are clearly seen at the center with higher values in their IPR. Away from the center are the extended states with lower values of IPR.

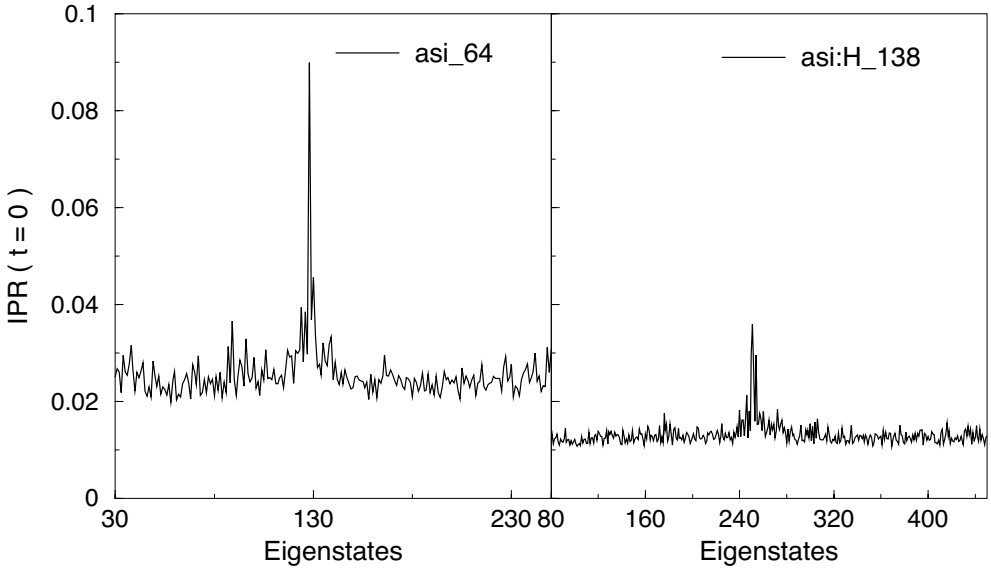

Figure 5.1: IPR for most of the states for aSi_{64} and $aSi_{120}H_{18}$ at $t = 0$. The peak in the value of IPR shows strong localization.

To study the phonon induced delocalization process in these models we chose two states near the Fermi level: the highest occupied molecular orbital (HOMO) and the lowest unoccupied molecular orbitals (LUMO). These (localized) edge states are characterized by their higher IPR values and mainly localized on very few atoms for both models at initial time $t = 0$ and diffuse to other states as time goes on. To illustrate this we calculated the contribution of every individual atoms for the IPR of each states at $t = 0$ and $t = 0.5$ps. In case of aSi_{64} at $t = 0$, the HOMO state is

localized mainly on the $38th$ and the $21st$ atoms with 23% and 15% contribution to the IPR respectively. This picture changes at a later time $t = 0.5$ps where the contribution from the $38th$ and $21st$ atom drops to 6% and 3% respectively. Similarly, for $aSi_{120}H_{18}$ at $t = 0$, the LUMO state is localized mainly on the $41st$ and $47th$ atom with 8% and 10% contribution to the IPR. However, this changes at a later time $t = 0.5$ps where the contribution from both atoms reduces to the same value 2.6%.

Understanding how electronic diffusion is influenced by temperature is not only crucial but also paves the way to get an idea of the electronic dynamics and the hopping mechanism. Having this in mind we computed the time evolution of the two localized states, HOMO and LUMO, for three different temperatures 100K, 300K and 500K for both models we used and it's been plotted in Fig. 5.2. In both models we observed that increasing temperature, with the range of temperature considered in our simulation, increases the diffusion. In the case of aSi_{64} the HOMO takes about 0.2ps and in case of $aSi_{120}H_{18}$ the LUMO takes about 0.15ps to completely diffuse to become extended states at a temperature of 300K. This diffusion is explained to be due to quantum mechanical mixing when another states gets close in energy to the state that we are tracking. We are still puzzled with the rapid diffusion of the localized state to create the extended state in a very short time. Further study needs to be done before additional work is undertaken.

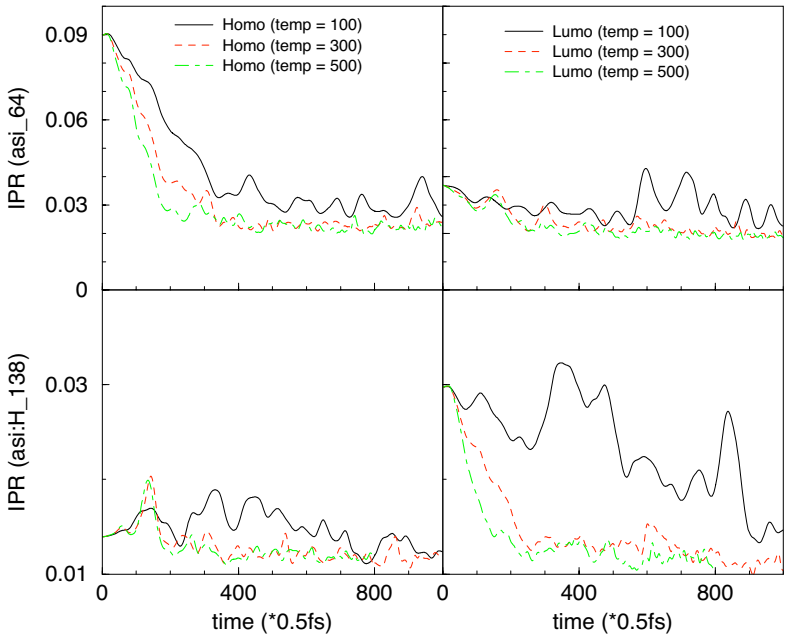

Figure 5.2: The time evolution for HOMO and LUMO of aSi_{64} and $aSi_{120}H_{18}$ at different temperatures.

5.3 The Kubo-Greenwood Formula

5.4 Methodology

From linear response theory, Kubo [100] originally derived a linear expression for electrical conductivity for an arbitrary system. Later a simplified version was developed by Greenwood [101]. An elementary derivation of the electrical conductivity can be obtained as follows [96, 102]. For the system of volume Ω, the relation between the power dissipation density P and the real part of the frequency dependent conductivity is $P = 2\sigma\Omega E_0^2$ where E_0 is the electric field. On the other hand a quantum mechanical expression of P can be obtained using Fermi's golden rule for

the transition rate (W_{nm}) from state n to state m, which eventually yield the real part of the conductivity to have a form

$$\begin{aligned}\sigma_{xx}(\omega) &= \frac{\pi e^2\hbar}{\Omega m^2}\sum_{nm}|\langle\psi_n|p_x|\psi_m\rangle|^2\frac{f_F(\varepsilon_m)-f_F(\varepsilon_n)}{\hbar\omega} \\ &\times \delta(\varepsilon_n-\varepsilon_m-\hbar\omega) \end{aligned} \tag{5.5}$$

where f_F is the Fermi distribution, e and m are the electronic charge and mass, p_x is the momentum operator, ψ_i and ε_i are the eigenstates and eigenvalues. Note that $\sigma(\omega)=\frac{1}{3}(\sigma_{xx}+\sigma_{yy}+\sigma_{zz})$.

In the dc-limit ($\omega\rightarrow 0$) the real part of the conductivity takes the form

$$\sigma(T)=\int_{-\infty}^{\infty}\frac{1}{3}(\sigma_{xx}(\varepsilon)+\sigma_{yy}(\varepsilon)+\sigma_{zz}(\varepsilon))\left(-\frac{\partial f_F(\varepsilon)}{\partial\varepsilon}\right)d\varepsilon \tag{5.6}$$

where

$$\sigma_{xx}(\varepsilon)=\frac{\pi e^2\hbar}{\Omega m^2}\sum_{nm}|\langle\psi_n|p_x|\psi_m\rangle|^2\delta(\varepsilon_n-\varepsilon)\delta(\varepsilon_m-\varepsilon) \tag{5.7}$$

For a linear system, where the dissipation is quadratic in the perturbation, we can replace the matrix element of p_x with x by using the following transformation [103]. With [x,H]=(i$\hbar$/m)p_x, we have $|\langle\psi_n|p_x|\psi_m\rangle|^2=(|\varepsilon_m-\varepsilon_n|^2m^2/\hbar^2)|\langle\psi_n|x|\psi_m\rangle|^2$, and using $|\psi_n\rangle=\sum_i a_{ni}|\varphi_i\rangle$ Eq. 5.7 can be rewritten as

$$\begin{aligned}\sigma_{xx}(\varepsilon) &= \frac{\pi e^2}{\Omega\hbar}\sum_{nm}\sum_{ij}|\varepsilon_m-\varepsilon_n|^2|\underbrace{a_{ni}^*\langle\varphi_i|x|\varphi_j\rangle a_{mj}}_{\langle\psi_n|X|\psi_m\rangle}|^2 \\ &\times \delta(\varepsilon_m-\varepsilon)\delta(\varepsilon_n-\varepsilon) \end{aligned} \tag{5.8}$$

There are number of studies which use the Kubo-Greenwood formula to compute the conductivity of amorphous materials [104, 105, 106, 108]. Most of these

studies are either at higher temperature or low temperature ranges. In this study, we use the Kubo-Greenwood formula to compute the DC conductivity for a wide range of temperatures and attempt to understand the microscopic origin of the temperature dependence. We have also studied the effect of doping on the conductivity by tracking conductivity with an artificially shifted Fermi level. In order to study the DC conductivity using Kubo-Greenwood formula [100, 101], we have used aSi_{64} and $aSi_{61}H_{10}$ models. We have prepared these models for six different temperatures 200K, 300K, 500K, 700K, 1000K, and 1500K. In each case we followed the following procedures. The two models were annealed to a particular temperature for 1.5 ps which is followed by equilibration for another 1.5 ps. Once the models are well equilibrated, we performed a constant temperature MD simulation for another 500 steps to obtain an average DC conductivity for the respected models at a given temperature.

The first principle code SIESTA [21] was used to perform the density functional calculations. We solved the self consistent Kohn-Sham equations by direct diagonalization of the Hamiltonian and a conventional mixing scheme. We used the $\Gamma(k = 0)$ point to sample the Brillouin zone in all calculations.

5.5 Results and discussions

We have studied the electrical properties at different temperature by using the inverse participation ratio (IPR) which is defined as

$$\text{IPR} = \sum_{i=1}^{N} [q_i(\varepsilon)]^2 \tag{5.9}$$

where N is the total number of atoms and $q_i(\varepsilon)$ is the Mulliken charge residing at an atomic site i for an eigenstate with eigenvalue ε with $\sum_{i=1}^{N}[q_i(\varepsilon)] = 1$. The IPR is 1 for an ideally localized state and $1/N$ for an extended state.

In Fig. 5.3 we show the IPR as a function of energy eigenvalues for six different temperatures. As the temperature increases from 200K to 1500K, the optical gap is reduced and eventually at higher temperature all the states become extended with no energy gap in the density of states.

The DC conductivity of aSi_{64} is computed for 500 instantaneous configurations for different temperatures: T=200K, 300K , 500K, 700K, 1000K, 1500K, and 1800K. At a temperature of 1800K, the system is actually a liquid with a diffusion coefficient of $D \sim 1.6 \times 10^{-4}$ cm^{2}s^{-1} and a DC conductivity of $\sim 0.3 \times 10^4$ Ω^{-1}cm^{-1} which is close to the measured value of $(1.0 - 1.3) \times 10^4$ Ω^{-1}cm^{-1} [107] and computed value of 1.75×10^4 Ω^{-1}cm^{-1} [104].

In Fig. 5.4 we have shown the DC conductivity of aSi_{64} as a function of temperature. The results from experiment for selected temperatures are also shown. As we can see from Fig. 5.3, increase in the temperature of the system enhances

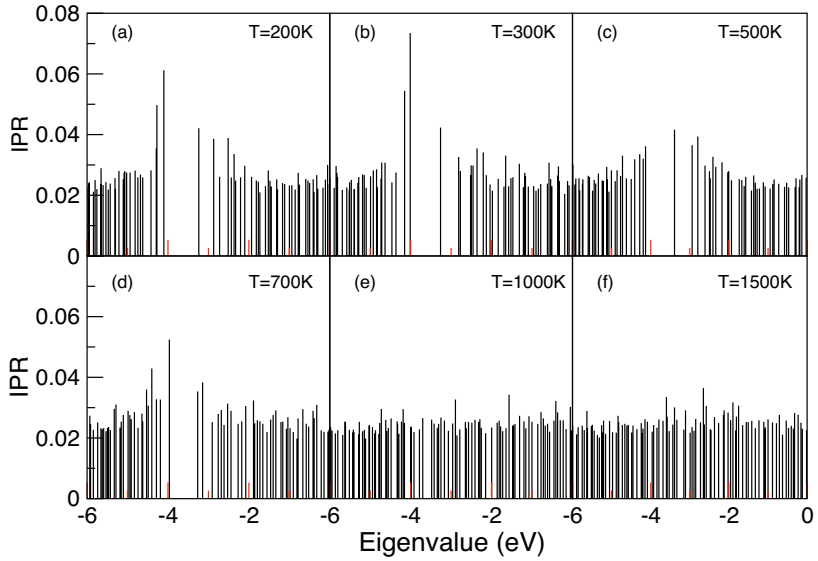

Figure 5.3: Inverse participation ratio (IPR) (indicating spatial compactness of eigenstates) versus energy for different temperatures in aSi_{64} model. LDA states and eigenvalues are used.

delocalization of the states and eventually eliminating the optical gap to change the property of the material from semi-conductor to metal. In doing so the DC conductivity changes from 0.31×10^{-10} Ω^{-1}cm^{-1} for T=200K to 0.24×10^{3} Ω^{-1}cm^{-1} for T= 1000K.

The temperature dependence of DC conductivity can be written as

$$\sigma = \sigma_o e^{(-E_a/k_B T)} \tag{5.10}$$

where E_a is the activation energy ($E_a = E_C - E_F$ or $E_a = E_F - E_V$) and σ_o is the preexponential factor of the conductivity. By dividing the dc conductivity in two regions of low temperature ($T < 450K$) and high temperature ($T > 450K$) we

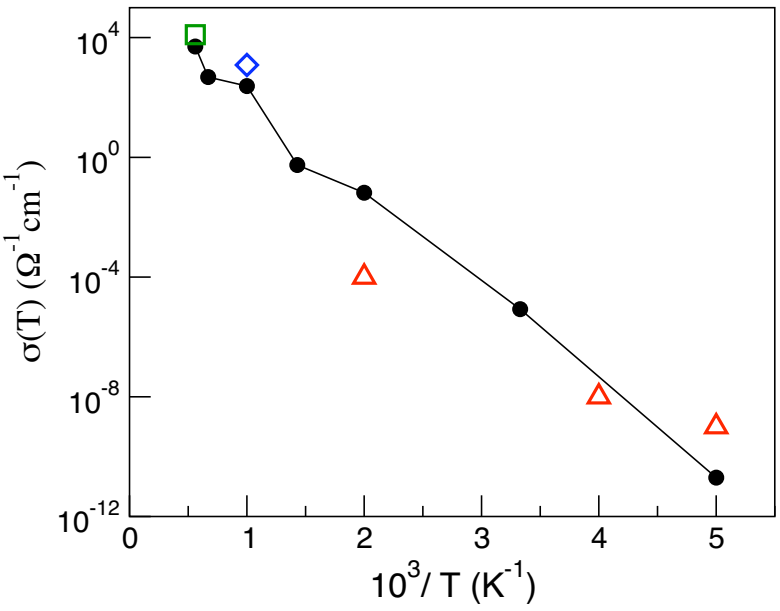

Figure 5.4: DC conductivity of aSi_{64} averaged over 500 configurations computed at different temperatures. The solid symbols are from our work, open symbols are from experiment: open square from Ref. [107], open diamond from Ref. [108] , and open triangle from Ref. [109]. The solid line is guide to the eye.

extracted the E_a and σ_o. For low T, we have obtained $E_a \sim 0.34$ eV and $\sigma_o \sim 4\ \Omega^{-1}\text{cm}^{-1}$. For high T, $E_a \sim 0.45$ eV and $\sigma_o \sim 1 \times 10^4\ \Omega^{-1}\text{cm}^{-1}$.

It is well known that doping and temperature change result in a shift in the position of Fermi level within the optical gap [110, 111]. In our simulation, we have computed the DC conductivity for a given temperature by shifting the Fermi level from its intrinsic position towards the conduction band edge as well as towards the valence band edge towards the mobility edge in steps of 0.1eV. This procedure allows us to scan the whole optical gap and compute conductivity for different doping levels

of n-type as well as p-type. The schematic representation of this process is shown in Fig. 5.5.

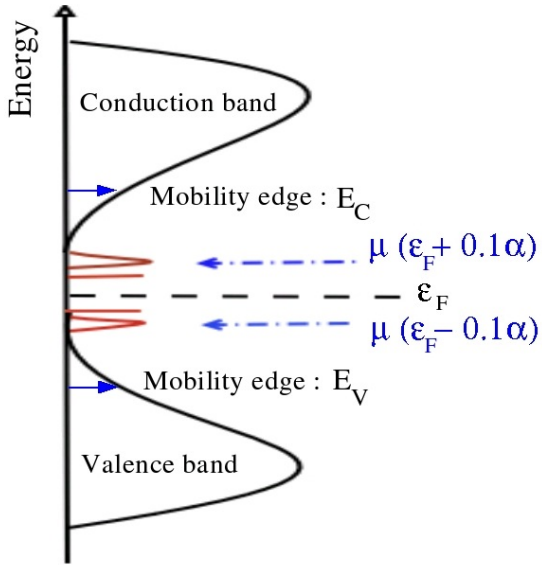

Figure 5.5: Schematic representation to show how the doping is performed in our simulation, where α is an integer. The activation energy, E_a is given by $E_a = E_C - E_F$ or $E_F - E_V$.

The computed DC conductivity for different temperatures as a function of chemical potential is shown in Fig. 5.6. As the Fermi energy shifts toward either the valence or conduction band from mid gap the DC conductivity increases. As the Fermi level gets closer to the mobility edge the conductivity becomes metallic with higher conductivity. At higher temperature, since the optical gap is almost zero, shifting the Fermi level (dopping as n-type or p-type) doesn't yield any significant change on the conductivity.

In the same way as we analyzed the aSi_{64} in the previous section, we have started our analysis of $aSi_{61}H_{10}$ by computing its electronic properties by calculating

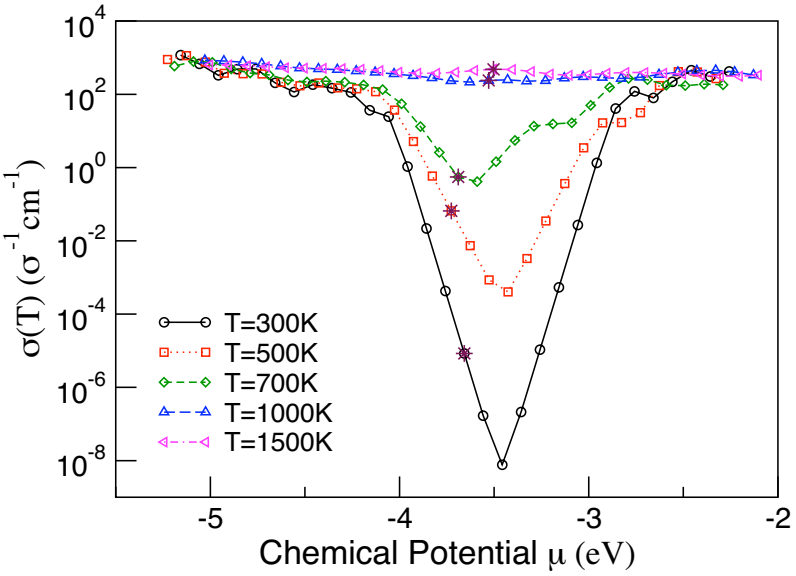

Figure 5.6: DC conductivity of aSi_{64} model averaged over 500 configurations computed at different temperatures versus chemical potential. The $*$ on each curve show the Fermi level before doping. The solid line is guide to the eye.

the inverse participation ratio. In Fig. 5.7, we have shown the IPR of $aSi_{61}H_{10}$ for different temperatures. As can be seen from the figure, the optical gap decreases with increasing the temperature which is attributed to phonon induced delocalization.

For the case of $aSi_{61}H_{10}$, increasing the temperature doesn't close the gap as fast as what we observed in the case of aSi_{64}. This might be attributed to the fact the H atoms are highly diffusive at a higher temperature and thereby introducing structural defects and hence keeps some of the states localized.

The DC conductivity of $aSi_{61}H_{10}$ as a function of temperature is shown in Fig. 5.8 with comparison from experimental results from Beyer *et al.* [112]. As we can see from Fig. 5.7, increase in the temperature of the system enhances delocalization

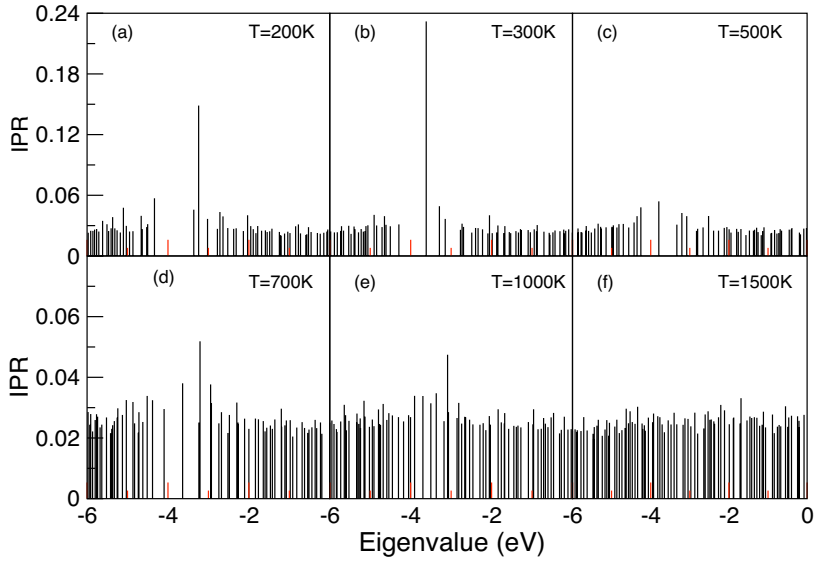

Figure 5.7: Inverse participation ratio (IPR) versus energy for different temperatures in $aSi_{61}H_{10}$. Kohn-Sham eigenvalues and states are used.

of the states and eventually eliminating the optical gap to change the property of the material from semi-conductor to metal. In this case, the DC conductivity changes from 0.54×10^{-10} Ω^{-1}cm^{-1} for T=200K to 0.83×10^{2} Ω^{-1}cm^{-1} for T= 1000K. The conductivity at T=1000K is less than of *a-Si* at the same temperature for the reason mentioned above.

For low T, we have obtained $E_a \sim 0.31$ eV and $\sigma_o \sim 5$ Ω^{-1}cm^{-1}. For high T, $E_a \sim 0.36$ eV and $\sigma_o \sim 5 \times 10^{3}$ Ω^{-1}cm^{-1}. These results are in a reasonable agreement with the experimental results of Kakalios *et al.* [113]. By using doped *a-Si:H*, Kakalios *et al.* showed that for low T, the E_a ranges from 0.16 to 0.21 eV with $\sigma_o \sim (5 - 10)$ Ω^{-1}cm^{-1}.

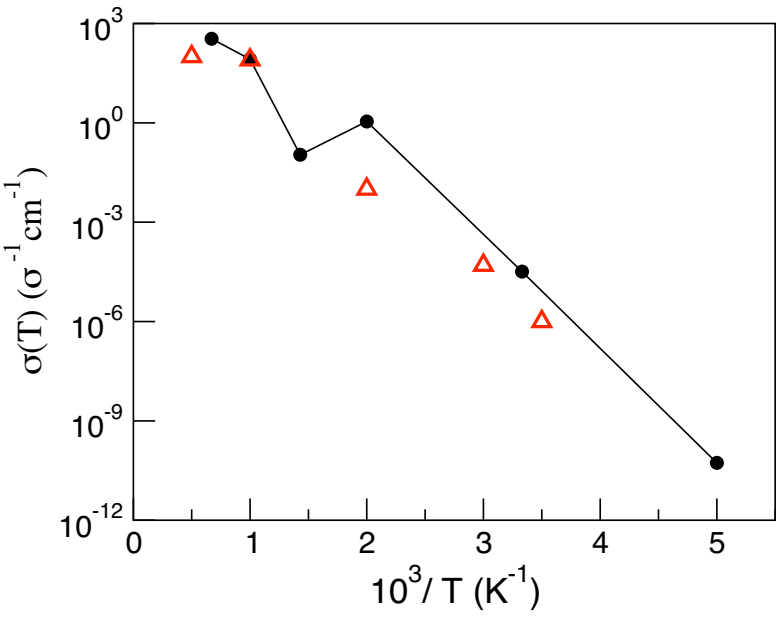

Figure 5.8: DC conductivity of $aSi_{61}H_{10}$ averaged over 500 configurations computed at different temperatures. The solid symbols are from our work, open symbols are from experiment Ref. [112]. The solid line is guide to the eye.

The computed DC conductivity for different temperatures as a function of chemical potential is shown in Fig. 5.9. As in the case of aSi_{64}, the DC conductivity increases as the Fermi energy shifts toward either the valence or conduction band from mid gap. At higher temperature, since the optical gap is almost zero, shifting the Fermi level (dopping as n-type or p-type) doesn't yield any significant change on the conductivity.

One other important feature of amorphous materials is there is a relationship between the pre-exponential factor σ_o and the activation energy E_a, called the Meyer-Neldel rule which has exponential form as

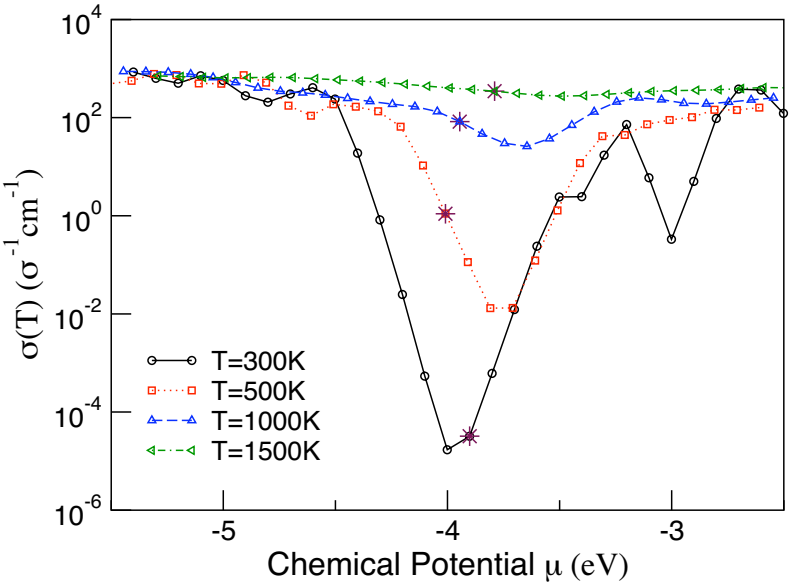

Figure 5.9: DC conductivity of $aSi_{61}H_{10}$ averaged over 500 configurations computed at different temperatures versus chemical potential. The $*$ on each curve show the Fermi level before doping. The solid line is guide to the eye.

$$\sigma_o = \sigma_{oo} e^{E_a/E_{\mathrm{MNR}}} \tag{5.11}$$

By performing a linear fit on the DC conductivity results, we identified the intercept at $(1/T) = 0$ to σ_o and the slope to the activation energy E_a. There are number of experimental results on *a-Si:H* which show this exponential behavior with E_{MNR}=0.067 eV [114, 115]. By plotting σ as a function of $1/T$ for various dopants (n-type as well as p-type) we extracted σ_o and E_a for $aSi_{61}H_{10}$ and the results are shown in Fig. 5.10. Our result show exponential behavior of σ_o as a function of the E_a, Meyer-Neldel rule, with E_{MNR}= 0.060 eV.

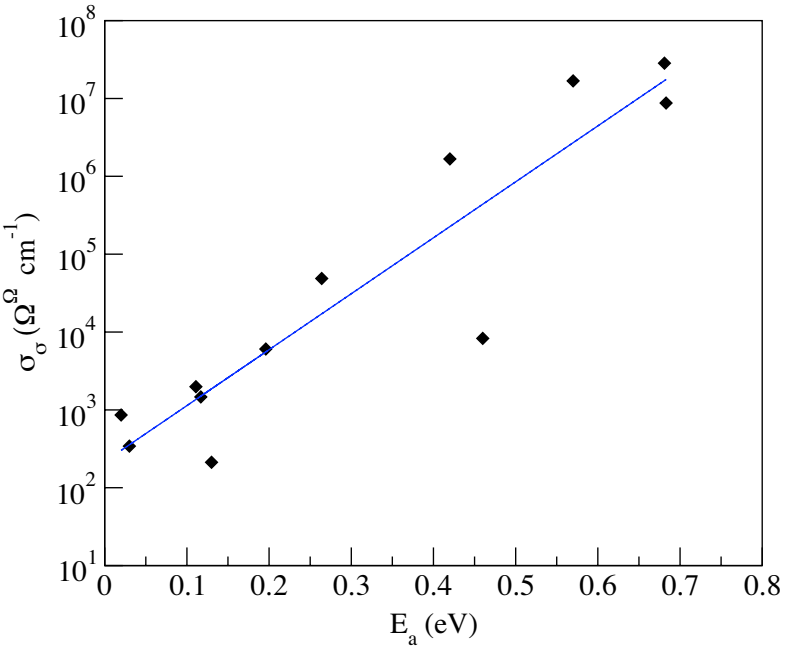

Figure 5.10: The pre-exponential factor as a function of activation energy (Meyer-Neldel rule) for $aSi_{61}H_{10}$. The dashed line is an exponential fit which represent Eq. (5.11).

The other fundamental characteristic of aSi:H is its high temperature coefficient of resistance, which makes it a candidate for uncooled microbolometer applications. The temperature coefficient of resistance (TCR) is defined as

$$TCR = \frac{1}{\rho_o}\frac{\rho - \rho_o}{T - T_o} \tag{5.12}$$

where ρ is a resistivity at any given temperature T and ρ_o is a resistivity at a reference temperature T_o (usually room temperature). The computed result of TCR with a definition of Eq. 5.12 using $T_o = 300K$ for $aSi_{61}H_{10}$ is shown in Fig. 5.11. The experimental result of TCR near room temperature in *a-Si:H* is $-2.7\%K^{-1}$ [116]. Our result show a TCR value of $\sim -2.0\%K^{-1}$ at $T = 350K$ which is in a good agreement with the experiment. Close to T_o the value of TCR is very sensitive to

temperature and has a wide range of values $-(2.0-5.0)\%K^{-1}$. The fundamental question of why these materials show such a high TCR will be the focus of future study.

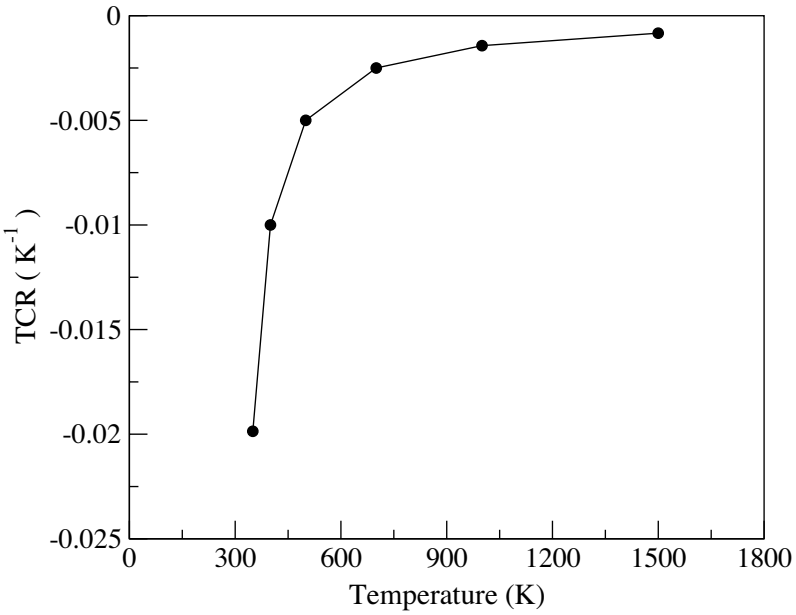

Figure 5.11: The temperature coefficient of resistance (TCR) for $aSi_{61}H_{10}$ as a function of temperature.

In conclusion, we have presented a study of transport in amorphous materials. We used Kubo-Greenwood formula for computing the DC conductivity of aSi_{64} and $aSi_{61}H_{10}$ for different temperatures. We have also presented the effect of doping on the DC conductivity. As the E_f level gets close to either the conduction edge or valence edge we observe an increase in the DC conductivity. Once the E_f exceeds the "mobility edge" we observe a weak temperature dependence on the DC conductivity. Though it requires further investigation (by using various dopants in aSi_{64} and

$aSi_{61}H_{10}$), we observe the Meyer Neldel rule with exponential behavior for the pre-exponential factor σ_o. The computed result for TCR is in a very good agreement with the experiment. Further study of this method involves using a richer basis set and full k-point sampling in the Brillouin zone. Further, the statistical aspects (convergence of the conductivity with respect to length of MD simulation and temperature) will be explored.

Chapter 6

Conclusion

In this work, a study of light induced effect using a simple implementation of light excitation, a study of atomic diffusion mechanisms, and a study of carrier transport by computing the DC conductivity of amorphous semiconductors are presented.

Using a direct *ab-initio* calculation of network dynamics and diffusion both for the electronic ground state and light-excited state for a-Si:H this work able to address the light induced effect. Consistent with recent NMR experiments, in the light-excited state, there is an enhanced hydrogen diffusion and formation of new silicon dihydride configurations. For the first time, this work shows the detailed dynamic pathways that arise from light-induced occupation changes, and provides one explicit example of defect creation and paired H formation. The enhanced structural change observed in the simulated light excited state is attributed to the local heating where the strong electron phonon coupling of a localized state locally increases the kinetic energy of atoms near the vicinity of the site where the state is localized. In addition, by extending the study to understand the diffusion mechanism of hydrogen in a-Si:H, it is observed that H emission is stimulated by Si motion, and the FBCD mechanism is shown to be important both for stripping off H chemically bonded to Si (thus creating "free" atomic H), and of course for creating Si dangling bonds.

An *ab initio* study of a-$Si_{1-x}Ge_x$:H alloys for five different Ge atomic compositions is also presented. Where (a) a composition independent bond length, a modest, possibly statistically insignificant change in the total coordination, and total bond angle distribution, and (b) the emergence of geometrically strained structures and coordination defects as the Ge content increases. The electronic density of states shows an associated increase in band-tail state and gap states. This illustrates the process of "band gap engineering" with a clear illustration of how the gap closes (and with which states contributing) in the a-$Si_{1-x}Ge_x$:H alloy.

A simulation of the dynamics of the localized states in the presence of thermal disorder by integrating the time dependent Kohn-Sham equation and density functional Hamiltonian is presented. A rapid diffusion of the localized state to the extended state in a very short time step is observed. This diffusion is explained to be due to quantum mechanical mixing when another states gets close in energy to the state that is being tracked.

In the study of transport in amorphous materials, Kubo-Greenwood formula is used for computing the DC conductivity of aSi_{64} and $aSi_{61}H_{10}$ for different temperatures. The results from this method are in good agreement with the experiment. The effect of doping on the DC conductivity for both materials is also presented. As the E_f level gets close to either the conduction edge or valence edge an increase in the DC conductivity is observed. Once E_f exceeds the "mobility edge" a weak temperature dependence on the DC conductivity is observed.

Bibliography

[1] D. L. Staebler and C. R. Wronski, Appl. Phys. Lett. **31**, 292 (1977).

[2] R. A. Street, *Hydrogenated amorphous silicon* (Cambridge University Press, Cambridge, 1991).

[3] H. Fritzsche, *Light-Induced Structural Changes in Glass, in Insulating and Semiconducting Glasses* p653, (World Scientific, Singapore, 2000).

[4] J. Singh and K. Shimakawa, *Advances in Amorphous Semiconductors* Ch. 10 (Taylor and Francis, London, 2003).

[5] H. M. Branz, Sol. St. Comm. **105/6**, 7725 (1999); Phys. Rev. B **74**, 085201 (2006); Phys. Rev. B **59**, 5498 (1999).

[6] H. M. Cheong, S. H. Lee, B. P. Nelson, and A. Mascarenhas, App. Phys. Lett. **77**, 2686 (2000).

[7] T. Su, P. C. Taylor, G. Ganguly, and D. E. Carlson, Phys. Rev. Lett. **89**, 015502 (2002).

[8] K. C. Palinginis, J. D. Cohen, S. Guha, and J. C. Yang, Phys. Rev. B **63**, 201203 (2001).

[9] M. Stutzmann, R. A. Street, C. C. Tsai, J. B. Boyce, and S. E. Ready, J. Appl. Phys. **66**, 569 (1989).

[10] C. Catlow (ed.), Defects and Disorder in Crystalline and Amorphous Solids, Series C: Mathematical and Physical Sciences-Vol. 418 (1994).

[11] R. Atta-Fynn, P. Biswas, and D. A. Drabold, Phys. Rev. B **69**, 245204 (2004).

[12] J. Li and D. A. Drabold, Phys. Status Solidi B **233** 10 (2002).

[13] J. Li and D. A. Drabold, Phys. Rev. B **68** 033103 (2003).

[14] G. T. Barkema and N. Mousseau, Phys. Rev. B **62**, 4985 (2000).

[15] F. Wooten, K. Winer, and D. Weaire, Phys. Rev. Lett. **54**, 1392 (1985).

[16] T. A. Abtew, D. A. Drabold, and P. C. Taylor, Appl. Phys. Lett. **86**, 241916 (2005).

[17] This second conformation reveals only that the proton-proton distances reported are "robust" even for a rather different chemical environment. It is unlikely that the SiH_2 would be so close to a dangling bond. See S. Yamasaki, H. Okushi, A. Matsuda, K. Tanaka, and J. Isoya, Phys. Rev. Lett. **65**, 756 (1990).

[18] P. A. Fedders unpublished.

[19] P. A. Fedders and D. A. Drabold, Phys. Rev. B **47**, 13277 (1993).

[20] R. M. Martin, Electronic structure: Basic theory and practical method, Cambridge university press, (2004).

[21] P. Ordejón, E. Artacho, and J. M. Soler, Phys. Rev. B **53**, 10441 (1996); D. Sánchez-Portal, P. Ordejón, E. Artacho, and J. M. Soler, Int. J. Quantum Chem. **65**, 453 (1997); J. M. Soler, E. Artacho, J. D. Gale, A. García, J. Junquera, P. Ordejón, and D. Sánchez-Portal, J. Phys.: Condens. Matter **14**, 2745 (2002).

[22] P. Ordejón, E. Artacho, and J. M. Soler, Phys. Rev. B **53**, 10441 (1996).

[23] D. Sánchez-Portal, P. Ordejón, E. Artacho, and J. M. Soler, Int. J. Quantum Chem. **65**, 453 (1997).

[24] J. M. Soler, E. Artacho, J. D. Gale, A. García, J. Junquera, P. Ordejón, and D. Sánchez-Portal, J. Phys.: Condens. Matter **14**, 2745 (2002).

[25] J. P. Perdew and A. Zunger, Phys. Rev. B **23**, 5048 (1981).

[26] J. P. Perdew, K. Burke, and M. Ernzerhof, Phys. Rev. Lett. **77**, 3865 (1996).

[27] N. Troullier and J. L. Martins, Phys. Rev. B **43**, 1993 (1991).

[28] L. Kleinman and D. M. Bylander, Phys. Rev. Lett. **48**, 1425 (1982).

[29] E. Artacho, D. Sánchez-Portal, P. Ordejón, A. García and J. M. Soler, Phys. Status Solidi B **215**, 809 (1999).

[30] M. Stutzmann, W. B. Jackson, and C. C. Tsai, Phys Rev B **32**, 23 (1985).

[31] R. Biswas, I. Kwon, and C. M. Soukoulis, Phys. Rev. B **44**, 3403 (1991).

[32] S. Zafar and E. A. Schiff, Phys. Rev. B **40**, 5235 (1989).

[33] S. Zafar and E. A. Schiff, Phys. Rev. Lett. **66**, 1493 (1991).

[34] R. Biswas and Y. -P. Li, Phys. Rev. Lett. **82**, 2512 (1999).

[35] N. Kopidakis and E. A. Schiff, J. Non. Cryst. Solids **266-269**, 415 (2000).

[36] S. B. Zhang and H. Branz, Phys. Rev. Lett. **87**, 105503 (2001).

[37] H. Fritzsche, Annu. Rev. Mater. Res. **31**, 47-79 (2001).

[38] T. A. Abtew and D. A. Drabold, J. Phys.: Condens. Matt. **18**, L1 (2006).

[39] T. A. Abtew and D. A. Drabold, Phys. Rev. B **74**, 085201 (2006).

[40] X. Zhang and D. A. Drabold, Phys. Rev. Lett. **83**, 5042 (1999).

[41] P. V. Santos and W. B. Jackson, Phys. Rev. B **46**, 4595 (1992).

[42] MOLEKEL 4.0, P. Flükiger, H.P. Lüthi, S. Portmann, and J. Weber, Swiss Center for Scientific Computing, Manno (Switzerland) (2000).

[43] A. Szabo and N. S. Ostlund, *Modern Quantum Chemistry*, (McGraw-Hill, New York, 1989), p. 151.

[44] M. H. Brodsky, Manuel Cardona, and J. J. Cuomo, Phys. Rev. B **16**, 3556 (1977).

[45] G. Lucovsky, R. J. Nemanich, and J. C. Knights, Phys. Rev. B **19**, 2064 (1979).

[46] W. P. Pollard and G. Lucovsky, Phys. Rev. B **26**, 3172 (1982).

[47] C. G. Van de Walle, Phys. Rev. B **49**, 4579 (1994).

[48] D. A. Drabold, P. A. Fedders, O. F. Sankey, and J. D. Dow, Phys. Rev. B **42**, 5135(1990).

[49] P. A. Fedders *et al.* Phys. Rev. Lett. **68**, 1888 (1992).

[50] W. B. Jackson and J. Kakalios , Phys. Rev. B **37**, 1020 (1988).

[51] H. M. Branz, Phys. Rev. B **59**, 5498 (1999).

[52] T. A. Abtew and D. A. Drabold, Phys. Rev. B **74**, 085201 (2006).

[53] P. V. Santos and W. B. Jackson, Phys. Rev. B **46**, 4595 (1992).

[54] C. V. Van de Walle and R. A. Street, Phys. Rev. B **51**, 10615 (1995).

[55] S. Lanzavecchia and L. Colombo, Europhys. Lett. **36**, 295 (1996).

[56] R. Biswas *et al.* Phys. Rev. B **57**, 2253 (1998)

[57] A. J. Franz *et al.* Phys. Rev. B **57**, 3927 (1998).

[58] B. Tuttle *et al.* Phys. Rev. B **59**, 5493 (1999).

[59] P. A. Fedders, Phys. Rev. B **61**, 15797 (2000).

[60] Y. S. Su and S. T. Pantelides, Phys. Rev. Lett. **88**, 165503 (2002).

[61] G. Panzarini and L. Colombo, Phys. Rev. Lett. **73**, 1636 (1994).

[62] S. Bedard and L. J. Lewis, Phys. Rev. B **61**, 9895 (2000).

[63] F. Buda, L. Chiarotti, R. Car, and M. Parrinello, Phys. Rev. Lett. **63**, 294 (1989).

[64] G. T. Barkema and N. Mousseau, Phys. Rev. Lett. **81**, 1865 (1998).

[65] E. P. Donovan, F. Spaepen, D. Turnbull, J. M. Poate, and D. C. Jacobson, Appl. Phys. Lett. **42**, 698 (1983).

[66] D. A. Drabold *et al.*, Phys. Rev. Lett. **67**, 2179 (1991); T. A. Abtew and D. A. Drabold in *Theory of Defects in semiconductors*, D. A. Drabold and S. K. Estricher (Eds), Springer, Berlin (2006) p245.

[67] P. A. Fedders *et al.* Phys. Rev. Lett. **85**, 401 (2000).

[68] T. Su *et al.*, Phys. Rev. B **62**, 12849 (2000).

[69] For example, A. Ahmed and R. N. Tait, Infrared Physics and Technology **46** 468 (2005).

[70] M. Garcia, R. Ambrosio, A. Torres, and A. Kosarev, J. Non. Cryst. Solids 338-340 744 (2004).

[71] P. Agrawal, H.Povolny, S. Han, and X. Deng, J. Non. Cryst. Solids 299-302 1213 (2002).

[72] M. Shima, M. Isomura, K. I. Wakisaka, K. Murata and M. Tanaka, Sol. Energy Materials and Solar Cells **85**, 167 (2005).

[73] V. I. Kuznetsov, M. Zeman, L. L. A. Vosteen, B. S. Girwar, and J. W. Metselaar, J. Appl. Phys. **80**, 6496 (1996).

[74] S. Aljishi, J. D. Cohen, S. Jin and L. Ley, Phys. Rev. Lett. **64**, 2811 (1990).

[75] K. D. Mackenzie, J. R. Eggert, D. J. Leopold, Y. M. Li, S. Lin, and W. Paul, Phys. Rev. B **31**, 2198 (1985).

[76] K. D. Mackenzie, J. H. Burnett, J. R. Eggert, Y. M. Li, and W. Paul, Phys. Rev. B **38**, 6120 (1988).

[77] Y. Nishino, S. Muramatsu, Y. Takano, and H. Kajiyama, Phys. Rev. B **38**, 1942 (1988).

[78] L. Incoccia, S. Mobilio, M. G. Proietti, P. Fiorini, C. Giovannella, and F. Evangelisti, Phys. Rev. B **31**, 1028 (1985).

[79] N. Mousseau and M. F. Thorpe, Phys. Rev. B **48**, 5172 (1992).

[80] M. R. Weidmann and K. E. Newman, Phys. Rev. B **45**, 8388 (1992).

[81] D. B. Aldrich, R. J. Nemanich, and D. E. Sayers, Phys. Rev. B **50**, 15026 (1994).

[82] M. Yu, C. S. Jayanthi, D. A. Drabold, S. Y. Yu, Phys. Rev. B **64**, 165205 (2001).

[83] P. A. Fedders and A. E. Carlsson, Phys. Rev. B **37**, 8506 (1988).

[84] D. A. Drabold, P. A. Fedders, O. F. Sankey, and J. D. Dow, Phys. Rev. B **42**, 5135 (1990); P. A. Fedders and D. A. Drabold, Phys Rev B **47** 13277 (1993); M. Durandurdu, D. A. Drabold, and N. Mousseau, Phys. Rev. B **62**, 16307 (2000).

[85] P. C. Kelires and J. Tersoff, Phys. Rev. Lett. **61**, 562 (1988).

[86] I. Štich, R. Car, and M. Parrinello, Phys. Rev. B **44**, 11092 (1991).

[87] G. T. Barkema, N. Mousseau, R. Vink, and P. Biswas, Proceedings of the Materials Research Society, **661**, A28.1 (2001).

[88] M. Ishimaru, M. Yamaguchi and Y. Hirotsu, Phys. Rev. B **68**, 235207 (2003).

[89] R. Atta-Fynn, P. Biswas, P. Ordejon and D. A. Drabold, Phys. Rev. B **69**, 085207 (2004).

[90] Y. Nishino and Y. Takano, J. Appl. Phys. **25**, 885 (1986).

[91] J. Dong and D. A. Drabold, Phys. Rev. B **54**, 10284 (1996).

[92] P. Biswas, D. Tafen and D. A. Drabold, Phys Rev B **71**, 054204 (2005).

[93] Jianjun Dong and D. A. Drabold, Phys. Rev. Lett. **80** 1928 (1998); J. J. Ludlam, S. N. Taraskin, S. R. Elliott and D A Drabold, J. Phys.: Condens. Matter **17**, L321 (2005).

[94] J. Wells, E. van Hattum, R. Schropp, P. Phillips, D. Carder, F. Habraken, and J. Dijkhuis, Phys. Stat. Sol. (b) **241**, 3474 (2004).

[95] D. A. Drabold, P. A. Fedders, S. Klemm, O. F. Sankey, Phys. Rev. Lett. **67**, 2179 (1991).

[96] H. Overhof and P. Thomas *Electronic Transport in Hydrogenated Amorphous Silicon* Springer Tracts in Modern Physics No. 114 (Springer, Berlin, 1989) .

[97] D. A. Drabold and L. Jun *Amorphous and Hetrerogeneous Silicon Based Films*, MRS Symposia Proceedings No. 715 (Materials Research Society, Warrendale, PA), p A14.1 (2003).

[98] W. Meyer and H. Neldel, Z. Techn. Phys. **12**, 588 (1937).

[99] J. K. Tomfohr and O. F. Sankey, Phys. Stat. Solidi **226**, 115 (2001).

[100] K. Kubo, J. Phys. Soc. Jpn. **12**, 576 (1957).

[101] D. A. Greenwood, Proc. Phys. Soc. **71**, 585 (1958).

[102] J. H. Davis, *The physics of low dimensional semiconductors* Cambridge University Press (Cambridge, United Kingdom, 1998).

[103] L. Moseley and T. Lukes, Am. J. Phys. **46** 676 (1978).

[104] I. Stiich, R. Car, and M. Parrinello, Phys. Rev. B **44**, 4262 (1991).

[105] J. M. Holender and G. J. Morgan, J. Phys.: Condens. Matter **4**, 4473 (1992).

[106] J. Dong and D. A. Drabold, Phys. Rev. Lett. **80**, 1928 (1998).

[107] V. M. Glasov, S. N. Chizhevskaya, and N. N. Glagoleva, *Liquid Semiconductors* (Plenum, New York, 1969).

[108] S. S. Ashwin, U. V. Waghmare, and S. Sastry, Phys. Rev. Lett. **92**, 175701 (2004).

[109] A. Lewis, Phys. Rev. Lett. **29**, 1555 (1972).

[110] R. H. Williams, R. R. Varma, W. E. Spear, and P.G. LeComber, J. Phys. C **12**, L209 (1979).

[111] B. von Roedern, L. Ley, and M. Cardona, Solid State Commun. **29**, 415 (1979).

[112] W. Beyer, A. Medeisis, and H. Mell, Commun. Phys. **2**, 121 (1977).

[113] J. Kakalios and R. A. Street, Phys. Rev. B **34**, 6014 (1986).

[114] D. E. Carlson and C. R. Wronski, in *Amorphous Semiconductors*, ed. by M. H. Brodski, Topics Appl. Phys., Vol. 36 (Springer, Berlin) Chap 10.

[115] H. Fritzsche, Sol. Energy Mat. bf 3, 447 (1980).

[116] M. B. Dutt and V. Mittal, J. Appl. Phys. **97**, 083704 (2005).

Appendix A

In this section we present codes that we developed and used in SIESTA code for solving time dependent Kohn-Sham equation and for computing the DC conductivity using the Kubo-Greenwood formula. *NOTE: Test the codes before doing any important calculations. The user should be aware of parameters which change with the number of atoms and basis set and change them accordingly.*

A.1 Codes

A.1.1 Time Dependent Kohn-Sham

```
c
c     Subroutine to solve the time dependent Kohn-Sham
c     equation using a Crank-Nicolson scheme
c
c         T. A. Abtew and D. A. Drabold
c
c
      subroutine timeevol(no,Haux,Saux,rpsi,ipsi,dt,istep1)
c
c
       implicit none
c
c
       integer no,istep1,dimen,invidet
       integer mdsteps
c
       parameter(dimen = 254, mdsteps = 2000)
       parameter(invidet = 01)
c
       real*8 Haux(dimen,dimen), Saux(dimen,dimen)
       real*8 dt, sumnormal
       real*8 HS(dimen,dimen)
       real*8 HSL(dimen,dimen), Sauxinvsqr(dimen,dimen)
       real*8 rpsi(dimen,dimen), ipsi(dimen,dimen)
       complex*16 cpsi(dimen,dimen), newh(dimen,dimen)
```

```
      complex*16 cpsic(dimen,dimen), newh2(dimen,dimen)
      complex*16 cpsio(dimen,dimen), cpsin(dimen,dimen)
c
      save cpsi,cpsic,cpsio
c
c     ------------------------------------
c
      integer nsiatom, orbSi
      integer nhatom, orbH, nat
c
      parameter(nsiatom = 61, orbSi = 4)
      parameter(nhatom = 10, orbH = 1)
c
c
      real*8 h(dimen,dimen), ss(dimen,dimen)
      real*8 sso(dimen,dimen), sssqrt(dimen,dimen)
      real*8 qsite(300,dimen)
      real*8 qsiteav(300,dimen),qsiteavp(300,dimen)
      complex*16 qq(dimen, dimen),qqp(dimen, dimen)
c
c
      complex*16 qq1(dimen, dimen),qq2(dimen, dimen)
      complex*16 qq3(dimen, dimen),qq4(dimen, dimen)
      real*8 qsite1(300,dimen), qsite2(300,dimen)
      real*8 qsite3(300,dimen), qsite4(300,dimen)
c
      integer ii, jj, kk, ll, mu, nu, nm, ipp,kk1
      real*8 sumc, sumch,sumcp
      complex*16 sum,sump
c
      integer unit, unit1, unit2, unit3, unit4
      complex*16 sum1, sum2, sum3, sum4
      real*8 sumc1, sumch1, spect1
      real*8 sumc2, sumch2, spect2
      real*8 sumc3, sumch3, spect3
      real*8 sumc4, sumch4, spect4
c
      integer homom5, homom3, homom2, homom1, homo
      integer lumo, lumop1, lumop2, lumop5
c
      logical
     .  frstmd
c
c
```

```
      save frstmd
      data frstmd /.true./
c
c
      integer lda,ldwork,mm,nn,natom
      parameter(mm = 254, nn = 254, natom = 71)
      parameter(lda = mm)
      parameter(ldwork = nn)
c
      complex*16 A(lda,nn),workd(ldwork)
      real*8 rcond
      complex*16 det(4)
      integer info,ipivot(nn)
c
      external zgefa,zgedi
      external dgetrf,dgetri
      external dgemm

      integer i,j,k,t,job,orb_sin,r,l,m,s
c
      integer io1,iu1,ie1,ia1
      integer ib1,ic1,id1,ig1
      real*8 eye(dimen,dimen)
      complex*16 iImag, DD(dimen,dimen)
      complex*16 B(dimen,dimen), D(dimen,dimen)
      complex*16 F(dimen,dimen)
c

      complex*16 DDD(dimen,dimen)
      complex*16 aa(dimen), bb(dimen)
      complex*16 aac(dimen), bbc(dimen)
      complex*16 c(dimen), g(dimen), q(dimen)
      complex*16 cc(dimen),fc(dimen),gc(dimen), qc(dimen)
c
     real*8 ccc
c
     real rhoc(natom)
     real rhocpercent(natom,dimen)
     save rhocpercent
c
     real rho_av(natom,dimen)
     real*8 ipr_av(dimen)
c
     complex*16 cii(dimen)
```

```
      complex*16 ci(dimen),fi(dimen),gi(dimen),qi(dimen)
      complex*16 ri(dimen)
      save ci,fi,gi,qi,ri
c
      real sumipr11, sumipr11nn
      real sumiprd11
c
      real sumipr11n(dimen),sumipr11np(dimen)
      save sumipr11n,sumipr11np
c
      complex*16 sumipr1, sumipr2, sumipr3, sumipr4
      complex*16 sumipr5, sumipr6
      complex*16 sumipr1c, sumipr2c, sumipr3c, sumipr4c
      complex*16 sumipr5c, sumipr6c
      real rho1,rho2,rho3,rho4,rho5,rho6
      real*8 alpha,beta
c
      real*8 normal
      real*8 tau, h_bar
      character*1 jobz,uplo
      h_bar = 0.65822d0
      nat = nsiatom * orbSi + nhatom * orbH
c
c
c      if (istep1 .eq. 1) then
         do i = 1, dimen
            do j = 1, dimen
              ss(i,j) = Saux(i,j)
            end do
         end do
c      end if
c
         iImag = (0.d0,1.d0)
c
c
c          if (istep1 .eq. 1) then
           do i = 1, dimen
              do j = 1, dimen
                 cpsi(i,j) = 0.d0
              end do
           end do
c
c
           do i = 1, dimen
```

```
               do j = 1, dimen
                  cpsi(i,j) = (rpsi(i,j) + iImag*ipsi(i,j))
                  cpsio(i,j) = (rpsi(i,j) + iImag*ipsi(i,j))
               end do
            end do
c
c
            do i = 1, dimen
               do j = 1, dimen
                  cpsic(i,j) = cpsi(i,j)
               end do
            end do
c
c
            call sqrtmatrix(ss, dimen, sssqrt)
c
            do i = 1, dimen
               do j = 1, dimen
                 cpsin(i,j) = 0.d0
                 do k = 1, dimen
                    cpsin(i,j) = cpsin(i,j) + sssqrt(i,k)*cpsi(k,j)
                 end do
               end do
            end do
c
c added Nov 21. 2005
c
c          end if

c
          homom5 = (dimen/2)-5
          homom3 = (dimen/2)-3
          homom2 = (dimen/2)-2
          homom1 = (dimen/2)-1
          homo   = (dimen/2)
          lumo   = (dimen/2)+1
          lumop1 = (dimen/2)+2
          lumop2 = (dimen/2)+3
          lumop5 = (dimen/2)+5
c
c ------------------------------------------------------------------------
c
            do i = 1, dimen
               do j = 1, dimen
```

```
                  eye(i,j) = 0.d0
                  HS(i,j) = 0.d0
                  HSL(i,j) = 0.d0
               end do
            end do
c
c ---------------------------------------------------------------------
c
            do i = 1, dimen
               do j = 1, dimen
                  A(i,j)    = 0.d0
                  B(i,j)    = 0.d0
                  D(i,j)    = 0.d0
                  DD(i,j)   = 0.d0
                  newh(i,j) = 0.d0
               end do
            end do
c
c ---------------------------------------------------------------------
            do  i = 1, dimen
                eye(i,i) = (1.d0,0.d0)
            end do
c ---------------------------------------------------------------------
            iImag = (0.d0,1.d0)
c ---------------------------------------------------------------------
c
        call dgetrf(mm, nn, Saux, lda, ipivot,info)
        call dgetri(nn, Saux, lda, ipivot, workd, ldwork,info)
c
         call sqrtmatrix(Saux, dimen, Sauxinvsqr)
c
c   ---------------------------------------------------------------------
c
       do i = 1, dimen
          do j = 1, dimen
             HSL(i,j) = 0.d0
             do k = 1, dimen
                HSL(i,j) = HSL(i,j) + Haux(i,k)*Sauxinvsqr(k,j)
             end do
          end do
       end do
c
c
       do i = 1, dimen
```

```
          do j = 1, dimen
             HS(i,j) = 0.d0
             do k = 1, dimen
                HS(i,j) = HS(i,j) + Sauxinvsqr(i,k)*HSL(k,j)
             end do
          end do
       end do
c
c
       do i = 1, dimen
          do j = 1, dimen
             A(i,j) = eye(i,j) + iImag*0.5d0*(dt/h_bar)*HS(i,j)
             B(i,j) = eye(i,j) - iImag*0.5d0*(dt/h_bar)*HS(i,j)
          end do
       end do
c
        job = invidet
        call zgefa(A,lda,nn,ipivot,info)
        call zgedi(A,lda,nn,ipivot,det,workd,job)
 c
 c
               do i = 1, dimen
                  do j = 1, dimen
                     F(i,j) = (0.d0,0.d0)
                     do k = 1, dimen
                        F(i,j) = F(i,j) + A(i,k)*B(k,j)
                     end do
                  end do
               end do
c
c
               do i = 1, dimen
                  do j = 1, dimen
                     D(i,j) = (0.d0,0.d0)
                     do k = 1, dimen
                        D(i,j) = D(i,j) + Sauxinvsqr(i,k)*F(k,j)
                     end do
                  end do
               end do
c
c ---------------------------------------------------------------------------
               do i = 1, dimen
                  do j = 1, dimen
                     newh(i,j) = (0.d0,0.d0)
```

```
                  do k = 1, dimen
                     newh(i,j) = newh(i,j) + D(i,k)*cpsin(k,j)
                  end do
               end do
            end do
c
cc

c ---------------------------------------------------------------------
10          continue

           nm=nat
           do ii = 1, nm
              do mu = 1, nm
                 qq(mu,ii) = 0.0d0
                 qqp(mu,ii) = 0.0d0
c
                 do nu=1,nm
                   qq(mu,ii) = qq(mu,ii) +
     .                  (cpsi(mu,ii))*ss(mu,nu)*conjg(cpsi(nu,ii))
                 end do
              end do
           end do
C           Compute IPR for all energy points
C           ( Including Si and H atoms)

            if (istep1 .eq. 1) then
               do ii = 1, nm
                  sumipr11n(ii) = 0.0d0
               end do
c
               do ii = 1, natom
                  do jj = 1, nm
                     qsiteav(ii,jj) = 0.0d0
                  end do
               end do
c
            end if
c
            ipp = orbSi * nsiatom
            do ii = 1,nm
c               calculate IPR from Si sites
                sumc=0.0
                do jj = 1, nsiatom
```

```
                  sum=0.0
                  sump=0.0
                  ll = jj*orbSi
                  do kk = (ll-orbSi+1), ll
                     sum = sum + qq(kk,ii)
                  end do
                  qsiteav(jj,ii) = qsiteav(jj,ii) + abs(sum)
                  sumc= sumc+ sum*conjg(sum)
               end do

c
c              Now add IPR from H sites (if there is any)
               if (nhatom .ne. 0) then
                  do jj = 1, nhatom
                     sum=0.0
                     ll = (jj-1)*orbH + 1 + ipp
                     do kk = ll, ll + (orbH-1)
                        sum = sum + qq(kk,ii)
                     end do
                     qsiteav(jj+nSiatom,ii) = qsiteav(jj+nSiatom,ii) +
     .                                        abs(sum)
                     sumc= sumc+ sum*conjg(sum)
                  end do
               end if
c
               sumipr11n(ii) = sumipr11n(ii) + sumc
              if ((ii .ge. homom3).and.(ii .le. lumop2)) then
                 unit = 300 + ii
                 write(unit,*) ii, sumc
              end if
            end do
c
c
            if (istep1 .eq. 1) then
               do j = 1, dimen
                  do i = 1, natom
                     rho_av(i,j) = (qsiteav(i,j)/(1.d0*istep1))*100
                     write(41,*) j, i, rho_av(i,j)
                  end do
               end do
            end if
            if (istep1 .eq. mdsteps) then
               do j = 1, dimen
                  ipr_av(j) = sumipr11n(j)/(1.d0*istep1)
```

```
                  write(42,*) istep1, j, ipr_av(j)
                end do
c
                do j = 1, dimen
                   do i = 1, natom
                      rho_av(i,j) = (qsiteav(i,j)/(1.d0*mdsteps))*100
                      write(43,*) j, i, rho_av(i,j)
                   end do
                end do
              end if

c
               do i = 1, dimen
                  do j = 1, dimen
                     cpsi(i,j) = newh(i,j)
                  end do
               end do
c
                do i = 1, dimen
                  do j = 1, dimen
                     rpsi(i,j) = real(cpsin(i,j))
                     ipsi(i,j) = imag(cpsin(i,j))
                  end do
               end do
c
             return
            end
```

A.1.2 Conductivity: Kubo-Greenwood formula

```
cc
c      Subroutine to calculate the DC conductivity using
c     the Kubo-Greenwood formula in X representation.
c          T. Abtew and D. A. Drabold, Nov. 15 2006
c
          subroutine conductivity(nspin,eo,no,maxo,maxspn,nk,
     .                            Xaux, Yaux, Zaux,
     .                            temp,tempion,ef,rpsi,istep1)
c
c      use precision
c      use sys
c      use parallel
c      use writewave
c#ifdef MPI
```

```
c      use mpi_siesta
c#endif
c
      implicit none
c
c#ifdef MPI
c      integer
c     .  MPIerror
c#endif
c
       integer mbin, Emax, Emin, ii, nn, mm, istep1, maxcond
       integer i, j, dop, homo, lumo, nspin, jj, kk, ll
       integer orbSi, orbH, nsiatom, nhatom, ipp, mu, nu
       integer maxo, maxspn, nk, no
c
       parameter(mbin=501)
c
       double precision
     . kB,temp,tempn,tempion,beta,eV,const,const_delta,dE, sig, pi,
     . EE, cond_E(mbin), diff_EmEn, diff_EnEE, diff_EmEE,
     . delta_EnEE, delta_EmEE, cond_T, diff_EEf, diff_EfEo,
     . fermifun, ef, EEf, EEf_f, EEo, ani_amj, hbar,
     . Xmatrix, Ymatrix, Zmatrix, sum, sum2,
     . Xmatrix_r(no),Ymatrix_r(no),Zmatrix_r(no),
     . Xaux(no,no), Yaux(no,no), Zaux(no,no),ppp,
     . eo(maxo,nspin), rpsi(no,no),xx(no,no),
     . EEf_a, EEf_d, lx, const1, const2,cond_Tfir,cond_Tsec,
     . der_fermi_num, der_fermi_den, der_fermi
       character*12 state
c
         kB    = 8.617339d-5
         hbar = 1.05459d-34
         pi = 3.14159265
         lx = 10.854d-8
c
         beta  = 1.0/(kB*tempion)
         eV    = 13.60580
         sig = 0.05
         ee = 1.6d-19
         const1 = (pi*ee**2)/((lx**3)*(hbar))
c 1Bohr=0.53A --> (1Bohr)**2=2.798d-17
         const2 = (0.53d-8)**2
         const = const1*const2
         const_delta = 1.0/(sig*sqrt(pi))
```

```
c
          Emax  = 10
          Emin  = -10
          dE    = (Emax-Emin)/float(mbin-1)
          diff_EfEo = 0.1
          EEf = ef*eV
c
          do nn = 1, no
              do mm = 1, no
                  xx(nn,mm) = 0.0d0
                  do i = 1,no
                     do j = 1, no
                        xx(nn,mm) = xx(nn,mm) +
     .                              abs(rpsi(nn,i)*Xaux(i,j)*rpsi(mm,j))
                     end do
                  end do
              end do
          end do
c
           do ii = 1, mbin
                EE = Emin + dE*float(ii-1)
                cond_E(ii) = 0.d0
              do nn = 1, no
             diff_EnEE = ( (eo(nn,1)*eV) - EE )**2
                     delta_EnEE = const_delta*exp(-1.0*diff_EnEE/(sig*sig))
                  do mm = 1, no
                      diff_EmEn = ( (eo(mm,1)*eV) - (eo(nn,1)*eV) )**2
                      diff_EmEE = ( (eo(mm,1)*eV) - EE )**2
                      delta_EnEE = const_delta*exp(-1.0*diff_EnEE/(sig*sig))
                      delta_EmEE = const_delta*exp(-1.0*diff_EmEE/(sig*sig))
c
                      cond_E(ii) = cond_E(ii) + (diff_EmEn)*
     .                 (xx(nn,mm)**2)*delta_EnEE*delta_EmEE

                end do
              end do
           end do
c
           EEf_a = EEf
           EEf_d = EEf
           do dop = 1, 30

              if (dop .eq. 1) then
                  state = 'neutral'
```

```
              elseif (dop .le. 16 .and. dop .ne. 1) then
                  state = 'acceptors'
                  EEf_a = (EEf_a - diff_EfEo)
              elseif (dop .gt. 16) then
                  state = 'donors'
                  EEf_d = (EEf_d + diff_EfEo)
              end if

              cond_T = 0.d0
              cond_Tfir = 0.d0
              cond_Tsec = 0.d0
              do ii = 1, mbin
                 EE = Emin + dE*float(ii-1)
c
                 if (dop .eq. 1) then
                    diff_EEf = EE - EEf
                 elseif (dop .le. 16 .and. dop .ne. 1) then
                    diff_EEf = EE - EEf_a
                 elseif (dop .gt. 16) then
                    diff_EEf = EE - EEf_d
                 end if
c
                 der_fermi_num = beta*exp(beta*diff_EEf)
                 der_fermi_den = (1.0 + exp(beta*diff_EEf))**2
                 der_fermi = (der_fermi_num)/(der_fermi_den)
c
               if (ii .eq. 1) then
                   cond_Tfir = 0.5*dE*const*der_fermi*cond_E(1)
               elseif (ii .gt. 1 .or. ii .lt. mbin) then
                   cond_T = cond_T + const*der_fermi*cond_E(ii)*dE
               else
                   cond_Tsec = 0.5*dE*const*der_fermi*cond_E(mbin)
               end if
                  cond_T = cond_Tfir + cond_Tsec + cond_T
                  cond_Tfir = 0.d0
                  cond_Tsec = 0.d0
c
              end do
              if (dop .eq. 1) then
                 write(44,111) istep1, state, EEf, cond_T
              elseif (dop .le. 16 .and. dop .ne. 1) then
                 write(44,111) istep1, state, EEf_a, cond_T
              elseif (dop .gt. 16) then
                 write(44,111) istep1, state, EEf_d, cond_T
```

```
            end if
          end do
c
110       format(2(E16.8E3,2x))
111       format(i8,4x,a12,2x,2(E16.8E3,4x))
c
          end
```